Hybrid quantum information processing with continuous and discrete variables of light fields

Gaia Donati

Linacre College, Oxford

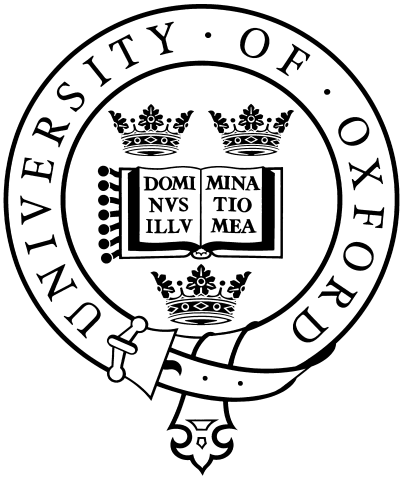

Submitted for the degree of Doctor of Philosophy
Hilary Term 2015

Supervised by
Prof. Ian A. Walmsley

Clarendon Laboratory
University of Oxford
United Kingdom

"Light is the left hand of darkness
and darkness the right hand of light.
Two are one, life and death, lying
together like lovers [...],
like hands joined together,
like the end and the way."

The left hand of darkness, Ursula K. Le Guin

Hybrid quantum information processing with continuous and discrete variables of light fields

Gaia Donati
Linacre College, Oxford

Submitted for the degree of Doctor of Philosophy
Hilary Term 2015

Abstract

Quantum correlations play a fundamental role in quantum information science. The variety of their manifestations has become increasingly apparent following the development of novel light sources, protocols and photodetectors. One broad classification identifies two instances of non-classical correlations: particle and mode entanglement. These categories mirror two coexisting descriptions of quantum systems in terms of discrete and continuous variables of the electromagnetic field. The past decades have generated a number of promising results based on schemes which encompass elements from both frameworks, rather than viewing the two descriptions as mutually exclusive. In this context, it is possible to conceive and realise experiments where either the quantum resource or the detection system is 'hybrid'. Optical weak-field homodyne detectors bring together phase sensitivity and photon counting; as such, they represent a detection scheme which works across continuous and discrete variables of the radiation field.

In this thesis we present a two-mode weak-field homodyne detection layout with added photon-number resolution and apply it to the study of a split single-photon state and a squeezed vacuum state. As a first test of the capabilities of this system, we investigate the reconstruction of relevant features of a given quantum resource – such as its photon statistics – with our detection scheme. Further, we experimentally demonstrate the observation of an instance of non-classical optical coherence which combines the continuous- and discrete-variable descriptions explicitly.

The ability to probe phenomena at the interface of wave and particle regimes opens the way to novel, improved schemes for quantum information processing. From a more fundamental perspective, such hybrid approaches may shed light on the very roots of quantum enhancement.

Publications

- G. Donati, T. J. Bartley, X.-M. Jin, M.-D. Vidrighin, A. Datta, M. Barbieri and I. A. Walmsley. Observing optical coherence across Fock layers with weak-field homodyne detectors. *Nat. Commun.* 5:5584 (2014).
- M. D. Vidrighin, G. Donati, M. G. Genoni, X.-M. Jin, W. S. Kolthammer, M. S. Kim, A. Datta, M. Barbieri and I. A. Walmsley. Joint estimation of phase and phase diffusion for quantum metrology. *Nat. Commun.* 5:3532 (2014).
- T. J. Bartley, G. Donati, X.-M. Jin, A. Datta, M. Barbieri and I. A. Walmsley. Direct observation of sub-binomial light. *Phys. Rev. Lett.* 110:173602 (2013).
- M. Vidrighin, T. J. Bartley, G. Donati, X.-M. Jin, M. Barbieri, W. S. Kolthammer, A. Datta and I. A. Walmsley. Requirements for two-source entanglement concentration. *Quant. Meas. and Quant. Metr.* 1:5 (2013).
- C. M. Natarajan, L. Zhang, H. Coldenstrodt-Ronge, G. Donati, S. N. Dorenbos, V. Zwiller, I. A. Walmsley and R. H. Hadfield. Quantum detector tomography of a time-multiplexed superconducting nanowire single-photon detector at telecom wavelengths. *Opt. Expr.* 21:893 (2013).
- T. J. Bartley, G. Donati, J. B. Spring, X.-M. Jin, M. Barbieri, A. Datta, B. J. Smith and I. A. Walmsley. Multiphoton state engineering by heralded interference between single photons and coherent states. *Phys. Rev. A* 86:043820 (2012).

Contents

List of Figures **ix**

List of Abbreviations **x**

Introduction **xii**

1 Basic quantum optics **1**

1.1 The quantised electromagnetic field 1

1.2 Continuous- and discrete-variable descriptions 12

1.3 Coherence, entanglement and non-locality 20

2 Applied quantum optics **31**

2.1 Beam splitter transformations 31

2.2 Generation of quantum states 37

2.3 Detection of quantum states 46

3 Hybrid schemes in quantum optics **53**

3.1 Weak-field homodyne detection 54

3.2 Phase-dependent detection probabilities 58

3.2.1 Counting and photon statistics 58

3.2.2 Response of a WFH detector to a generic quantum state . . . 65

3.3 Photon statistics and representations in phase space 69

3.3.1 Laying out the theoretical framework 70

3.3.2 Designing an experiment 78

4 Direct observation of non-classical optical coherence 100

4.1 Experimental realisation 101

4.1.1 Rationale for the investigation 101

4.1.2 Layout and test of individual components 104

4.2 Data analysis and modelling 125

4.2.1 Non-classical coherence in a split single-photon state 130

4.2.2 Non-classical coherence in a two-mode squeezed vacuum state 136

4.3 Higher-order Bell tests 142

Conclusions 155

Appendix: Experimental conditional probability matrices 160

Bibliography 180

List of Figures

1.1 Uncertainty relation and quantum states of light 9

1.2 Some classes of quantum states in phase space 11

1.3 Wigner functions of the vacuum, single-photon and squeezed states . 18

1.4 Layout for an experimental Bell test 29

2.1 The beam splitter and the Brown-Twiss interferometer 32

2.2 Parametric downconversion: schematic of the process and phase matching condition 39

2.3 Balanced strong-field homodyne detection 51

3.1 Layout of a single-mode weak-field homodyne detector 56

3.2 Overview of homodyne detection schemes 57

3.3 Schematic of a lossy mode multiplexer 61

3.4 Two-mode weak-field homodyne detection scheme 63

3.5 Simplified experimental layout for the direct probing of a two-mode quantum state 79

3.6 Experimental data and predicted behaviour for the Wigner function of the vacuum state 82

3.7 Experimental data and predicted behaviour for the Wigner function of a thermal state 83

3.8 Dependence of the LO amplitude on the setting of an inactive/active phase rotator 89

3.9 Experimental vs theoretical plots for the Wigner function of a two-mode squeezed vacuum (low pump power) 91

3.10 Experimental vs theoretical plots for the Wigner function of a two-mode squeezed vacuum (high pump power) 92

3.11 Experimental vs theoretical plots for the Wigner function of a two-mode squeezed vacuum with an alternative estimation of the relevant parameters (low pump power) 95

3.12 Experimental vs theoretical plots for the Wigner function of a two-mode squeezed vacuum with an alternative estimation of the relevant parameters (high pump power) 96

4.1 Experimental layout for the observation of non-classical optical coherence across the modes of a split single-photon state 104

4.2 Experimental layout for the observation of non-classical optical coherence across the modes of a squeezed vacuum state 105

4.3 Experimental layout: laser beam preparation 106

4.4 Unfiltered single-photon spectra of downconversion modes 109

4.5 Experimental layout: alignment of PDC source 110

4.6 Filtered spectra of signal and LO in both output channels 114

4.7 Observation of HOMI for a split single photon 115

4.8 Observation of HOMI for the squeezed vacuum 116

4.9 HOMI and compensation of temporal walk-off for the TMSS 118

4.10 Calibration curve for a geometric phase rotator 121

4.11 Phase drifts in the experimental setup: no active phase locking 122

4.12 Phase drifts in the experimental setup: active phase stabilisation . . . 123

4.13 Schematic of an m-stage time-multiplexed detector 125

4.14 Three-fold coincidence counts as a function of LO phase shift: a first signature of non-classicality 127

4.15 Predicted and experimental marginal distributions of counts 129

4.16 Experimental joint counting statistics and theoretical model for the split single photon 133

4.17 Experimental joint counting statistics and revised model (with mixed input state) for the split single photon 135

4.18 Experimental joint counting statistics and theoretical model for the squeezed vacuum 137

4.19 Experimental joint counting statistics and revised model (with thermal noise in the input state) for the squeezed vacuum 139

4.20 Theoretical distribution of counts for the SSPS and the TMSS: role of loss and imperfect state generation 140

4.21 Layout for the theoretical study of generalised Bell inequalities with weak-field homodyne detection 143

4.22 Expectation values of two projectors associated with four-photon events as functions of the LO phase 151

4.23 Violation of generalised Bell inequalities for an increasing number of detected photons 153

List of Abbreviations

APD: avalanche photodiode

BBO: β-barium borate (non-linear crystal)

BS: beam splitter

CGLMP: Collins-Gisin-Massar-Popescu (inequality)

CV: continuous-variable

cw: continuous-wave (laser system)

DFG: difference-frequency generation

DM: dichroic mirror

DV: discrete-variable

EPR: Einstein-Podolsky-Rosen (paper, argument, state)

FPGA: field-programmable gate array

FWHM: full width (at) half maximum

GPR: geometric phase rotator

HeNe: helium-neon (laser)

HOMI: Hong-Ou-Mandel interference

HWP: half-wave plate

IF: interference filter

IR: infrared

JSA: joint spectral amplitude

KDP: potassium dihydrogen phosphate (non-linear crystal)

LO: local oscillator

LVT: local variable theory

PBS: polarising beam splitter

PD: photodiode

PDC: parametric downconversion

PID: proportional-integral-derivative (controller)

PMT: photomultiplier tube

PNRD: photon-number-resolving detector

QIP: quantum information processing

QWP: quarter-wave plate

SFG: sum-frequency generation

SHG: second-harmonic generation

SMF: single-mode fibre

SSPS: split single-photon state

TES: transition-edge sensor

TMD: time-multiplexed detector

TMSS: two-mode squeezed state

UV: ultraviolet

WFH: weak-field homodyne

Introduction

Overview

2015 is the International Year of Light and Light-based Technologies – a recognition of the impact of light science on many present-day technologies[1]. For the occasion, the online journal *Physics* has dedicated a web page to a selection of results (appeared in APS journals) which allowed for a deeper understanding of light-related phenomena while also triggering the fast-paced technological progress that we have witnessed in the past decades[2]. As we browse the list of milestones, we find the works by Townes and collaborators, who first demonstrated microwave amplification by stimulated emission of radiation (MASER) [1]. The maser was the precursor of the laser, which marked the transition from the microwave to the visible part of the electromagnetic spectrum; the first papers reporting on the observation of coherent emission from a semiconductor diode are also included in the APS selection. The maser and the laser started a new era for light-based technological applications. From a purely scientific viewpoint, they greatly facilitated the study of poorly in-

[1]The official website is http://www.light2015.org/Home.html.
[2]See also http://www.physics.aps.org/IYL.

vestigated aspects of quantum mechanics: in the words of Nobel prize recipient R. J. Glauber [2], the quantum theory "has had only a fraction of the influence upon optics that optics has historically had upon quantum theory."

Glauber's seminal paper on the quantum theory of optical coherence[3] features in the selection proposed by *Physics*. Glauber recognised the long-lasting consequences of two technological advances that took place in the decade preceding his first article on quantum optical coherence, published in 1963 [2]. On the one hand, the maser "led to the generation of fields with a range of correlation unprecedented at optical frequencies." On the other hand, the coincident detection of photons showed "the existence of unanticipated correlations in the arrival times of light quanta" such as those observed by Hanbury Brown and Twiss [3]. In Glauber's view, this previously unsuspected behaviour suggested "the growing importance of [...] photon statistics." Such developments were bound to support new approaches to optics; this in turn called for a revised definition of the fundamental concept of coherence.

Glauber showed that it is possible to define optical coherence rigorously if one recasts its description in terms of probabilities of photodetection events. To this end, it is necessary to move away from the purely wave-like definition of this phenomenon, namely "a tendency of two values of the [electromagnetic] field to take on correlated values." Instead, Glauber introduced correlation functions defined as statistical averages of detection observables. Physically, these functions correspond to n-photon delayed coincidence events, so that $G^{(1)}(\mathbf{x}_1, \mathbf{x}_2)$ is associated to count rates, $G^{(2)}(\mathbf{x}_1, \mathbf{x}_2, \mathbf{x}_3, \mathbf{x}_4)$ is related to two-photon coincidence rates and so on[4]. This

[3]The quotes which appear in the following are all taken from this article.

[4]Here $\mathbf{x}_1 = (\mathbf{r}_1, t_1)$ and similarly for the other quantities. All bold letters denote vectors.

theoretical framework leads to the definition of increasing orders of coherence [2]: an nth-order coherent optical field is such that all quantities $G^{(j)}$, for $j \leq n$, can be expressed as a product of first-order correlation functions. In other terms, nth-order coherence means that if we record j-photon coincidence counts, these are not statistically correlated for $j \leq n$. Hence the phenomenon of coherence, once exclusively associated to the wave-like picture of Young's interference fringes, acquires a statistical meaning – it "restrict[s] randomness of the fields" – thanks to a new, general definition which relies on the measurement of discrete photon counts with a detector.

According to Glauber, inventions such as the maser would give access to electromagnetic fields with orders of coherence higher than what had been observed before; the area of non-linear optics was also moving its first steps, considering quantities associated with increasingly high powers in the field strengths. Today, laser systems are an indispensable tool in experimental quantum optics and quantum information science thanks to their coherent light emission and versatility [4, 5]. Non-linear processes have allowed for the production of a variety of quantum states, be it to probe fundamental properties of the quantum theory or to implement quantum information and communication protocols [6–11].

Quantum correlations are at the core of the progress in quantum information science made possible by the generation, manipulation and detection of this growing multitude of experimentally accessible light fields. In fact, the variety of manifestations of such correlations has become ever more apparent as novel light sources, protocols and detectors were investigated. The experiments of Hanbury Brown and

Twiss and the theoretical work of Glauber relied on detection at the single-photon level; the observed quantum correlations belong to a particle-like framework where we consider the specific relation between counting events at different points in space and time. Yet an electromagnetic signal is also a wave: as such, it is characterised by its amplitude and phase (or, equivalently, by suitably defined Cartesian coordinates). If we adopt a wave-like description of light fields, how do we express and observe quantum correlations? An insightful example is given by the class of two-mode squeezed states, which in quantum phase space exhibit correlations between the generalised position and momentum observables, also known as quadratures[5].

In the light of the above discussion, we identify two distinct instances of non-classical correlations or entanglement – particle and mode entanglement [12]. These expressions of quantum correlations mirror two coexisting descriptions of quantum systems which refer to discrete and continuous variables of the electromagnetic field, respectively. The two approaches are often seen as mutually exclusive; the specific experiment determines which description is better suited [13]. Enormous progress has been made in discrete-variable (DV) quantum information processing (QIP), from the implementation of computational operations to that of communication protocols [13]. The continuous-variable (CV) framework, closer to the traditional wave-like approach to optical phenomena, has been the preferred choice for fundamental studies of quantum optics such as the experimental observation of squeezed light or the production of more exotic resources, an example being Schrödinger-cat states [14]. Interestingly, the characterisation of these states was made possible by

[5]This is one part of the story; in the photon-number basis, two-mode squeezed states are characterised by perfect photon-number correlations between the two modes.

a suitably adapted technique taken from classical signal processing – homodyne detection [15].

There exist arguments in favour and against the potential of CV quantum information processing over its DV counterpart. Continuous variables may be advantageous for sensitive tasks such as quantum key distribution and, more generally, for communication protocols [16–19]; other areas, such as continuous-variable quantum computing [20, 21], still lag behind the corresponding discrete-variable implementations significantly [13].

Here we shall deviate from the mutually exclusive viewpoint suggested by the 'CV versus DV debate'. Indeed, the past decades have generated a sparse albeit significant body of work focussed on approaches to quantum optics and QIP which bring together elements from both frameworks. In this view, it is possible to conceive and realise experiments where either the quantum resource or the detection system is 'hybrid'. The latter choice led to a scheme also known as weak-field homodyne (WFH) detection[6]. The WFH technique combines the phase-sensitive layout of optical homodyning with photon counting (with or without photon-number resolution) [22–24]. A number of results have already shown the versatility of this detection system: this ranges from the study of the non-local properties of archetypal non-classical states [22, 25, 26], to the point-by-point reconstruction in quantum phase space of the Wigner quasi-probability distribution for a single-mode state [23, 27, 28]. Examples of what may be called hybrid state engineering make use of photon counting as a heralding operation which prepares the quantum resource in a state later

[6]Although this is a rather natural choice of vocabulary to describe this technique, some of the references cited throughout this thesis do not explicitly refer to it in these terms.

detected with traditional CV techniques such as strong-field homodyning [29, 30]. Continuous-variable states can be used as a starting point for the generation of discrete qubits [31]; interestingly, a CV resource can also exhibit non-classical correlations in the form of entangled qubits [32]. These hybrid approaches to state preparation and characterisation have been considered for applications in quantum computing as well as for communication protocols.

From a conceptual perspective, the role of mode and particle correlations as resources allowing for a quantum outperformance in given scenarios is a subject of debate in itself – one example being the ongoing discussion within the quantum metrology community [12]. In order to fully grasp the potential offered by the quantum theory in light-based research, the capability to investigate phenomena traversing wave-like and particle-like manifestations is likely to lead to new clarifications on the very origin of quantum enhancement.

Thesis outline

Hybrid detection for QIP extended to two-mode quantum states of light constitutes the subject of this thesis. The two-mode layout is a necessary step if we are to apply CV-DV strategies to complex resources with richer structures. Drawing on the expertise built in the Oxford group, photon-number resolution features in our implementation of weak-field homodyning. To test the two-mode WFH layout, we focus on two aspects introduced earlier: firstly, we consider the reconstruction of relevant properties – such as the photon statistics – of a given quantum resource

with our detection system. Further, we show how weak-field homodyne detectors give direct access to an instance of non-classical optical coherence that combines the continuous- and discrete-variable descriptions explicitly.

This thesis is structured as follows: Chapter 1 and 2 contain a selection of topics covering the aspects that are referred to later on. Chapter 3 introduces the technique of weak-field homodyne detection from a historical and technical point of view. We then discuss the first test of our hybrid detection system – accessing relevant information about a two-mode squeezed vacuum state with WFH detectors. In Chapter 4 we report on the main result of this doctoral work. After a detailed description of the experimental layout, we present the experimental observation of non-classical optical coherence across photon-number states for two classes of two-mode quantum states. We conclude with a summary of our investigations and an outlook on hybrid approaches to quantum information processing.

Chapter 1

Basic quantum optics

1.1 The quantised electromagnetic field

At the core of the quantum theory of radiation lies the association of a quantum harmonic oscillator with a mode of the electromagnetic field [33, 34]. A wave vector $\mathbf{k}$ and a polarisation (which identifies the direction of the electric field in space) define a *spatial mode* of the radiation field. This mode can be excited by the electromagnetic field; most often, a field excitation will be expressed as a linear combination of spatial-temporal modes.

In a classical picture where we consider an electromagnetic radiation confined in a cavity and expand electric and magnetic fields in normal modes, the Hamiltonian for the system reads

$$H = \frac{1}{2} \sum_{\mathbf{k},\ell} \left(m_k \omega_k^2 X_{\mathbf{k},\ell}^2 + \frac{P_{\mathbf{k},\ell}^2}{m_k} \right). \tag{1.1}$$

We recognise each term in the above sum as the energy of a harmonic oscillator: this 'mechanical equivalent' of a field mode is characterised by its mass m_k, frequency of oscillation $\omega_k = k\,c$ (with $k \equiv |\mathbf{k}|$), position $X_{\mathbf{k},\ell}$ and canonical momentum $P_{\mathbf{k},\ell} = m_k \dot{X}_{\mathbf{k},\ell}$. The index ℓ labels the two available choices of polarisation for every wave vector $\mathbf{k}$ (as the polarisation state of the radiation field belongs to a two-dimensional space).

From Eq.(1.1) we see that each mode of the radiation field is dynamically equivalent to a mechanical harmonic oscillator [34]. We quantise the electromagnetic field by identifying the conjugate coordinates $X_{\mathbf{k},\ell}$ and $P_{\mathbf{k},\ell}$ with two non-commuting operators such that

$$[\hat{X}_{\mathbf{k},\ell}, \hat{P}_{\mathbf{k}',\ell'}] = \imath\hbar\,\delta(\mathbf{k}-\mathbf{k}')\delta_{\ell\ell'}\,, \quad \text{and} \quad [\hat{X}_{\mathbf{k},\ell}, \hat{X}_{\mathbf{k}',\ell'}] = [\hat{P}_{\mathbf{k},\ell}, \hat{P}_{\mathbf{k}',\ell'}] = 0\,. \tag{1.2}$$

We further introduce the dimensionless operators $\hat{a}_{\mathbf{k},\ell}$ and $\hat{a}^\dagger_{\mathbf{k},\ell}$:

$$\begin{aligned} \hat{a}_{\mathbf{k},\ell} &= \sqrt{\frac{1}{2m_k\hbar\omega_k}}(m_k\omega_k\hat{X}_{\mathbf{k},\ell} + \imath\hat{P}_{\mathbf{k},\ell})\,, \\ \hat{a}^\dagger_{\mathbf{k},\ell} &= \sqrt{\frac{1}{2m_k\hbar\omega_k}}(m_k\omega_k\hat{X}_{\mathbf{k},\ell} - \imath\hat{P}_{\mathbf{k},\ell})\,. \end{aligned} \tag{1.3}$$

The commutation relations for $\hat{a}_{\mathbf{k},\ell}$ and $\hat{a}^\dagger_{\mathbf{k},\ell}$ follow from Eq.(1.2).

In terms of these new operators the quantised Hamiltonian of the radiation field becomes [33]

$$\hat{H} = \sum_{\mathbf{k},\ell} \hbar\omega_{\mathbf{k},\ell}\left(\hat{a}^\dagger_{\mathbf{k},\ell}\hat{a}_{\mathbf{k},\ell} + \frac{1}{2}\hat{I}\right). \tag{1.4}$$

The electric field operator reads

$$\hat{\mathbf{E}}(\mathbf{r},t) = \sum_{\mathbf{k},\ell} \mathbf{e}_{\mathbf{k},\ell}\, \imath\, \mathcal{E}_k \left(\hat{a}_{\mathbf{k},\ell}\, e^{-\imath(\omega_k t - \mathbf{k}\cdot\mathbf{r})} + \hat{a}^\dagger_{\mathbf{k},\ell}\, e^{\imath(\omega_k t - \mathbf{k}\cdot\mathbf{r})} \right) = \hat{\mathbf{E}}^{(+)}(\mathbf{r},t) + \hat{\mathbf{E}}^{(-)}(\mathbf{r},t)\,, \tag{1.5}$$

where $\mathbf{e}_{\mathbf{k},\ell}$ is a unit vector and $\mathcal{E}_k$ has the dimensions of an electric field. An analogous expression holds for the magnetic field operator.

Let us consider a single mode of the electromagnetic field in order to introduce the quantum states of light that we shall refer to throughout this thesis; while this choice simplifies the mathematical formulae, it doesn't compromise the validity of the obtained results.

In the single-mode case, Eq.(1.4) becomes

$$\hat{H} = \hbar\omega \left(\hat{a}^\dagger \hat{a} + \frac{1}{2}\hat{I} \right). \tag{1.6}$$

We define the photon-number operator as $\hat{n} := \hat{a}^\dagger \hat{a}$. Its eigenvalues correspond to the number n of light quanta, or photons, that are excited in the considered electromagnetic mode [33]. The eigenvectors of $\hat{n}$ are known as *Fock states* $\{|n\rangle\}$:

$$\hat{n}|n\rangle = n|n\rangle\,. \tag{1.7}$$

Interestingly, it is possible to show that $\hat{a}|n\rangle$ and $\hat{a}^\dagger|n\rangle$ are also eigenstates of the number operator; from this result it follows that

$$\hat{a}|n\rangle = \sqrt{n}|n-1\rangle \quad \text{and} \quad \hat{a}^\dagger|n\rangle = \sqrt{n+1}|n+1\rangle\,. \tag{1.8}$$

These formulae justify why $\hat{a}$ and $\hat{a}^\dagger$ are known as the annihilation and creation operators of the radiation field: when the electromagnetic energy in a mode decreases (increases), we refer to a photon being destroyed (created) through the application of $\hat{a}$ ($\hat{a}^\dagger$). With reference to Eq.(1.5), we notice that the positive frequency part of $\hat{\mathbf{E}}(\mathbf{r},t)$ contains annihilation operators only, whereas $\hat{\mathbf{E}}^{(-)}(\mathbf{r},t)$ is a function of creation operators.

The quantity n takes on integer, non-negative values – 'fractional photons' do not exist [35]. Further, a peculiarity of the quantum theory of light is that it assigns a meaning to the state devoid of photons – the vacuum state $|0\rangle$. As an energy eigenvector, $|0\rangle$ is such that $\hat{H}|0\rangle = (\hbar\omega/2)\,|0\rangle$; $E_0 := \hbar\omega/2$ is the ground state energy of the quantum harmonic oscillator. Because no energy eigenvalue lower than E_0 can exist[1], it follows that $\hat{a}|0\rangle = 0$ [34].

Repeated application of the creation operator to the vacuum state allows us to express Fock state $|n\rangle$ as

$$|n\rangle = \frac{(\hat{a}^\dagger)^n}{\sqrt{n!}}\,|0\rangle\,. \tag{1.9}$$

We see that all photon-number states arise as excitations of the vacuum. Fock states are orthonormal and form a complete set of quantum states (also called the Fock basis), i.e. they span the entire Hilbert space of the electromagnetic oscillator. Mathematically, these statements translate into

$$\sum_{n=0}^{+\infty} |n\rangle\langle n| = 1 \quad \text{and} \quad \langle n|n'\rangle = \delta_{nn'}\ \forall\ n,n' \in \mathbb{N}. \tag{1.10}$$

[1] A proof of this statement can be given in terms of regular and irregular wave functions [35].

An eigenstate of the annihilation operator $\hat{a}$ is known as a *coherent state* $|\alpha\rangle$ of the radiation field[2]:

$$\hat{a}|\alpha\rangle = \alpha|\alpha\rangle\,. \tag{1.11}$$

The eigenvalue α is a complex number as $\hat{a}$ is not Hermitian. Consequently, coherent states are characterised by their amplitude $|\alpha|$ and phase ϕ such that $\alpha = |\alpha|e^{i\phi}$. Let us now draw the connection between coherent fields and the quantum harmonic oscillator ground state. To this end, we introduce the displacement operator $\hat{D}(\alpha)$:

$$\hat{D}(\alpha) := e^{\alpha\hat{a}^\dagger - \alpha^*\hat{a}} = e^{-|\alpha|^2/2}e^{\alpha\hat{a}^\dagger}e^{-\alpha^*\hat{a}}\,, \tag{1.12}$$

where we used the Baker-Hausdorff formula [36] to obtain the second expression. The displacement operator is unitary; it owes its name to the way it acts on the annihilation and creation operators. Indeed, we have that

$$\hat{D}^\dagger(\alpha)\,\hat{a}\,\hat{D}(\alpha) = \hat{a} + \alpha\hat{I} \tag{1.13}$$

and an analogous result holds for $\hat{a}^\dagger$. We then consider the following calculation [35]:

$$\hat{a}\hat{D}(-\alpha)|\alpha\rangle = \hat{D}(-\alpha)\hat{D}^\dagger(-\alpha)\,\hat{a}\,\hat{D}(-\alpha)|\alpha\rangle = \hat{D}(-\alpha)(\hat{a} - \alpha\hat{I})|\alpha\rangle\,. \tag{1.14}$$

Yet $(\hat{a} - \alpha\hat{I})|\alpha\rangle = 0$ from Eq.(1.11), hence

$$\hat{D}(-\alpha)|\alpha\rangle \equiv |0\rangle \quad \Rightarrow \quad |\alpha\rangle = \hat{D}(\alpha)|0\rangle. \tag{1.15}$$

[2]Equivalently, $|\alpha\rangle$ is an eigenstate of $\hat{\mathbf{E}}^{(-)}(\mathbf{r}, t)$ (see Eq.(1.5)).

A coherent state is thus a 'displaced' vacuum state. The complex quantity α sets the strength and direction of the displacement; this operation is best visualised in quantum phase space, as we shall see in the next section.

Eqn.(1.12) and (1.15) allow us to express a coherent state $|\alpha\rangle$ in the Fock basis:

$$|\alpha\rangle = e^{-|\alpha|^2/2} \sum_{n=0}^{+\infty} \frac{\alpha^n}{\sqrt{n!}} |n\rangle \,. \tag{1.16}$$

From this result, it follows that the mean number of photons in $|\alpha\rangle$ is $\langle\alpha|\hat{n}|\alpha\rangle = |\alpha|^2$. Further, it is possible to show that the probability $|\langle n|\alpha\rangle|^2$ is described by Poisson distribution. This is a distinctive feature of coherent states: while Fock states are characterised by a definite number of photons, we do not know with certainty how many light quanta populate a coherent state of the radiation field.

Let us refer back to the observables $\hat{X}$ and $\hat{P}$ associated with our quantised harmonic oscillator. We are interested in computing the variances of these operators when the field is in a coherent state $|\alpha\rangle$. Heisenberg's uncertainty principle states that, given two non-commuting observables, their expectation values cannot be simultaneously determined with arbitrary precision. Therefore, the uncertainties[3] ΔX and ΔP must satisfy the inequality

$$\Delta X \, \Delta P \geq \frac{\hbar}{2} \,. \tag{1.17}$$

For a coherent state $|\alpha\rangle$ we find that $(\Delta X)_\alpha = \sqrt{\frac{\hbar}{2\omega}}$ and $(\Delta P)_\alpha = \sqrt{\frac{\hbar\omega}{2}}$, where

[3]In this thesis, standard deviations such as ΔX and ΔP are also called uncertainties, while $(\Delta X)^2$ and $(\Delta P)^2$ are the corresponding variances.

$(\Delta X)_\alpha = \sqrt{\langle\alpha|\hat{X}^2|\alpha\rangle - (\langle\alpha|\hat{X}|\alpha\rangle)^2}$ and a similar expression holds for $(\Delta P)_\alpha$. It thus follows that $(\Delta X)_\alpha(\Delta P)_\alpha = \hbar/2$, which corresponds to the lower bound set by Heisenberg's relation. Coherent states belong to the class of minimum-uncertainty states: the variances of the generalised position and momentum variables are as small as Heisenberg's principle allows for. This feature of coherent states clarifies why they are sometimes treated as classical states: the position and momentum of a classical wave can be measured simultaneously with unbounded precision, hence to satisfy the lower bound in Eq.(1.17) is to be as close as possible to the classical world. Moreover, the well-defined amplitude and phase of a coherent state identify it naturally as a wave-like resource (see Eq.(1.11)).

Scully and Zubairy provide an insightful argument to illustrate the origin of the expression 'coherent state of radiation' [34]. They set out to find a state which displays a constant value for ΔX in the presence of a harmonic potential – this quantum wave packet $\psi(X,t)$ shall be the closest to a classical field. This state turns out to be precisely a coherent field: in the coordinate representation, its wave function describes a wave packet which does not vary in shape as a function of time, i.e. the wave packet *coheres*. The emission from high-quality laser systems approaches coherent states of the electromagnetic field.

As a conclusive remark before introducing the last class of quantum states which is of interest to us, we note that $(\Delta X)_n(\Delta P)_n = \hbar\left(n+\frac{1}{2}\right)$ for number states. It follows that, for $n = 0$, $(\Delta X)_n(\Delta P)_n \equiv (\Delta X)_\alpha(\Delta P)_\alpha$. Hence not only is the vacuum state a minimum-uncertainty state; its definition does not depend on the representation adopted to describe it.

We now introduce dimensionless versions of the generalised position and momentum observables $\hat{X}$ and $\hat{P}$:

$$\begin{aligned} \hat{x} &= \sqrt{\frac{m\omega}{\hbar}}\,\hat{X} = \frac{\hat{a}^\dagger + \hat{a}}{\sqrt{2}}\,, \\ \hat{p} &= \sqrt{\frac{1}{m\omega\hbar}}\,\hat{P} = \frac{\imath(\hat{a}^\dagger - \hat{a})}{\sqrt{2}} \end{aligned} \tag{1.18}$$

and $[\hat{x}, \hat{p}] = \imath$. Conversely,

$$\hat{a} = \frac{\hat{x} + \imath\hat{p}}{\sqrt{2}} \quad \text{and} \quad \hat{a}^\dagger = \frac{\hat{x} - \imath\hat{p}}{\sqrt{2}}\,. \tag{1.19}$$

$\hat{x}$ and $\hat{p}$ are also observables of the electromagnetic oscillator; Eq.(1.17) becomes

$$\Delta x \Delta p \geq 1/2\,. \tag{1.20}$$

What is the interest of these Hermitian operators? If we consider a single-mode electric field at a fixed point in space, $\hat{\mathbf{E}}(t) = \mathbf{e}\,\imath\,\mathcal{E}(\hat{a}e^{-i\omega t} + \hat{a}^\dagger e^{i\omega t})$, we can express it in terms of $\hat{x}$ and $\hat{p}$ as

$$\hat{\mathbf{E}}(t) = \mathbf{e}\,\imath\sqrt{2}\,\mathcal{E}\,(\hat{x}\cos\omega t + \hat{p}\sin\omega t)\,. \tag{1.21}$$

We see that $\hat{x}$ and $\hat{p}$ represent the amplitudes – dephased by $\pi/2$ with respect to each other – of the electric field $\hat{\mathbf{E}}(t)$; we refer to these operators as the *quadratures* of the radiation field. As we shall see shortly, they allow us to introduce a useful representation for quantum states in the so-called quadrature (quantum) phase

space. $\hat{x}$ and $\hat{p}$ are also observables quantities which, as explained in the following, are easier to measure than amplitude and phase.

As illustrated in Fig. 1.1, Eq.(1.20) identifies a hyperbola in the two-dimensional space $(\Delta x, \Delta p)$. The point on the hyperbola for which $\Delta x = \Delta p$ corresponds to

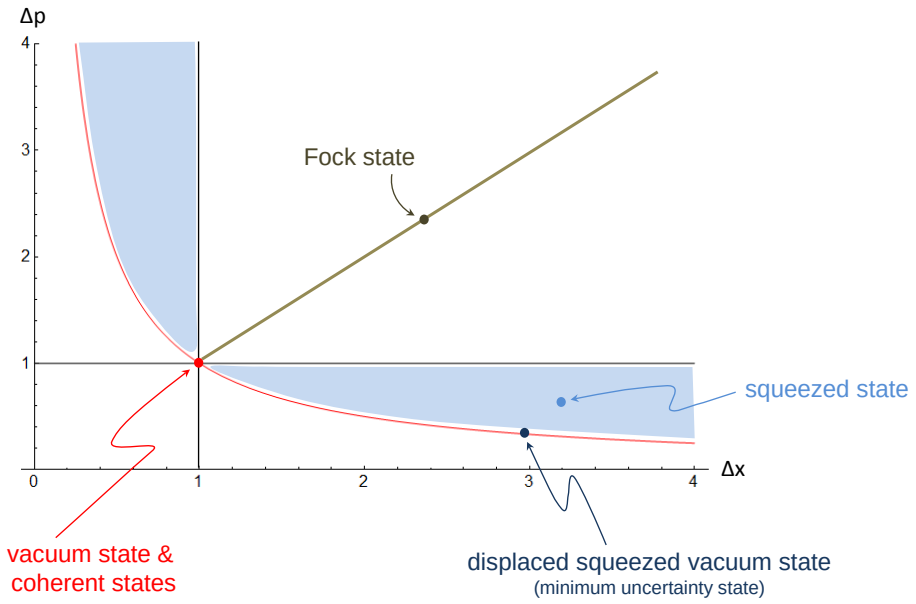

Figure 1.1 Heisenberg's principle allows us to graphically summarise some characteristic properties of the classes of quantum states considered in this chapter. Minimum-uncertainty states lie on the hyperbola (solid red curve – we note that we plotted $1/\Delta x$ instead of $1/(2\Delta x)$). Physical states, such as Fock states and squeezed light, are found in the region above this curve.

coherent states (and the vacuum). Photon-number states reside in the region where the uncertainties in the quadratures are equal and are both greater than $1/\sqrt{2}$. What about the light blue regions and the points on the hyperbola which do not describe coherent fields? These states have a special feature: one of their variances is *smaller* than $1/2$ – we could say that this uncertainty is *squeezed*. Unsurprisingly, the reduction of one variance comes at the expense of the second, which takes on a value greater than that of the vacuum in accordance with Heisenberg's principle.

Squeezed states of the radiation field populate the light blue regions in Fig. 1.1. The hyperbola $1/(2\Delta x)$, which partly bounds such regions, identifies all minimum-uncertainty states. The latter correspond to displaced squeezed vacuum states [35]:

$$|\psi\rangle = \hat{D}(\alpha)\hat{S}(\zeta)|0\rangle\,, \tag{1.22}$$

where $\hat{S}(\zeta)$ is known as the squeezing operator. We define it as

$$\hat{S}(\zeta) := e^{\frac{1}{2}\left(\zeta^*\hat{a}^2 - \zeta(\hat{a}^\dagger)^2\right)} \tag{1.23}$$

and $\zeta = \mathsf{r}e^{\imath\theta}$. We note that the unitary operator $\hat{S}(\zeta)$ is quadratic in $\hat{a}$ and $\hat{a}^\dagger$: we will present an alternative way of obtaining the squeezing operator in Chapter 2.
It is useful to mention a few additional results before we highlight the physical meaning of the class of quantum states that we have just introduced. Application of $\hat{S}(\zeta)$ to the annihilation and creation operators yields

$$\begin{aligned}
\hat{S}^\dagger(\zeta)\hat{a}\hat{S}(\zeta) &= \hat{a}\cosh\mathsf{r} - \hat{a}^\dagger e^{\imath\theta}\sinh\mathsf{r}\,,\\
\hat{S}^\dagger(\zeta)\hat{a}^\dagger\hat{S}(\zeta) &= \hat{a}^\dagger\cosh\mathsf{r} - \hat{a}e^{-\imath\theta}\sinh\mathsf{r}\,.
\end{aligned} \tag{1.24}$$

Given the phase-shifting operator $\hat{U}(\theta) := e^{-\imath\theta\hat{n}}$, we introduce the rotated quadratures $\hat{x}_\theta$ and $\hat{p}_\theta$ as [35]

$$\begin{aligned}
\hat{x}_\theta &:= \hat{U}^\dagger(\theta)\,\hat{x}\,\hat{U}(\theta) = \hat{x}\cos\theta + \hat{p}\sin\theta\,,\\
\hat{p}_\theta &:= \hat{U}^\dagger(\theta)\,\hat{p}\,\hat{U}(\theta) = -\hat{p}\sin\theta + \hat{p}\cos\theta\,.
\end{aligned} \tag{1.25}$$

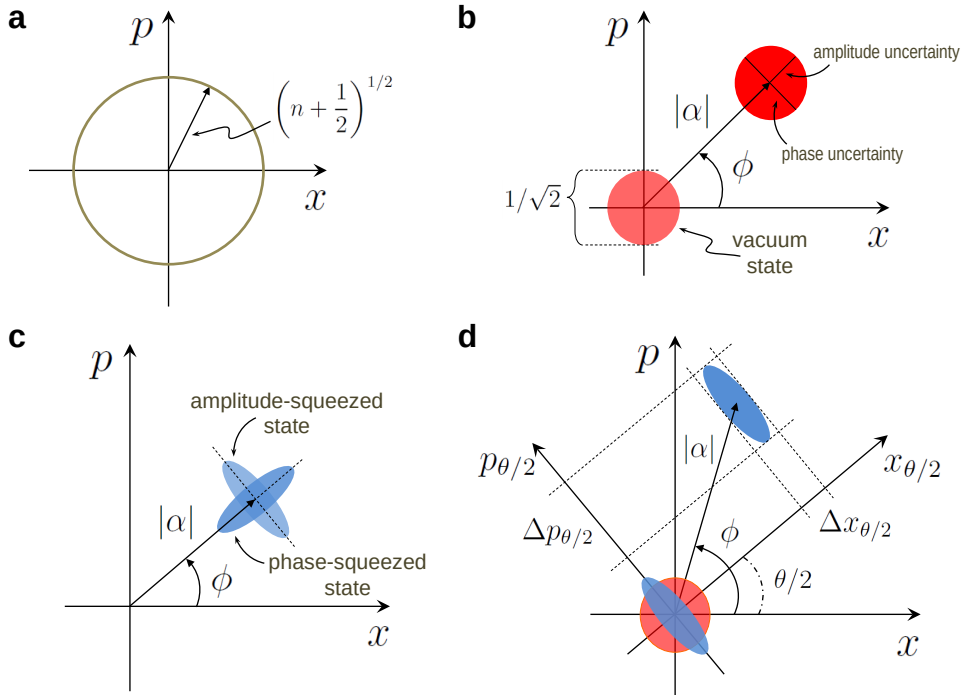

Figure 1.2 **(a)** In a phase-independent Fock state, the uncertainty associated with x and p depends on the number n of photons present in the state (which is a well-defined quantity). **(b)** Coherent states are displaced vacuum states, identified in quantum phase space by their amplitude $|\alpha|$ and phase ϕ characterised by the same uncertainty. **(c)** With reference to the coherent state in **(b)**, we note the distinction between amplitude and phase squeezing. **(d)** A squeezed vacuum state is obtained by squeezing and displacing the coherent vacuum. In the coordinate frame rotated by $\theta/2$, we see that the uncertainty in one variable is reduced below the vacuum level (here $\Delta x_{\theta/2}$) at the expense of its conjugate coordinate.

Similarly, we define a rotated complex amplitude

$$\hat{a}_{\theta/2} := (\hat{x} + \imath\hat{p})e^{-\imath\theta/2} = \hat{x}_{\theta/2} + \imath\,\hat{p}_{\theta/2}\,. \tag{1.26}$$

From Eqn.(1.24) and (1.26) we can then compute

$$\hat{S}^{\dagger}(\zeta)\,\hat{a}_{\theta/2}\,\hat{S}(\zeta) = \hat{x}_{\theta/2}\,e^{-\mathsf{r}} + \imath\,\hat{p}_{\theta/2}\,e^{\mathsf{r}}\,. \tag{1.27}$$

For the uncertainties in the observables $\hat{x}_{\theta/2}$ and $\hat{p}_{\theta/2}$ we find

$$\Delta x_{\theta/2} = \frac{1}{\sqrt{2}} e^{-\mathsf{r}}\,, \quad \Delta p_{\theta/2} = \frac{1}{\sqrt{2}} e^{\mathsf{r}} \quad \Rightarrow \quad \Delta x_{\theta/2}\, \Delta p_{\theta/2} = \frac{1}{2}\,. \tag{1.28}$$

The seemingly arbitrary introduction of the rotated quadratures sheds light on the physical effect of squeezing: the uncertainty in one quadrature, here $\hat{x}_{\theta/2}$, is reduced (or squeezed) by a factor $e^{-\mathsf{r}}$ below the vacuum level, whereas the uncertainty in $\hat{p}_{\theta/2}$ is amplified by the same factor. Therefore, squeezed states allow us to measure one variable with enhanced precision while accepting a greater ignorance about its conjugate. In Fig. 1.2 we provide a graphical interpretation of the results discussed in this section.

1.2 Continuous- and discrete-variable descriptions

In the introduction we mentioned the two conventional descriptions based on discrete and continuous variables of the electromagnetic field. Indeed, most quantum systems possess both types of degrees of freedom: for an optical field, examples of the former class would be its polarisation and photon number, while wavelength and wave vector are instances of continuous variables. We have already noted that hybrid QIP goes beyond the view according to which DV and CV approaches are mutually exclusive. We must stress that discrete and continuous variables do not correspond to either few or many photons [13]; nonetheless, the current technology effectively prevents the description of a very intense light field in terms of discrete variables. In this

sense, the choice of one representation over the other depends on the experimental setup and, particularly, on the detection system. In the introduction we highlighted the success of discrete-variable schemes for QIP; on the other hand, we observed that continuous variables are naturally reminiscent of the traditional wave-like picture of optics. As an additional feature of CV strategies, it may be argued that they can give access to larger state spaces[4], thus broadening the range of accessible resources.

In the previous section we introduced the quantum states which will appear throughout this thesis – coherent fields, Fock states and squeezed light. Although we did not state this choice explicitly, we made use of Dirac's notation for the quantised radiation field in terms of kets and bras. We now discuss an alternative representation which suits particularly well the continuous-variable description of quantum states.

Classically, a particle is identified by one point $(x_{\mathrm{cl.}}, p_{\mathrm{cl.}})$ in phase space (where $x_{\mathrm{cl.}}$ is its position and $p_{\mathrm{cl.}}$ its momentum). For an ensemble of particles, we refer to a statistical mechanics framework where the probability associated to each point in phase space is governed by a probability density function. The latter approach can be transferred to the quantum domain. In quantum phase space we introduce a *quasi*-probability distribution $W(x,p)$ known as the Wigner function. If $W(x,p)$ is a valid probability density for a quantum state, we expect the marginal distributions given by $\int_{-\infty}^{+\infty} W(x,p)dp$ and $\int_{-\infty}^{+\infty} W(x,p)dx$ to yield classical probability densities associated with x and p, respectively. Moreover, if we consider a phase-shifting operation $\hat{U}(\theta)$ we expect the quadratures to transform into rotated variables x_θ

[4]We remark that there are examples in the literature where the comparison between CVs and DVs corresponds to the distinction between infinite- and finite-dimensional spaces.

and p_θ, and $W(x,p)$ to change accordingly. The two aspects that we have just mentioned – marginal distributions and rotations in quantum phase space – lead to the definition of the Wigner function as we postulate that

$$p(x,\theta) = \langle x|\hat{U}(\theta)\hat{\rho}\,\hat{U}^\dagger(\theta)|x\rangle = \int_{-\infty}^{+\infty} W(x\cos\theta - p\sin\theta, x\sin\theta + p\cos\theta)\,dp\,, \quad (1.29)$$

where $p(x,\theta)$ is the probability distribution for x following a phase shift (applied to the density operator $\hat{\rho}$ which describes the state of the considered system).

Remarkably, this postulate is all we need to introduce the quasi-probability function $W(x,p)$ in quantum phase space [35]. Indeed, for $\theta = 0$ and $\theta = \pi/2$, we find

$$\begin{aligned} p(x,0) &= \langle x|\hat{\rho}|x\rangle = \int_{-\infty}^{+\infty} W(x,p)dp \quad \text{and} \\ p\left(x,\frac{\pi}{2}\right) &= \langle p|\hat{\rho}|p\rangle = \int_{-\infty}^{+\infty} W(-p,x)\,dx = \int_{-\infty}^{+\infty} W(x,p)\,dx\,, \end{aligned} \quad (1.30)$$

respectively[5].

The explicit formula for $W(x,p)$ quoted in most quantum optics textbooks highlights the close connection between $W(x,p)$ and the density operator $\hat{\rho}$. We express the Wigner distribution for a single-mode state as [35]

$$W(x,p) = \frac{1}{2\pi}\int_{-\infty}^{+\infty} e^{\imath p\nu}\langle x-\nu/2|\hat{\rho}|x+\nu/2\rangle\,d\nu\,. \quad (1.31)$$

The Wigner function is normalised, and $W^*(x,p) = W(x,p)$.

In the light of its definition and properties, it is not yet clear why we termed the

[5]To compute $p(x,\pi/2)$ we used the expressions for the rotated quadratures (see Eq.(1.25)).

Wigner function a *quasi*-probability distribution. To illustrate this key feature, let us consider a remarkable expression – the overlap formula:

$$\mathrm{Tr}[\hat{B}_1\hat{B}_2] = 2\pi \int_{-\infty}^{+\infty}\int_{-\infty}^{+\infty} W_1(x,p)W_2(x,p)\,dxdp\,, \tag{1.32}$$

where $W_1(x,p)$ and $W_2(x,p)$ are the Wigner functions associated with two arbitrary operators $\hat{B}_1$ and $\hat{B}_2$. This result allows us to calculate the expectation value of $\hat{B}_2$, for instance, on a state described by $\hat{\rho}$ as

$$\langle\hat{B}_2\rangle = \mathrm{Tr}[\hat{\rho}\hat{B}_2] = 2\pi \int_{-\infty}^{+\infty}\int_{-\infty}^{+\infty} W(x,p)W_2(x,p)\,dxdp\,. \tag{1.33}$$

Interestingly, we would write a similar expression in classical statistical mechanics. From a quantum-mechanical perspective, we see from Eq.(1.33) that we only have access to 'filtered projections' of the Wigner function associated with the observed system (interpreting $W_2(x,p)$ as a 'filter function', in this example) [35].

The overlap formula has another immediate consequence given by the expression

$$|\langle\psi_1|\psi_2\rangle|^2 = 2\pi \int_{-\infty}^{+\infty}\int_{-\infty}^{+\infty} W_1(x,p)W_2(x,p)\,dxdp\,. \tag{1.34}$$

$|\langle\psi_1|\psi_2\rangle|^2$ expresses the overlap between $|\psi_1\rangle$ and $|\psi_2\rangle$: it yields 0 if the two states are orthogonal. This seemingly unassuming formula highlights the fundamental difference between classical phase-space densities and the Wigner function. If $W_1(x,p)$ and $W_2(x,p)$ were two positive functions it would not be possible for $|\langle\psi_1|\psi_2\rangle|^2$ to vanish for some states. Therefore, we must conclude that the Wigner function can

take on negative values – a rather odd feature for a classical probability density. Consequently, $W(x,p)$ can only be interpreted as a *quasi*-probability distribution; regions where the Wigner function is negative indicate the non-classical nature of the considered quantum state.

Finally, we mention a result that we will extend to two-mode states in Chapter 3. Thanks to the overlap formula, it is possible to retrieve the elements of the density matrix ρ for a given state from its Wigner function:

$$\langle m|\hat{\rho}|n\rangle = \mathrm{Tr}\big[\hat{\rho}|n\rangle\langle m|\big] = 2\pi \int_{-\infty}^{+\infty}\int_{-\infty}^{+\infty} W(x,p)W_{n,m}(x,p)\,dxdp\,. \tag{1.35}$$

Here we chose the photon-number basis to compute the elements of ρ, but any complete set of states leads to the same conclusion. Interestingly, this expression provides a criterion to identify if a function $W(x,p)$ is a Wigner distribution: all diagonal elements calculated from the above formula must be non-negative [35].

Once again, it is useful to visualise the Wigner functions associated with the quantum states introduced earlier on. Fig. 1.3 illustrates the quasi-probability distributions for the coherent vacuum $|0\rangle$, the single-photon state $|1\rangle$ and a squeezed vacuum state. For pure states, explicit expressions for $W(x,p)$ can be computed directly from Eq.(1.31). For example, for the vacuum state we find

$$W_{\mathrm{vacuum}}(x,p) = \frac{1}{2\pi}\int_{-\infty}^{+\infty} e^{\imath p\nu}\langle x-\nu/2|0\rangle\langle 0|x+\nu/2\rangle\,d\nu = \frac{1}{\pi}\,e^{-(x^2+p^2)}\,. \tag{1.36}$$

To justify the second passage in Eq.(1.36) we must define the quadrature wave

functions $\Psi(x) = \langle x|\Psi\rangle$ and $\Psi(p) = \langle p|\Psi\rangle$. For the vacuum state we have that $\langle x|0\rangle = (1/\pi^{1/4})\, e^{-x^2/2}$, from which the above result for $W_{\text{vacuum}}(x,p)$ follows [35]. Similarly, it is possible to show that

$$W_{\text{squeezed}}(x,p) = \frac{1}{\pi}\, e^{-\left(e^{2\zeta}x^2 + e^{-2\zeta}p^2\right)} = \frac{1}{\pi}\, e^{-\left(\frac{x^2}{2\sigma^2} + \frac{p^2}{2\tau^2}\right)}\,, \tag{1.37}$$

where we recall that $\zeta = \mathsf{r}e^{\imath\theta}$ and we defined the uncertainties $\sigma := e^{-\zeta}/\sqrt{2}$ and $\tau := e^{\zeta}/\sqrt{2}$. We further note that $W_{\text{squeezed}}(x,p) \equiv W_{\text{vacuum}}(e^{\zeta}x, e^{-\zeta}p)$.

As expected, the effect of squeezing is visible in the variances associated with the quadratures, respectively squeezed and stretched by a factor $e^{2\zeta}$. More general expressions for $W_{\text{squeezed}}(x,p)$ can be obtained, for example, by applying a non-zero displacement $\hat{D}(\alpha)$ to the initial state.

With reference to Fig. 1.3, we observe the Gaussian character of $W_{\text{vacuum}}(x,p)$ and $W_{\text{squeezed}}(x,p)$. Coherent states are also described by Gaussian functions, although these are displaced away from the origin of quantum phase space according to the amplitude and phase of the complex parameter α in $\hat{D}(\alpha)$. For $\alpha = x_0 + \imath p_0$ we find

$$W_{\text{coherent}}(x,p) = \frac{1}{\pi}\, e^{-\left[(x-x_0)^2 + (p-p_0)^2\right]}\,. \tag{1.38}$$

By contrast, the Wigner function of the single-photon state displays negative values (see Fig. 1.3) – a feature which we predicted as a consequence of the overlap formula, and a signature of non-classicality. The expression of the Wigner function for Fock states requires the introduction of a quasi-probability distribution known as the Q

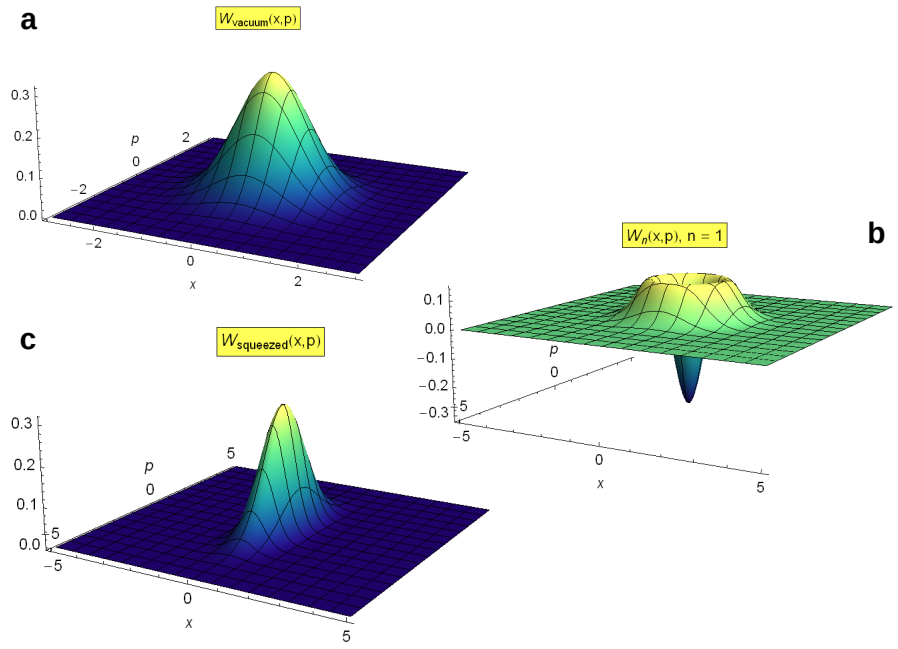

Figure 1.3 These are the representations in quantum phase space of three quantum states discussed in the present chapter. The Wigner distribution of the coherent vacuum is a Gaussian function which recalls a classical probability density. By contrast, the Wigner function of the one-photon state drops below zero at the origin of phase space. The effect of the squeezing operation (here without displacement) is clearly seen in the quasi-probability distribution for a squeezed vacuum state with $\zeta \in \mathbb{R}$ and $\mathsf{r} = 0.5$.

function; it is then possible to show that

$$W_n(x,p) = \frac{(-1)^n}{\pi}\, e^{-(x^2+p^2)}\, \mathcal{L}_n(2x^2+2p^2) \tag{1.39}$$

for a state with n photons [35]. $\mathcal{L}_n(2x^2+2p^2)$ denotes the Laguerre polynomial of order n; in general, $\mathcal{L}_n(y) = \frac{e^y}{n!}\frac{d^n}{dy^n}(e^{-y}y^n)$.

A few remarks on the Wigner distributions that we have just introduced seem appropriate at this stage. First, we stress that $W(x,p)$ is a function of the real quantities x and p, used throughout this section, which *correspond to* the quadrature amplitudes $\hat{x}$ and $\hat{p}$ defined in the previous section – although the notation in

some textbooks might be misleading, the Wigner distribution is not a function of operators. In the same way, when we represent quantum states and their uncertainties as shown in Fig. 1.2, we implicitly consider the relation between Cartesian and polar coordinates given by

$$\begin{aligned} x &= \langle\alpha|\hat{x}|\alpha\rangle = \sqrt{2}|\alpha|\cos\phi\,, \\ p &= \langle\alpha|\hat{p}|\alpha\rangle = \sqrt{2}|\alpha|\sin\phi\,, \end{aligned} \tag{1.40}$$

and $\alpha = |\alpha|e^{\imath\phi}$.

The specific form of these transformations is determined by the definition of $\hat{x}$ and $\hat{p}$ (see Eq.(1.18)). Here Eq.(1.40) corresponds to $\alpha = (1/\sqrt{2})(x + \imath p)$. However, this is a special case of a more general expression, namely $\alpha = \mathsf{k}(x + \imath p)$ with k a positive real number. The Wigner distribution of the vacuum state for a generic k reads

$$W^{\mathsf{k}}_{\rm vacuum}(x,p) = \frac{2\mathsf{k}^2}{\pi}\, e^{-2\mathsf{k}^2(x^2+p^2)}\,, \tag{1.41}$$

which generalises Eq.(1.36); Heisenberg's principle becomes $\Delta x \Delta p = 1/(4\mathsf{k}^2)$. For $\mathsf{k} = 1/\sqrt{2}$ we recover our original formulae.

What is the form of the Wigner distribution in polar coordinates? Eq.(1.40) should make this task straightforward – except for a fundamental difference which distinguishes $(|\alpha|, \phi)$ from (x, p): while the latter variables are subject to the uncertainty relation, which in turn makes it possible to consider the general expression given by Eq.(1.41), the same is not true for polar coordinates. This is because of the additional constraint $|\alpha|^2 = \langle\hat{n}\rangle$: this equality restricts the flexibility of the $(|\alpha|, \phi)$

representation. We express the Wigner function of the vacuum in polar variables as

$$W_{\text{vacuum}}(|\alpha|,\phi) = \frac{2}{\pi}\, e^{-2|\alpha|^2} = \frac{2}{\pi}\, e^{-\frac{|\alpha|^2}{2(1/4)}}\,. \tag{1.42}$$

Quantum mechanics does not allow for alternative ways to generalise or reformulate this result. We see that the variance of the Gaussian function $W_{\text{vacuum}}(|\alpha|,\phi)$ is equal to 1/4, to be compared with $1/(4\mathsf{k}^2)$ in Cartesian coordinates (see Eq.(1.41)). The variance of the vacuum is thus determined by the chosen representation; depending on the specific calculation, it may then be convenient to consider variances which are expressed relative to this quantity. This observation will be useful in Chapter 3.

1.3 Coherence, entanglement and non-locality

Degree of optical coherence

In the introduction we discussed Glauber's contribution to a rigorous definition of quantum coherence. Mathematically, the degree of coherence of a given light field can be studied through correlation functions $\{G^{(n)}(\mathbf{x}_1,\ldots,\mathbf{x}_n,\mathbf{x}_{n+1},\ldots,\mathbf{x}_{2n})\}$ corresponding to n-photon detection events. In the following, we restrict our attention to coincidence events and study the second-order coherence of our experimentally generated quantum states. As we shall see shortly, this quantity takes on well-known values for the light fields discussed earlier – notably, a value below 1 is a signature of non-classicality. Higher-order functions such as $G^{(3)}$ allow for the characterisation of multi-mode mixed states [37].

We define the second-order correlation function as [33]

$$G^{(2)}(\mathbf{x}_1, \mathbf{x}_2, \mathbf{x}_3, \mathbf{x}_4) := \mathrm{Tr}\left[\hat{\rho}\, \hat{E}^{(-)}(\mathbf{x}_1)\hat{E}^{(-)}(\mathbf{x}_2)\hat{E}^{(+)}(\mathbf{x}_3)\hat{E}^{(+)}(\mathbf{x}_4)\right], \tag{1.43}$$

where $\mathbf{x}_i = (\mathbf{r}_i, t_i)$ for $i = 1, \ldots, 4$.

As we shall be interested in two-photon coincidence counting, we consider the special case given by $\mathbf{x}_3 = \mathbf{x}_2$ and $\mathbf{x}_4 = \mathbf{x}_1$. It is also convenient to introduce a normalised version of this function, $g^{(2)}(\mathbf{x}_1, \mathbf{x}_2, \mathbf{x}_2, \mathbf{x}_1)$, known as the second-order degree of coherence. We further restrict our attention to the degree of *temporal* coherence (that is, we refer to a single spatial mode of the radiation field); for a stationary light beam[6] we can then write

$$g^{(2)}(\tau) = \frac{\langle \hat{E}^{(-)}(t)\hat{E}^{(-)}(t+\tau)\hat{E}^{(+)}(t+\tau)\hat{E}^{(+)}(t)\rangle}{\langle \hat{E}^{(-)}(t)\hat{E}^{(+)}(t)\rangle^2}, \tag{1.44}$$

where τ is a relative temporal delay between detection events.

As the values taken by $g^{(2)}(\tau)$ for distinct light fields are most different when $\tau = 0$, we shall consider $g^{(2)}(0)$ – and refer to it as $g^{(2)}$ for brevity – from now on. In terms of creation and annihilation operators, the second-order degree of coherence reads

$$g^{(2)} = \frac{\langle \hat{a}^\dagger \hat{a}^\dagger \hat{a}\hat{a}\rangle}{\langle \hat{a}^\dagger \hat{a}\rangle^2}. \tag{1.45}$$

A coherent state is characterised by $g^{(2)} = 1$; a chaotic light source exhibits thermal statistics and yields $g^{(2)} = 2$. For the generic Fock state $|n\rangle$ we find $g^{(2)} = 1 - (1/n)$:

[6] In general this hypothesis does not hold for pulsed fields, in which case it also becomes relevant to account for the temporal resolution of the detectors [38].

a value of $g^{(2)}$ smaller than 1 is typical of non-classical fields.

The following necessary condition for coherence holds [2]: if $|g^{(j)}| = 1$ for $j \leq n$, then the considered quantum field exhibits nth-order coherence. The theoretical description developed by Glauber identifies the 'threshold value' of the powers in the field strengths such that we start to observe correlations between detection events, i.e. we cannot factorise the correlation functions anymore.

What does it mean for a quantum state to be 'slightly entangled'?

Another fundamental concept in the quantum theory of light is that of entanglement. In this context, the *correlation* between two physical systems, which we shall call A and B, implies that the measurement of some property of A has an effect on the information carried by B – although B was not directly observed. Given a bipartite system AB, the quantum state $|\Psi\rangle_{\mathrm{AB}}$ is said to be entangled (that is, it exhibits correlations with no classical analogue) if it cannot be factored as

$$|\Psi\rangle_{\mathrm{AB}} = |\Psi\rangle_{\mathrm{A}} \otimes |\Psi\rangle_{\mathrm{B}} \,. \tag{1.46}$$

This is a definition of entanglement which does not seem to leave room for unexpected turns. Yet this concept is significantly more subtle, as illustrated by the following example [39]. We consider a two-photon source which guarantees that each pair is emitted in orthogonal polarisation modes – for instance, one photon is horizontally polarised and its twin has vertical polarisation[7]. Mathematically,

[7] We shall describe this kind of two-photon source in the next chapter.

there are two ways to express this feature while taking into account the absence of knowledge about which photon is associated to a given polarisation state:

$$\begin{aligned}\hat{\rho}_{\mathrm{AB}} &= \frac{1}{2}\Big(|HV\rangle_{\mathrm{AB}}\langle HV|\Big) + \frac{1}{2}\Big(|VH\rangle_{\mathrm{AB}}\langle VH|\Big)\,, \quad \text{or} \\ \hat{\varrho}_{\mathrm{AB}} &= \frac{1}{2}\Big(|HV\rangle_{\mathrm{AB}} + |VH\rangle_{\mathrm{AB}}\Big)\Big((\langle HV|)_{\mathrm{AB}} + (\langle VH|)_{\mathrm{AB}}\Big)\,.\end{aligned} \tag{1.47}$$

Labels A and B identify the polarisation modes of the emitted photons, and H, V stand for the two considered polarisation states. We also adopted the shorthand notation $|H\rangle_{\mathrm{A}} \otimes |V\rangle_{\mathrm{B}} \equiv |HV\rangle_{\mathrm{AB}}$.

Both formulae represent valid options. Indeed, the effect of a projective measurement on one photon yields $\mathrm{Tr}\big[\hat{\rho}_{\mathrm{AB}}|H\rangle_{\mathrm{A}}\langle H|\big] = \mathrm{Tr}\big[\hat{\varrho}_{\mathrm{AB}}|H\rangle_{\mathrm{A}}\langle H|\big] = |V\rangle_{\mathrm{B}}\langle V|$ (and an analogous result is found if subsystem B is measured). Nevertheless, $\hat{\rho}_{\mathrm{AB}}$ and $\hat{\varrho}_{\mathrm{AB}}$ describe fundamentally different physical states: the former is not entangled, while the photon pairs described by $\hat{\varrho}_{\mathrm{AB}}$ are entangled in polarisation. While the first state exhibits only classical correlations, the second is characterised by 'two-particle coherences' which are purely quantum-mechanical [39]. If we compute the density matrices for both states, we find that ϱ_{AB} has two non-zero off-diagonal elements, referred to as coherences in the light of the example that we have just presented.

Besides the subtle difference between classical and quantum correlations manifested as entangled states of composite systems, a non-trivial task is to determine whether a given quantum state exhibits entanglement or not. This is because, given our current definition of entanglement, the answer to this question seems to rely exclusively on our ability to check if the studied state can be factored – yet what if

the initial expression makes the factorisation all but obvious? The Schmidt-mode analysis, or Schmidt decomposition, provides a powerful mathematical tool to tackle this issue as well as to quantify the degree of entanglement.

Let us consider a bipartite system (such as that of two light quanta or of an atom and a photon) in the pure state

$$|\Psi\rangle = \sum_{u=1}^{n} \sum_{v=1}^{\mu} C(u,v)\, |u\rangle \otimes |v\rangle \,. \tag{1.48}$$

Following the notation adopted in [39], we use Latin and Greek letters to distinguish the state spaces associated with the two subsystems. For a reason that will become clear later on, we specify that the finite dimensionalities of the considered subsystems, given by integers n and μ in the above summations, are such that $\mu \leq n$.

The Schmidt-mode analysis allows us to write any pure state $|\Psi\rangle$ of a bipartite system as follows:

$$|\Psi\rangle = \sum_{\varsigma=1}^{\mu} \sqrt{\lambda_\varsigma}\, |F^\varsigma\rangle \otimes |\Phi^\varsigma\rangle \,, \tag{1.49}$$

where $|F^\varsigma\rangle$ and $|\Phi^\varsigma\rangle$ are known as the Schmidt modes for $|\Psi\rangle$. These states form orthonormal bases in the state spaces of the two subsystems and are defined as

$$\begin{aligned} |F^\varsigma\rangle &= \sum_{u=1}^{n} f_u^\varsigma\, |u\rangle \,, \\ |\Phi^\varsigma\rangle &= \sum_{v=1}^{\mu} (\phi_v^\varsigma)^*\, |v\rangle \,. \end{aligned} \tag{1.50}$$

The complex coefficients f_u^ς and ϕ_v^ς are defined as the probability amplitudes between the basis vectors introduced above for the two subsystems, $\{|u\rangle\}$ and $\{|v\rangle\}$,

and new sets of basis states which correspond to the eigenvectors of the reduced density operators for each subsystem (that is, each coefficient denotes a specific basis transformation). The quantities $\{\lambda_\varsigma\}_{\varsigma=1,\ldots,\mu}$ in Eq.(1.49) are also related to the reduced density matrices as they are defined as their eigenvalues.

The Schmidt-mode analysis is tailored to a specific quantum state; every pure state of a given composite system has its own decomposition. It is also possible to show that the Schmidt-mode analysis for a given quantum state is not unique [40]. The first advantage given by the Schmidt decomposition is operational – instead of two summations (see Eq.(1.48)) we now only have to consider one. Importantly, Eq.(1.49) explains why we specified that $\mu \leq n$: the single summation goes to the smaller dimensionality. From a more fundamental viewpoint, the Schmidt-mode analysis informs us that a pure state is entangled if the sum in Eq.(1.49) contains more than one term.

We can refer to $\{\lambda_\varsigma\}$ as 'information eigenvalues'. Indeed, we know that $0 \leq \lambda_\varsigma \leq 1$ for all values of ς and that $\sum_\varsigma \lambda_\varsigma = 1$ as these are eigenvalues of density matrices. Consequently, $\lambda_\varsigma = 1$ indicates a factorable state, i.e. complete knowledge of the structure of $|\Psi\rangle$. Depending on how many terms appear in the Schmidt decomposition, the information contained in a given quantum state is more or less 'spread out' [39] – thus determining the number of projective measurements which must be performed on one subsystem in order to extract some information about the second. Therefore, the Schmidt-mode analysis provides both a characterisation of pure-state entanglement in bipartite systems and a quantitative measure of the degree of entanglement characterising a given state of the considered composite system.

A useful metric is given by the Schmidt number K, defined as

$$K = \frac{1}{\sum_{\varsigma=1}^{\mu} \lambda_\varsigma^2} = \frac{1}{\mathrm{Tr}[\hat{\rho}_{\mathrm{L}}^2]} = \frac{1}{\mathrm{Tr}[\hat{\rho}_{\mathrm{G}}^2]}\,, \tag{1.51}$$

where subscripts 'L' and 'G' refer to the Latin and Greek subsystems. The Schmidt number, given by the purity of either reduced density operator ($\hat{\rho}_{\mathrm{L}}$ or $\hat{\rho}_{\mathrm{G}}$), quantifies the effective number of terms in the decomposition; equivalently, it indicates how many modes in the considered Schmidt basis are 'active'. Indeed, we see that if $\lambda_{\bar{\varsigma}} = 1$ (for a fixed $\bar{\varsigma}$) we obtain $K = 1$. On the other hand, if all coefficients are equal this implies that $\lambda_\varsigma = 1/\mu$ for all ς, hence $K = \mu$ (which accounts once again for the right number of terms in the decomposition).

The above presentation of the Schmidt-mode analysis refers to finite-dimensional Hilbert spaces, as indicated by the finite number of terms in the summations. However, it is possible to transfer this approach to systems with infinite dimension; such extension is advantageous for the study of continuous degrees of freedom, as discussed in [41].

As a conclusion to this section, it is appropriate to stress once more that entanglement is a non-trivial concept representing a key feature of the quantum theory. There exist states for which it is not straightforward to assert whether they are or not entangled. Importantly, we remark that the very notion of entanglement depends on the way we partition the Hilbert space of a given composite system [12]. Moreover, we must note that a quantum state may show particle entanglement but no mode entanglement or vice versa (or both, as we shall see in the next chapter). In

this view, a classical state is neither particle- nor mode-entangled. This observation has significant consequences: it plays a fundamental role in the debate on the identification of the quantum resources – in the form of states which have either particle or mode entanglement, for example – responsible for the quantum enhancement of precision measurements [12].

Quantum mechanics and local realism

The properties of non-separable states were challenged in a seminal article by Einstein, Podolsky and Rosen (commonly referred to as the EPR paper) [42]. The goal of the authors was to show that the quantum theory is incomplete, a necessary condition for completeness being stated as follows: "every element of the physical reality must have a counterpart in the physical theory." [42]

The EPR paper builts on two assumptions:

> *The condition of reality.* "If, without in any way disturbing a system, we can predict with certainty [...] the value of a physical quantity, then there exists an element of physical reality corresponding to this physical quantity." [42]
>
> *The condition of locality.* If two systems are causally disconnected[8], the outcome of a measurement on one system cannot influence the result of a measurement on the other.

Additionally, we must keep in mind that quantum mechanics distinguishes between commuting and non-commuting observables (where by observables we mean opera-

[8]Two events with spatial and temporal separations Δy and Δt, respectively, are causally disconnected if $(\Delta y)^2 > c^2(\Delta t)^2$ (where c is the speed of light in vacuum).

tors corresponding to physical quantities); if $\hat{O}$ and $\hat{Q}$ do not commute, the physical quantities they represent cannot be simultaneous elements of physical reality as it is not possible to predict with certainty the outcomes of a simultaneous measurement of $\hat{O}$ and $\hat{Q}$.

The authors develop their argument by identifying two mutually exclusive statements: either "the quantum-mechanical description of physical reality [...] is not complete" [42], or the two physical quantities corresponding to two non-commuting operators cannot have simultaneous reality. Assuming that the quantum theory is complete, and under the hypotheses introduced above, Einstein and coworkers arrive at the conclusion that two physical quantities associated with non-commuting observables can be simultaneous elements of reality. Therefore, they deduce that the initial assumption of completeness of quantum mechanics is flawed. Interestingly, the EPR paper introduced entangled states of bipartite systems, that is, states characterised by 'strong' correlations between some properties of the subsystems (where, in fact, 'strong' stands for 'non-classical').

The EPR article sparked an intense debate on the interpretation of the quantum theory, and in the decades that followed a number of papers reformulated the 'thought experiment' proposed by Einstein and collaborators. If the EPR argument was correct, was there a way to make the quantum theory complete, and if yes how? One approach suggested that there exist local degrees of freedom which are unaccounted for in the standard treatment of quantum mechanics; when these parameters are included in an appropriate local variable theory (LVT), they 'cure' the probabilistic nature of measurement processes which characterises the quantum-

mechanical description of reality. 1964 marked a turning point: the formulation of the *Bell inequalities* transferred the debate from pen and paper to the laboratory. Bell derived the inequalities that bear his name assuming that the conditions of reality and locality are both valid hypotheses. Under these assumptions, he introduced

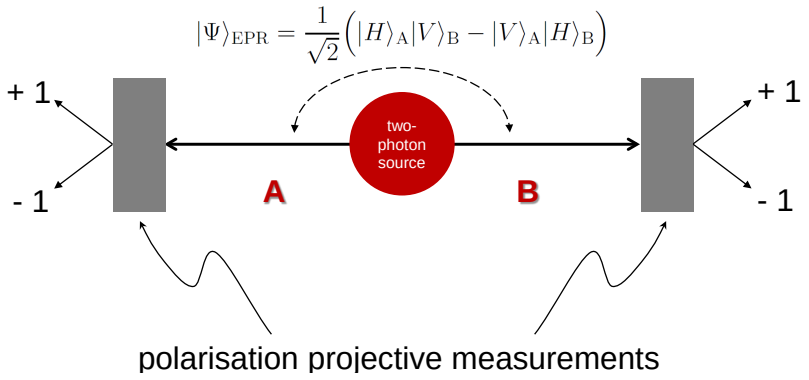

Figure 1.4 This schematic illustrates the layout for an experimental Bell test. A source delivers pairs of entangled photons over two modes (A and B); in this example the light quanta are encoded in polarisation. Each particle is sent to a detector performing projective measurements: in this specific implementation, we can think of a sequence of half-wave plate, polarising beam splitter (or, equivalently, a polariser) and a photon counter such as an avalanche photodiode (see Chapter 2) on each output arm. The measurement process yields dichotomic outcomes as the considered degree of freedom defines a two-dimensional space. For instance, we can associate the result '+1' to the detection of a horizontally polarised photon and '-1' to vertical polarisation; this identification varies as we project onto different polarisation bases by changing the orientation of the half-wave plate. For an appropriate choice of settings on the polarisation analyser, it is possible to construct the quantities – in the form of correlations between measurement results – which appear in a Bell inequality and thus verify if quantum mechanics contradicts the classical prediction thanks to the strong correlations present in the entangled state $|\Psi\rangle_{\mathrm{EPR}}$.

'hidden variables' which would explain the correlations exhibited by the measurement results on an 'EPR pair' (such as two photons emitted from a light source); Bell showed that this framework leads to a conclusion – expressed as a set of inequalities involving correlation coefficients – which can be contradicted by the corresponding

quantum-mechanical prediction [43]. Therefore, the experimental observation of a 'violation' of the inequalities derived from the LVT would confirm the validity of the quantum theory and cast doubts on a description of physical reality based on local hidden variables. There is now a considerable amount of literature reporting on the experimental violation of Bell inequalities in a variety of settings and for different systems [44–49]. In Fig. 1.4 we illustrate the schematic of an experiment performing a Bell test; this also highlights the dichotomic nature of the measurement results considered in the original inequalities.

In Chapter 4 we will discuss a generalisation of the original result obtained by Bell – the generalisation lying in the reformulation of the inequalities for measurements which produce non-dichotomic outcomes.

Chapter 2

Applied quantum optics

2.1 Beam splitter transformations

In the previous chapter we presented the classes of quantum states that we shall refer to in the following, and characterised these states in terms of the second-order degree of coherence. In the study of the correlations between field strengths (leading to first-order coherence) and field intensities (associated with $g^{(2)}$, as discussed in Chapter 1), interferometry occupies a fundamental place. The Mach-Zehnder interferometer and the setup proposed by Hanbury Brown and Twiss [3], for example, have become paradigmatic schemes in quantum optics. An essential element in such interferometric layouts is the beam splitter – a thin slab of partially reflective material which splits an incoming light beam to produce an output on a transmitted and a reflected spatial mode. This operation can lead to significant transformations of the input state such as the generation of entanglement. We shall thus start this chapter with a brief mathematical description of this optical component.

We consider the lossless beam splitter (BS) identified by two input and two output spatial modes as depicted in Fig. 2.1 **a**. As the atoms on the partially reflective

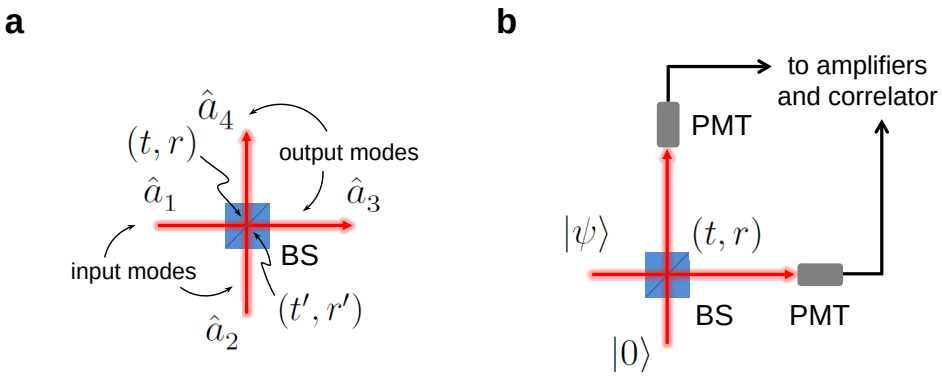

Figure 2.1 **(a)** The input and output modes of a beam splitter can be described by annihilation and creation operators as shown in this schematic. Each side of the partially reflective surface is characterised by a pair of transmission and reflection coefficients. **(b)** Given an unknown input state $|\psi\rangle$ impinging on the BS (and the vacuum on the other input port), this layout – known as the Hanbury Brown and Twiss interferometer – allows for the experimental measurement of second-order correlations between detection events recorded by photomultiplier tubes (PMTs) placed at each output.

surface are excited by the incoming radiation, they become themselves emitters of interfering spherical waves. This interference identifies specific emission modes out of the beam splitter, thereby producing coherent scattering of radiation. This process is described by a scattering matrix B:

$$B = \begin{pmatrix} t & r' \\ r & t' \end{pmatrix} \tag{2.1}$$

with $t, t', r, r' \in \mathbb{C}$, hence $t = |t|e^{\imath\vartheta}$, $t' = |t'|e^{\imath\vartheta'}$, $r = |r|e^{\imath\varphi}$ and $r' = |r'|e^{\imath\varphi'}$. t, t' and r, r' are called the transmission and reflection coefficients of the BS, respectively (see Fig. 2.1 **a**).

Energy must be conserved during the scattering process, hence the following algebraic conditions must hold:

$$|t|^2 + |r|^2 = |t'|^2 + |r'|^2 = 1, \quad t(r')^* + r(t')^* = 0\,. \tag{2.2}$$

The second part of Eq.(2.2) implies that $|r|/|t| = |r'|/|t'|$ and $\vartheta - \varphi' = \varphi - \vartheta' \pm \pi$. As a consequence, we must have $|t| = |t'|$ and $|r| = |r'|$.

The conditions that we have just listed guarantee that B is a unitary matrix, i.e. $B^{-1} = B^\dagger$; this follows from the conservation of energy between input and output modes. As long as the transmission and reflection coefficients satisfy the above requirements, the BS matrix can take on a number of forms – the most convenient choice is often determined by the specific phenomenon under study.

If we require all elements of B to be real, we can model the transformation performed by the beam splitter as a rotation matrix:

$$B = \frac{1}{\sqrt{2}} \begin{pmatrix} \cos\theta & -\sin\theta \\ \sin\theta & \cos\theta \end{pmatrix}\,. \tag{2.3}$$

In Chapter 3 we will use this form of B to describe the BS transformation of a two-mode input state given by a single photon and a coherent field.

Alternatively, we can choose $\vartheta = \vartheta' = 0$ in the expressions for t and t' (that is, $t, t' \in \mathbb{R}$). It follows that $-\varphi' = \varphi \pm \pi$ and the choice of φ' determines the final form

of B. For instance,

$$B = \frac{1}{\sqrt{2}} \begin{pmatrix} 1 & \pm\imath \\ \pm\imath & 1 \end{pmatrix} \tag{2.4}$$

corresponds to $\varphi' = \pi/2$ (plus sign) and $\varphi' = 3\pi/2$ (minus sign). We shall consider a slightly more general form of Eq.(2.4) in Chapter 4.

The modes which constitute inputs and outputs of the beam splitter can be associated to creation and annihilation operators as shown in Fig. 2.1 **a**. For example, to describe the case of a single-photon state in input mode 1 and the vacuum in mode 2 is empty, we can write $|\Psi\rangle_{\text{in}} = |1\rangle_1|0\rangle_2 \equiv \hat{a}_1^\dagger|0\rangle_1|0\rangle_2$ where the numerical subscripts identify the two input modes.

The creation and annihilation operators allow us to adopt a convenient matrix form to express the transformation operated by the BS:

$$\begin{pmatrix} \hat{a}_3^\dagger \\ \hat{a}_4^\dagger \end{pmatrix} = \frac{1}{\sqrt{2}} \begin{pmatrix} 1 & \imath \\ \imath & 1 \end{pmatrix} \cdot \begin{pmatrix} \hat{a}_1^\dagger \\ \hat{a}_2^\dagger \end{pmatrix}, \tag{2.5}$$

which in turn leads to the input-output relations

$$\begin{cases} \hat{a}_1^\dagger = \frac{1}{\sqrt{2}}\left(\hat{a}_3^\dagger - \imath\hat{a}_4^\dagger\right) \\ \hat{a}_2^\dagger = \frac{1}{\sqrt{2}}\left(-\imath\hat{a}_3^\dagger + \hat{a}_4^\dagger\right) \end{cases} \tag{2.6}$$

for the creation operators (and analogous formulae apply to $\hat{a}_1, \hat{a}_2, \hat{a}_3, \hat{a}_4$).

Let us consider a single-photon state arriving at the beam splitter from each input channel: the total input state is thus $|\Psi\rangle_{\text{in}} = \hat{a}_1^\dagger\hat{a}_2^\dagger|0\rangle_1|0\rangle_2$, which thanks to

Eq.(2.6) can be re-expressed as

$$\begin{aligned} |\Psi\rangle_{\text{out}} &= \frac{1}{2}\big(\hat{a}_3^\dagger - \imath\hat{a}_4^\dagger\big)\big(-\imath\hat{a}_3^\dagger + \hat{a}_4^\dagger\big) = \\ &= \frac{1}{2}\big(-\imath(\hat{a}_3^\dagger)^2 + \hat{a}_3^\dagger\hat{a}_4^\dagger - \hat{a}_4^\dagger\hat{a}_3^\dagger - \imath(\hat{a}_4^\dagger)^2\big) = \\ &= \frac{-\imath}{\sqrt{2}}\big(|2\rangle_3|0\rangle_4 + |0\rangle_3|2\rangle_4\big)\,. \end{aligned} \tag{2.7}$$

This is a striking result: quantum mechanics predicts that the two particles always exit the beam splitter in the same mode. This also means that if we were to put photodetectors in both output modes, for *two perfectly indistinguishable* particles we would expect not to record any coincident detection event. The destructive interference which determines this 'dip' in the coincidence counts has no classical analogue [33]. This effect is also referred to as bosonic coalescence: if we were to perform the same measurement with fermions, the Pauli exclusion principle would lead to vanishing probabilities associated with terms $|2\rangle_3|0\rangle_4$ and $|0\rangle_3|2\rangle_4$. What do we mean by 'perfectly indistinguishable' bosonic particles? As an example, it may happen that the arrival times of the two photons at the BS do not coincide, and one photon is slightly delayed with respect to the other. This makes the particles distinguishable with respect to the degree of freedom 'arrival time at the beam splitter': we thus expect that if we scan this time difference, the coincidence count rate will reach a minimum for the so-called zero-delay condition. This is precisely the experiment that Hong, Ou and Mandel conducted with pairs of photons interfering at a beam splitter which could be moved over micrometric distances in order to vary the optical path lengths relative to each other [50]. For this reason, we speak of

Hong-Ou-Mandel (two-photon) interference (HOMI) and Hong-Ou-Mandel 'dips' in coincidence counts.

In the HOM experiment, the BS is responsible for the creation of mode entanglement. With reference to the expression $|\Psi\rangle_{\rm in} = |1\rangle_1|1\rangle_2$, where subscripts identify the input modes, we see that the total input state is factorised. If we switch from mode to particle formalism, we need to take into account all possible permutations of the two particles. This leads to a symmetrised expression of the initial state which reads $|\Psi\rangle_{\rm in} = (1/\sqrt{2})(|\mathsf{m}_1\rangle_1|\mathsf{m}_2\rangle_2 + |\mathsf{m}_2\rangle_1|\mathsf{m}_1\rangle_2)$: here m_1 and m_2 identify the modes over which each photon can be found, while subscripts correspond to the two particles. This result shows that the state is particle-entangled. After the beam splitter, we know from Eq.(2.7) that the output state is $|\Psi\rangle_{\rm out} = (\imath/\sqrt{2})(|2\rangle_3|0\rangle_4 + |0\rangle_3|2\rangle_4) = (\imath/\sqrt{2})(|\mathsf{m}_1\rangle_1|\mathsf{m}_1\rangle_2 + |\mathsf{m}_2\rangle_1|\mathsf{m}_2\rangle_2)$, following the particle formalism that we have just introduced. The total output state is thus particle- and mode-entangled: the beam splitter introduces correlations between the output modes.

We now consider the interferometric layout depicted in Fig. 2.1 **b**. The degree of second-order coherence of an optical field was measured for the first time by Hanbury Brown and Twiss with a similar setup (although a rigorous definition of this quantity was given later by Glauber). At the output of the interferometer, we probe the photon-number correlations between the two output modes:

$$\langle \hat{n}_3 \hat{n}_4 \rangle = |r|^2|t|^2\langle \hat{n}_1(\hat{n}_1 - \hat{I})\rangle \,, \tag{2.8}$$

where $\hat{n}_3 = \hat{a}_3^\dagger \hat{a}_3$, $\hat{n}_4 = \hat{a}_4^\dagger \hat{a}_4$, (t, r) are the transmission and reflection coefficients of

the BS and $\hat{I}$ is the identity operator [33]. The expectation values are calculated on the total input state $|\Psi\rangle_{\text{in}} = |\psi\rangle_1|0\rangle_2$ (see Fig. 2.1) thanks to the BS input-output relations given by Eq.(2.6). The measured quantity $\langle\hat{n}_3\hat{n}_4\rangle$ is related to the degree of second-order coherence for the output field as

$$g^{(2)}_{3,4} = \frac{\langle\hat{n}_3\hat{n}_4\rangle}{\langle\hat{n}_3\rangle\langle\hat{n}_4\rangle} \equiv \frac{\langle\hat{n}_1^2\rangle - \langle\hat{n}_1\rangle}{\langle\hat{n}_1\rangle^2} = g^{(2)}_{1,1}\,. \tag{2.9}$$

We see that the statistical properties of the output state, represented by $g^{(2)}_{3,4}$, inform us about the photon statistics of the initial state present in mode 1 [33]. We will apply this formula in Chapter 4 to estimate the degree of second-order coherence of our experimentally generated quantum states.

2.2 Generation of quantum states

Chapter 1 offered a partial survey of the quantum states of light, from the wave-like coherent fields to the non-classical Fock states. How do we generate these fields in the laboratory? The output from a laser system approximates well a coherent state; in order to produce single photons and squeezing, we need to further manipulate the electromagnetic radiation generated by stimulated emission from a gain medium confined in an optical cavity – for example through a non-linear interaction with a dielectric material.

Among the many known non-linear processes where an electromagnetic field interacts with a medium characterised by a non-vanishing second-order susceptibility

$\chi^{(2)}$, parametric downconversion (PDC) occupies a most prominent role in quantum optics. PDC has been known to generate photon pairs since the sixties [51]; further studies showed that photon sources based on this process could facilitate the investigation of fundamental aspects of the quantum theory [46]. Interestingly, the HOMI experiment discussed in the previous section contributed to establishing PDC as a key tool for quantum information processing. Indeed, the characteristic drop in coincident detection events at the output of the BS as a function of the arrival times of the particles was observed with a photon source based on this parametric process [50]. The experiment highlighted that downconverted photons are created within (at least) sub-picosecond time intervals. Notably, the ability to produce pairs of photons in well-defined temporal (and spatial) modes is a major strength of parametric downconversion [52].

In general, an intense electromagnetic field interacting with a dielectric medium induces a non-linear response in the material. The induced polarisation of the medium creates the conditions for three-wave mixing – a class of phenomena where three electromagnetic fields interact in a material with $\chi^{(2)} \neq 0$. Under conservation of energy and momentum, frequency conversion can be then observed. In sum-frequency generation (SFG), two incident fields produce radiation at a frequency corresponding to the sum of the frequencies of the input fields[1]; similarly, difference-frequency generation (DFG) describes the production of an output field at a frequency equal to the difference of the two input frequencies. In PDC a single input (or pump) beam generates two output fields known as signal and idler, as illustrated in Fig. 2.2 **a**. As

[1]Second-harmonic generation (SHG) is a special case of SFG where the two input fields are degenerate in frequency.

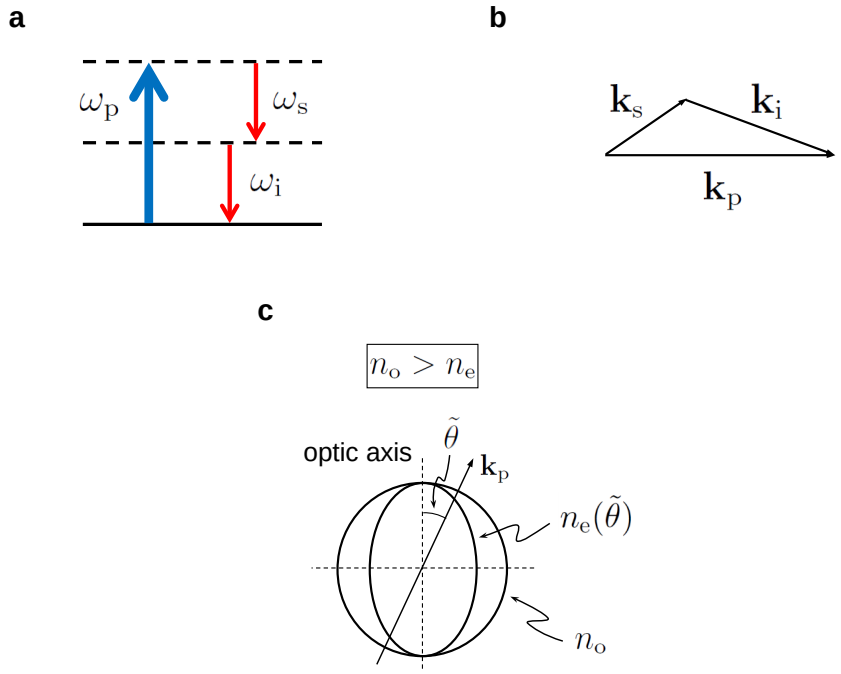

Figure 2.2 **(a)** Parametric downconversion is a special case of difference-frequency generation: here one pump photon at frequency ω_p creates two daughter photons, signal and idler, at frequencies ω_s and ω_i. **(b)** In parametric downconversion, energy and momentum must be conserved: this schematic illustrates the so-called phase matching condition, showing that for a given direction of the pump beam (and for a set orientation of the crystal, see text) the emission of downconverted photon pairs takes place in well-defined spatial directions. **(c)** In a negative uniaxial non-linear medium, the index of refraction n_o experienced by the 'ordinary beam' (or o-ray, see text) is higher than the angle-dependent extraordinary index $n_e(\tilde{\theta})$.

opposed to SFG and DFG, parametric downconversion can only be explained in a fully quantum-mechanical picture: vacuum fluctuations must be taken into account to explain the generation of output fields at frequencies lower than that of the pump. As already mentioned, the fields involved in the process of parametric downconversion must conserve energy and momentum in the non-linear medium, that is,

$$\omega_p = \omega_s + \omega_i, \qquad \mathbf{k}_p = \mathbf{k}_s + \mathbf{k}_i\,. \tag{2.10}$$

Subscripts 'p', 's' and 'i' stand for 'pump', 'signal' and 'idler'. The second relation is known as the phase matching condition (see Fig. 2.2 **b**): perfect phase matching is achieved when the wave vector mismatch $c\,\Delta k = \omega_{\mathrm{p}} n_{\mathrm{p}}(\omega_{\mathrm{p}}) - \omega_{\mathrm{s}} n_{\mathrm{s}}(\omega_{\mathrm{s}}) - \omega_{\mathrm{i}} n_{\mathrm{i}}(\omega_{\mathrm{i}})$ vanishes. However, $\Delta k = 0$ is a difficult condition to meet because of normal dispersion: in the range of values usually taken by ω_{p}, ω_{s} and ω_{i}, the index of refraction $n(\omega)$ is an increasing function of frequency. Consequently, perfect phase matching for three collinear beams, implying that $\omega_{\mathrm{p}} n_{\mathrm{p}}(\omega_{\mathrm{p}}) = \omega_{\mathrm{s}} n_{\mathrm{s}}(\omega_{\mathrm{s}}) + \omega_{\mathrm{i}} n_{\mathrm{i}}(\omega_{\mathrm{i}})$, could not be achieved while simultaneously satisfying the first expression in Eq.(2.10) [53]. While one natural solution to this issue would be to make use of anomalous dispersion, a most successful choice is to take advantage of the birefringent properties of many crystals: in these media, the index of refraction depends on the orientation of the electric field of the optical radiation (i.e. its polarisation). This approach rules out all isotropic media, leaving us to choose between uniaxial and biaxial crystals depending on whether the material has one preferential direction (or optic axis) or two. In the following we shall restrict our attention to uniaxial crystals. If the direction of the electric field for a given radiation is contained in the plane identified by the optic axis and the wave vector of the pump beam, the considered field is said to have extraordinary polarisation; light polarised in the perpendicular plane is characterised by ordinary polarisation. While the latter field (also called the 'o-ray') experiences an index of refraction n_{o}, extraordinary-polarised radiation (also referred to as the 'e-ray') experiences an index of refraction $n_{\mathrm{e}}(\tilde{\theta})$ which depends on the angle $\tilde{\theta}$ between the optic axis and $\mathbf{k}_{\mathrm{p}}$ as shown in Fig. 2.2 **c**. This means that by tuning the angular orientation of the crystal with respect to the direction of

propagation of the pump field it is possible – in principle – to achieve the condition of perfect phase matching [53]. We distinguish between three possible scenarios: in the type-0 phase matching configuration, all three fields have the same polarisation. If the two downconverted fields are both orthogonally polarised with respect to the pump we speak of type-I phase matching; the third option corresponds to the case where signal and idler are characterised by orthogonal polarisations and is referred to as type-II phase matching. An additional classification stems from the two existing types of uniaxial crystals: negative birefringent media are such that $n_{\mathrm{o}} > n_{\mathrm{e}}$, while in positive crystals $n_{\mathrm{o}} < n_{\mathrm{e}}$. All experimental work reported in this thesis refers to negative uniaxial birefringent materials.

What quantum states can we produce with a 'parametric downconverter' based on the process that we have just described? In a *simplified* quantum-mechanical picture, the annihilation of one pump photon at frequency ω_{p} is followed by the creation of two daughter photons at frequencies ω_{s} and ω_{i}. If we assume that the pump beam is bright, we can treat this field classically and include it in the interaction Hamiltonian $\hat{H}_{\mathrm{int}}$ for the process through its complex amplitude α_{p} only. We thus write $\hat{H}_{\mathrm{int}} = \imath\hbar\xi(\alpha_{\mathrm{p}}^{*}\hat{a}_{\mathrm{s}}\hat{a}_{\mathrm{i}} - \alpha_{\mathrm{p}}\hat{a}_{\mathrm{s}}^{\dagger}\hat{a}_{\mathrm{i}}^{\dagger})$, where ξ is known as the interaction strength and α_{p} is the complex amplitude of the input field. Consequently, we define an operator of temporal evolution $\hat{U}(t) = e^{-\frac{\imath}{\hbar}\hat{H}_{\mathrm{int}}t}$ which reads

$$\hat{U}(t) = e^{\mathsf{g}^{*}\hat{a}_{\mathrm{s}}\hat{a}_{\mathrm{i}} - \mathsf{g}\hat{a}_{\mathrm{s}}^{\dagger}\hat{a}_{\mathrm{i}}^{\dagger}} \tag{2.11}$$

with $\mathsf{g} = \xi\alpha_{\mathrm{p}}t = \mathsf{r}e^{\imath\theta}$ and $\mathsf{r} = |\mathsf{g}| = \xi|\alpha_{\mathrm{p}}|t$. Application of the Baker-Campbell-

Hausdorff formula [54] to this operator yields

$$\hat{U}(t) = e^{\lambda \hat{a}_{\rm s}^\dagger \hat{a}_{\rm i}^\dagger} e^{-\Lambda(\hat{a}_{\rm s}^\dagger \hat{a}_{\rm s} + \hat{a}_{\rm i}^\dagger \hat{a}_{\rm i} + \hat{I})} e^{-\lambda \hat{a}_{\rm s} \hat{a}_{\rm i}} \,, \tag{2.12}$$

where we defined $\lambda = e^{\imath\theta} \tanh \mathsf{r}$ and $\Lambda = \ln(\cosh \mathsf{r})$. We now consider the state given by $|\Psi\rangle_{\rm out} = \hat{U}(t)|0\rangle_{\rm s}|0\rangle_{\rm i}$, where $|0\rangle_{\rm s}|0\rangle_{\rm i}$ is the initial state of the signal and idler fields. From right to left, we see from Eq.(2.12) that the first and second terms produce the vacuum state $|0\rangle_{\rm s}|0\rangle_{\rm i}$. However, when we apply the third operator to the vacuum we obtain

$$\begin{aligned} |\Psi\rangle_{\rm out} &\propto e^{\lambda \hat{a}_{\rm s}^\dagger \hat{a}_{\rm i}^\dagger} |0\rangle_{\rm s}|0\rangle_{\rm i} \simeq \\ &\simeq \left[\hat{I} + \lambda \hat{a}_{\rm s}^\dagger \hat{a}_{\rm i}^\dagger + \frac{\lambda^2}{2} (\hat{a}_{\rm s}^\dagger)^2 (\hat{a}_{\rm i}^\dagger)^2 + \dots \right] |0\rangle_{\rm s}|0\rangle_{\rm i} \,, \end{aligned} \tag{2.13}$$

We see that signal and idler modes are always populated with the same number of photons. Indeed, the exact expression for the state exiting the downconverter reads

$$|\Psi\rangle_{\rm out} = \sum_{n=0}^{+\infty} c_n |n\rangle_{\rm s}|n\rangle_{\rm i} \,, \tag{2.14}$$

with $c_n = (1/\cosh \mathsf{r})\, e^{\imath n\theta} (\tanh \mathsf{r})^n$ [40].

If we compare $\hat{U}(t)$ to the operator $\hat{S}(\zeta)$ defined in Chapter 1 for a single-mode field, we recognise the evolution operator as the two-mode squeezing operator: its action on the vacuum state produces the squeezed state given by $|\Psi\rangle_{\rm out}$, which is an entangled two-mode state with perfect photon-number correlations between the two modes. Recalling the definition of the complex parameter λ, namely $\lambda = e^{\imath\theta} \tanh \mathsf{r}$,

we can rewrite the two-mode squeezed vacuum state as

$$|\Psi\rangle_{\rm out} = |\Psi\rangle_{\rm squeezed} = \sqrt{1-|\lambda|^2}\sum_{n=0}^{+\infty}\lambda^n|n\rangle_{\rm s}|n\rangle_{\rm i}\,. \tag{2.15}$$

We shall refer to this expression later on. λ is also called the squeezing parameter: it is a function of two variables, r and θ, which are closely related to the specific interaction considered as well as to the properties of the pump beam. The quantity $\mathsf{r} = |\mathsf{g}| = \xi|\alpha_{\rm p}|t$ is known as the non-linear gain because it is determined by the strength and duration of the interaction, as well as by the intensity of the pump. Importantly, the phase term in λ comes from the complex amplitude $\alpha_{\rm p}$: the output state inherits some of its features directly from the pump field.

We further note that Eq.(2.14) corresponds to the Schmidt decomposition (see Chapter 1) for the (ideal) two-mode squeezed vacuum state considered in this section. Although we did not stress this aspect in the previous chapter, one advantage of the Schmidt-mode analysis is that it leads rather naturally to the expression of the state which describes each subsystem: here the 'partitions' of the composite system correspond to the signal and idler modes. We find [40]

$$\hat{\rho}_{\rm s} = \frac{1}{(\cosh\mathsf{r})^2}\sum_{m=0}^{+\infty}(\tanh\mathsf{r})^{2m}|m\rangle_{\rm s}\langle m| \tag{2.16}$$

for the reduced density operator associated with the signal field; a similar result applies to the idler mode. Eq.(2.16) describes a chaotic state of the electromagnetic field, i.e. a radiation characterised by thermal statistics and mean photon number

$\langle \hat{n}_{\mathrm{s}} \rangle = (\sinh \mathsf{r})^2$ [40]. For a pure state of a composite bipartite system, each 'partition' is found in a maximally mixed state given by a thermal field with fixed average energy (specified by the non-linear gain $|\mathsf{g}|$, in this case) [55].

In conclusion, it is appropriate to clarify why we termed this description of PDC 'simplified'. Substituting the electric fields in the interaction Hamiltonian with single-mode creation and annihilation operators does not account for the spatial, temporal and spectral correlations between daughter photons, an aspect which is highlighted in a more general study of parametric downconversion. The spatial dependence demands an integration of the fields over the length of the crystal (if we refer to a collinear configuration), while the relevant temporal scale is given by the interaction time (essentially determined by the pulse length in the case of a pulsed laser system); the positive and negative frequency parts of the electric fields are not, in general, monochromatic. A more realistic form for $|\Psi\rangle_{\mathrm{out}}$ is $|\Psi\rangle_{\mathrm{out}} \propto \int\int f(\omega_{\mathrm{s}}, \omega_{\mathrm{i}})\, \hat{a}_{\mathrm{s}}^{\dagger}(\omega_{\mathrm{s}}) \hat{a}_{\mathrm{i}}^{\dagger}(\omega_{\mathrm{i}})\, |0\rangle_{\mathrm{s}} |0\rangle_{\mathrm{i}} d\omega_{\mathrm{s}} d\omega_{\mathrm{i}}$ (plus a vacuum term which we omitted), where we consider all frequencies allowed by Eq.(2.10). The function $f(\omega_{\mathrm{s}}, \omega_{\mathrm{i}})$ is called the joint spectral amplitude (JSA) distribution of the photon pairs created by PDC; it is determined by the pump distribution $\alpha(\omega_{\mathrm{s}}+\omega_{\mathrm{i}})$ and the phase matching function $\tilde{f}(\omega_{\mathrm{s}}, \omega_{\mathrm{i}})$. This framework is important for understanding the differences between the states produced by parametric downconversion in the continuous-wave regime and with a pulsed pump field. Notably, the photons produced in a pulsed type-II PDC process are characterised by different spectral distributions [56]; in turn, this means that downconverted photons carry information which makes them distinguishable. This key aspect must be taken into account in HOM-type experi-

ments, for example, as well as for the design of sources of pure single photons with high production rates. With reference to the latter goal, let us suppose that we operate a pulsed downconverter at very low gain so that high-order photon terms in Eq.(2.15) are negligible. We could then envisage a scheme where the detection of an idler photon, for instance, heralds the presence of its twin on the signal mode, thus delivering a probabilistic single-photon source. This heralding approach is in fact commonly adopted in quantum optics laboratories; however, its success depends strongly on the form of the JSA. This is because $f(\omega_{\rm s}, \omega_{\rm i})$ is such that, in general, the state of the signal photon upon detection of the idler photon is not projected onto a pure state due to spectral correlations between signal and idler; this ultimately decreases the quality of the source [52]. To solve this problem, one can apply tight spectral filtering in the heralding mode. Alternatively, it is possible to show that a factorable JSA leads to heralded pure single photons; the latter condition can be achieved by careful engineering of the PDC process in type-II crystals through asymmetric group velocity matching inside the non-linear medium [57, 58].

In the same way, $|\Psi\rangle_{\rm squeezed}$ (see Eq.(2.15)) corresponds to an ideal process. Often we will operate with a multi-mode squeezer, where signal and idler will exhibit spectral correlations which may not be limited to the ones discussed above [38]. In a general study of frequency multi-mode PDC for the production of squeezing, it is useful to include the statistical properties of the output state, such as its degree of second-order coherence, and relate this to a quantity which expresses how far from a spectrally uncorrelated JSA the parametric source is. The latter is provided by the Schmidt number K defined in the previous chapter: in this case it indicates how

many frequency modes are effectively 'active' in the squeezer. It is possible to show that the following relation holds [59]:

$$g^{(2)} \simeq 1 + \frac{1}{K} \tag{2.17}$$

under the assumption of a small squeezing parameter. We will make use of Eq.(2.17) in Chapter 4 to calculate the values of $g^{(2)}$ associated with our experimental states.

2.3 Detection of quantum states

In order to characterise the performance of a source of quantum states or the success of a given protocol in quantum information processing, we must be able to detect the quantum resources that we produce and manipulate in experimental quantum optics, be they single photons or bright squeezed states. In Chapter 1 we stressed how the CV/DV distinction pertains more to the choice of degrees of freedom that we set out to observe rather than to a conceptual difference. Similarly, the design of a detection system is determined both by the adopted source of quantum states as well as by the specific aspect that we wish to investigate.

One way to classify detectors is to ask the following question: does the detection system reveal the properties of a state at the single-photon-level, such as its photon statistics, or does it measure wave-like quantities related to its field quadratures? This approach does not do justice to the variety of existing photodetectors, but it does suit the purpose of the present section, which is to highlight the features of

detection schemes belonging to these two categories.

It is customary to characterise modern single-photon detectors in terms of a set of parameters which encompass their expected behaviour in response to an incoming signal. This type of characterisation should not be confused with detector tomography, which provides the complete description of the considered device by reconstruction of its projection operators. Rather, this is a somewhat operational characterisation which is often sufficient to analyse and interpret the data collected with a given detection system. The spectral range of a single-photon detector is the starting point in the design of an experiment, as every photon counter is only sensitive to an interval of wavelengths determined by the materials used. This aspect motivated the popular choice of near-infrared wavelengths for optical layouts, as most commercial detectors cover this region. However, with the growing interest in applications of QIP to communication protocols, experiments have been shifting towards telecommunication wavelengths ($\lambda \simeq 1550\,\mathrm{nm}$), where losses in optical fibres are also minimal. This has spurred intense research into efficient detection at these frequencies. Other relevant parameters in a single-photon detector include the dead time, its dark count rate and the timing jitter [60]. The recovery time (or dead time) follows the absorption of a photon, and indicates the interval during which the detector can potentially 'miss' incoming light quanta; it thus limits the photon count rate of the detection system. Every detector suffers from a temporal delay between the absorption of a photon and the generation of the corresponding electrical signal: the variation in this delay (over a given acquisition time) is quantified by the jitter. Finally, while detectors are expected to 'click' in the presence of one light particle

– and often one *or more* – this is not always the case: photodetectors produce false counts, also referred to as dark counts, which are due to the intrinsic properties of the materials and/or to external noise sources (such as scattering or fluorescence from a crystal). This effect can significantly jeopardise data acquisitions which aim at reconstructing the photon statistics of a given state, for instance. It is therefore important to limit as much as possible the influence of external noise and (if it is indeed non-negligible) estimate the residual contribution from dark counts prior to an experiment.

In the following, we shall be mostly concerned with the efficiency of detection η. This parameter quantifies the probability of registering a count as a photon hits the considered detector. While this is not the only relevant quantity, as illustrated by the above list of additional features, it is a most significant variable in the experiments discussed in this thesis as the overall η is determined by a number of loss factors characteristic of the design of our detection layout. The Klyshko calibration method is an elegant technique widely used to estimate the efficiency of a detector [61]. Interestingly, it relies on a source of correlated photon pairs such as the one based on PDC that we discussed in the previous section. In this case two detectors, the test and the trigger, record counts and coincidences (that is, 'simultaneous' counts) coming from the signal and idler beams. Let N be the total number of photon pairs produced by the source over the data acquisition time; η_{test} and η_{tr} denote the efficiencies of the test and trigger detectors. We then have that $N_{\text{test}} = \eta_{\text{test}} N$ and $N_{\text{tr}} = \eta_{\text{tr}} N$ for the counts registered in each channel, while $N_{\text{c}} = \eta_{\text{test}} \eta_{\text{tr}} N$ gives the number of total coincidence counts. Consequently, the efficiency of the test de-

tector can be computed as $\eta_{\rm test} = N_{\rm c}/N_{\rm tr}$. We stress that all efficiencies quoted in the present work are detection efficiencies, and we shall refer again to the Klyshko calibration method where appropriate.

Established technologies for single-photon detectors are given by photomultiplier tubes (used in the Brown-Twiss experiment – see Fig. 2.1 **b**) and avalanche photodiodes (APDs); superconducting nanowire detectors constitute a promising alternative solution. One of the main drawbacks of these detectors is that they cannot truly count photons – their response is binary, and may be crudely described as 'nothing' (corresponding to the projector $|0\rangle\langle 0|$) or 'something' (that is, $\hat{I} - |0\rangle\langle 0|$). Interestingly, we now know that detectors such as superconducting transition edge sensors produce electronic signals which are intrinsically proportional to the number of absorbed particles [60]. Alternatively, it is possible to use standard detectors to build arrays which provide the desired photon-number resolution through either spatial or temporal multiplexing; this approach is all the more successful when the binary photon counters exhibit high efficiencies [62]. In this thesis we will consider a detection system based on time multiplexing and standard avalanche photodiodes.

Photon counters measure quantities related to the intensity (or photon number) of the electromagnetic field, and have thus been successfully applied to the reconstruction of the density matrices as well as to the characterisation of protocols or gates for applications to quantum information and computing. As we shall see in the following, knowledge about the way a detector 'clicks' in response to an incoming beam indicates how to elaborate reliable and robust strategies to infer the desired information on the observed state from the counts produced by the detectors. Is

it possible to access directly the field quadratures as we do with field intensities? Unfortunately, the response of photodetectors to oscillating electric fields is slower than the frequencies of optical signals [14], thus preventing any direct measurement of the values of $\langle\hat{x}\rangle$ and $\langle\hat{p}\rangle$. We also remark that these quantities are defined up to a phase factor (see Chapter 1), hence we look for a detection system with added phase sensitivity. Once more, interferometry offers a valid solution with optical homodyne detection. In this technique we interfere the signal that we wish to probe with a bright field, known as the local oscillator (LO), which provides a phase reference and at the same time acts as a filter 'amplifying' the quantum fluctuations of the quadratures associated with the unknown signal. The brightness of the reference beam ensures that its phase and amplitude do not fluctuate significantly; from the interference process we expect a term where both amplitudes of the fields appear, and from which we can therefore extract the desired information about the quantum phase space distribution of the signal.

As illustrated in Fig. 2.3, we consider a beam splitter such that $t \in \mathbb{R}$ and $r = \imath|r|$ and two input fields identified by modes $\hat{a}$ and $\hat{b}$. We can make use of the BS input-output transformations (see Eq.(2.6)) to express the fields detected by two linear photodiodes placed on both output arms: if $\hat{c}$ and $\hat{d}$ describe the output modes, the detectors measure the intensities given by $\langle\hat{c}^\dagger\hat{c}\rangle$ and $\langle\hat{d}^\dagger\hat{d}\rangle$. Additionally, we assume that the reference field in mode $\hat{b}$ is in a coherent state $|\beta\rangle$, hence $\hat{b}|\beta\rangle = |\beta|e^{\imath\phi}|\beta\rangle$. The intensities recorded by the detectors at the output of the BS read

$$\langle\hat{c}^\dagger\hat{c}\rangle \simeq |r|^2|\beta|^2 + t|r\beta|\langle\hat{x}_{-\phi-\pi/2}\rangle\,, \quad \langle\hat{d}^\dagger\hat{d}\rangle \simeq t^2|\beta|^2 - t|r\beta|\langle\hat{x}_{-\phi-\pi/2}\rangle\,, \tag{2.18}$$

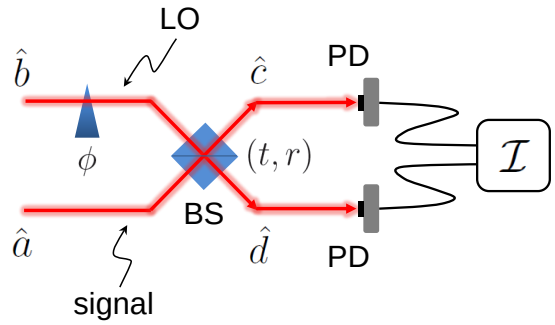

Figure 2.3 This sketch includes the main features of a strong-field optical homodyne detection system: the signal to probe and a bright coherent field providing a phase reference (indicated as ϕ here) interfere on a beam splitter. Linear photodiodes (PDs) are placed on both output arms.

where the '$\simeq$' sign indicates that these formulae hold if the LO is significantly brighter than the signal (that is, $\langle \hat{a}^\dagger \hat{a} \rangle \ll \langle \hat{b}^\dagger \hat{b} \rangle$). As a consequence, if we now consider the difference of currents $\mathcal{I} = \langle \hat{c}^\dagger \hat{c} \rangle - \langle \hat{d}^\dagger \hat{d} \rangle$ we find

$$\mathcal{I} = (1 - 2t^2)|\beta|^2 + 2t|r\beta|\langle \hat{x}_{-\phi-\pi/2} \rangle = |\beta|\langle \hat{x}_{-\phi-\pi/2} \rangle \equiv |\beta|\langle \hat{x}_\theta \rangle \tag{2.19}$$

with $\theta = -(\phi + \pi/2)$. In the second passage we assigned specific values to the transmission and reflection coefficients, i.e. $t = |r| = 1/\sqrt{2}$ (see Eq.(2.4)).

This is a notable result: the measurement of the difference of intensities $\mathcal{I}$ provides us with the expectation value of the phase-dependent quadrature $\hat{x}_\theta$ of the unknown input field. As we vary the phase ϕ of the reference beam, we probe different points in quantum phase space because θ is determined by ϕ; moreover, Eq.(2.19) highlights the amplification of the quadrature fluctuations operated by the local oscillator in the form of the multiplicative factor $|\beta|$. The scheme that we have just discussed is termed *balanced* homodyne detection because it monitors both output

modes, and thus makes it possible to compute a quantity which is proportional to $\hat{x}_\theta$ (and does not depend on the additional contributions from the reflected/transmitted component of the bright LO – see Eq.(2.18)). This technique is often referred to as strong-field homodyne detection to stress the requirement of a bright reference beam. This aspect is particularly relevant in this thesis, as we will discuss an alternative implementation of optical homodyning where the intensity of the local oscillator is comparable to that of the unknown signal: for this reason, we shall speak of weak-field homodyne detection.

Chapter 3

Hybrid schemes in quantum optics

In this chapter we move from the general framework that we have just surveyed to the topic which is the focus of this thesis – the implementation of schemes combining the CV and DV descriptions of quantum-optical phenomena. As discussed in the introduction, this 'hybrid' character can identify either the state preparation or the detection stage in a given experiment or protocol. In the present chapter we study the capabilities of a detection system which brings together a specific kind of homodyning layout and photon counters with added photon-number resolution in a two-mode geometry. We present the operating principle of our scheme, postponing the more technical details to Chapter 4. We then discuss a first test for this setup by considering the detection of a two-mode squeezed vacuum state. Precisely, we investigate how (and how well) it is possible to reconstruct key information about this resource – in our case, its photon statistics and the values of its variances.

This chapter is structured as follows: the first section offers a brief review of the weak-field homodyne detection technique. In the second section we derive a num-

ber of key results for single- and two-mode quantum states: we discuss the relation between counting and photon statistics, and derive explicit expressions for the distribution of photons associated with a generic input state measured with our WFH detectors. The third section draws the existing connection between photon statistics and representations in quantum phase space. This naturally leads to our first experimental investigation, which is discussed in the same section.

3.1 Weak-field homodyne detection

In the design of an optical experiment, detection is a key component. A suitable choice of detectors can inform about the success of a specific quantum operation or protocol. Alternatively, one may wish to characterise a given detection system, for example by performing quantum detector tomography. In Chapter 2 we introduced two main classes of detection devices: single-photon detectors, which count light quanta with varying degrees of discrimination between distinct 'click' events, and detectors which measure wave-like properties of the radiation field such as their quadratures. At first sight, this picture of photodetection may appear exhaustive. Avalanche photodiodes are suitable if one is interested in the discrete-variable description of quantum states: they are indeed among the preferred tools for measuring qubits. On the other hand, homodyne detection refers to the continuous-variable standpoint; as such, it allowed for pioneering experiments with squeezed states of light throughout the nineties [15], and it is now a well-established and prominent detection technique [11].

What happens if one combines the homodyne scheme with photon counting? In 1987 Ou, Hong and Mandel suggested a variant of standard homodyning: instead of considering the difference between the signals from two linear diodes (see Chapter 2, Section 2.3), the authors proposed to record coincidence counting events (in the form of intensity correlations) to detect squeezing [63]. The following year, Grangier and coworkers adopted an analogous scheme to experimentally demonstrate a new violation of Bell's inequalities. They described their detection scheme as "a mixture of homodyne [...] and intensity correlations techniques" [22]. Notably, their local oscillators (two beams in this case, to probe a two-mode state) were 'weak': the intensities were chosen to be of the same order of magnitude as the intensity of the probed signal – as opposed to the bright reference beams used in strong-field homodyne detection. Subsequently, avalanche photodiodes measured the intensity correlation function between the relevant output modes. In the nineties, analogous and independently developed hybrid detection schemes were discussed by Wallentowitz and Vogel and by Banaszek and Wódkiewicz [23, 27]. Later, Kuzmich, Walmsley and Mandel recast the proposal by Grangier and collaborators into the framework of pulsed laser systems – instead of a continuous-wave (cw) source – for the generation of the signal and the local oscillators [25].

The scheme introduced by Kuzmich and coauthors is the closest to the layout that we shall consider in the rest of this thesis. We term weak-field homodyne (WFH) detection a hybrid measurement technique which encompasses elements of the wave-like and particle-like frameworks for quantum state detection, as illustrated in Fig. 3.1 for a single-mode state. A signal is interfered on a beam splitter with

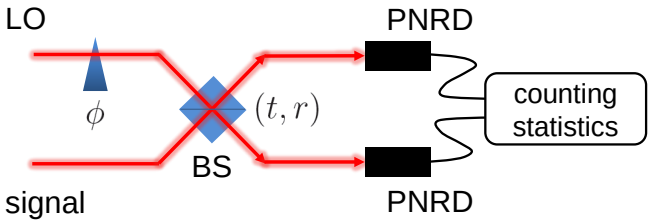

Figure 3.1 The weak-field homodyne detector considered in this thesis relies on the interference of a given signal with a 'weak' local oscillator (LO). We note that the LO phase can be set to an arbitrary value ϕ. The two beams are mixed on a beam splitter (BS) with tunable transmission and reflection coefficients (t, r): both modes of the resulting output state are measured with a photon-number-resolving detector (PNRD). An alternative scheme discards one of the two output modes.

a local oscillator described by the coherent state $|\alpha\rangle$ (and $\alpha = |\alpha|e^{\imath\phi}$). The beam splitter is characterised by its transmission and reflection coefficients (t, r); as we shall see in the following, the most interesting configurations are the balanced one, i.e. $|t| = |r| = 1/\sqrt{2}$, and the case where $|t| \gg |r|$. The intensity of the reference beam is comparable to that of the probed signal – in this sense, the LO is 'weak'. Photon-number-resolving detectors (PNRDs) measure the resulting two-mode output state: in this thesis we shall consider PNRDs based on mode multiplexing and commercially available avalanche photodiodes.

Naively, one could then interpret the choice of a weak coherent state as a condition imposed by the PNRDs: a bright LO would saturate the single-photon detectors and compromise their correct operation. Nonetheless, it is more correct to view this choice as inherent to the detection technique: in the same way as the standard homodyne scheme requires the reference beam to be bright in order to amplify quadrature fluctuations against noise that would otherwise hinder their detection (see Eq.(2.19)), weak-field homodyning captures information about the observed

state through phase-dependent coincidence counting statistics derived from the interaction of the quantum signal with a coherent state of comparable intensity.

Fig. 3.2 shows a graphical overview of the main schemes adopted for homodyne detection with photon counters over the past three decades.

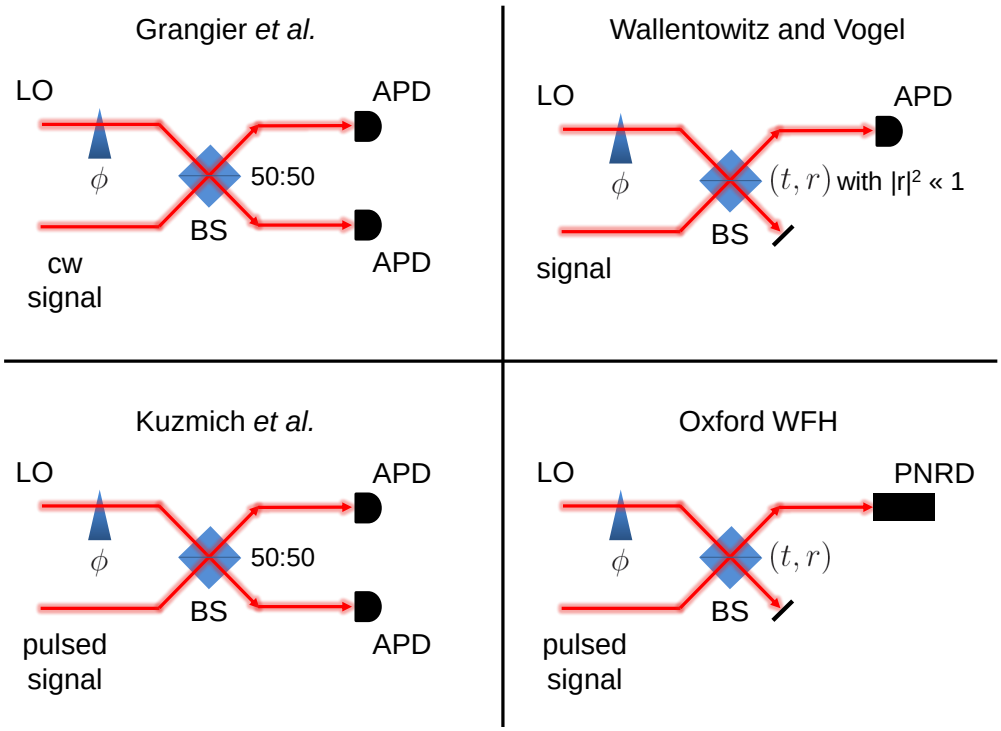

Figure 3.2 These are examples of homodyne detection schemes combined with photon counting reported in the literature. The layouts by Grangier *et al.* and Kuzmich *et al.* are referred to as balanced because both output modes are measured with photon counters. By contrast, our scheme is closer to that of Wallentowitz and Vogel in that it is unbalanced. However, we use PNRDs in place of 'on-off' photodiodes, and we take advantage of the tunability of the interference beam splitter by setting (t, r) according to the considered experiment.

3.2 Phase-dependent detection probabilities

What information do we record about the output state in Fig. 3.1 with photon-number-resolving detectors in the form of mode multiplexers? How reliable is the reconstruction of the distribution of photons in the measured state, and what are the factors limiting the quality of the recorded data? These are the questions that we consider in this section.

3.2.1 Counting and photon statistics

Depending on the technical specifications of the considered photon counter, factors such as loss, dark counts, afterpulsing and saturation affect the detection process to different degrees. When photon-number resolution is achieved by mode multiplexing, it is also necessary to take into account how the incoming light particles distribute themselves among the available detection modes, be they spatial or temporal. In general, we must distinguish between the counting statistics recorded by a given detector and the photon statistics associated with the measured light field. The former represent the information provided by the detection system through appropriate acquisition of the generated electrical signals. The photon distribution, by definition, informs us about the statistics which characterise the quantum resource initially prepared. Photon-number-resolving detectors such as those considered in this work illustrate well the intrinsic difference between the two considered quantities [64]. Interestingly, both distributions provide important information about the observed quantum resource.

We first set out to find an expression that relates the counting statistics to the distribution of photons for a generic single-mode quantum state. To do so, we start by considering the effect of mode multiplexing on the detection of n photons. We formulate the following question: given n 'billiard balls' randomly distributed among K bins, what is the probability that k bins are populated? We note that we can treat photons as independent billiard balls because PNRDs are not phase-sensitive by construction, hence any coherence existing between the incoming particles is lost upon detection [65]. If p_k is the probability of recording k counts and f_n is the probability that n photons are incident on the detector, we have that

$$p_k = \sum_n P(k|n) f_n \,, \tag{3.1}$$

where $P(k|n)$ is a conditional probability.

If we let k and n take on a range of non-negative integer values, we see that the set of conditional probabilities is conveniently cast into the form of a conditional probability matrix $\mathbf{C}$ whose generic element is $C_{kn} = P(k|n)$. Similarly, we can build a vector $\mathbf{p}$ of counting probabilities $\{p_k\}$ and a vector $\mathbf{f}$ with components given by the quantities $\{f_n\}$. The relation between the distributions of counts and photons thus reads, in matrix form,

$$\mathbf{p} = \mathbf{C} \cdot \mathbf{f} \,. \tag{3.2}$$

How do we compute the quantities $\{C_{kn}\}$? We make a few initial assumptions [65]:

- We ignore afterpulsing and dark counts associated with the detector. This

hypothesis implies that it is not possible to produce a number of counting events exceeding the number of incident particles. Therefore, we write that $P(k|n) = 0$ for all $k > n$, $P(k|0) = 0$ for $k \neq 0$ and $P(0|0) = 1$. From an experimental point of view, this assumption can be justified by the use of a trigger signal to gate counts and coincidence events, as well as by the moderate brightness of the source producing the studied quantum states.

- We consider a lossless detection device[1]. This means that, for $n = 1$, $P(1|1) = 1$: the impinging single photon must occupy one detection mode.

Given our mode multiplexer with K available detection modes, we associate a weight w_i to each of them. The quantity w_i represents the probability that mode i is populated. Ideally, all weights should be the same, i.e. $w_i = 1/K$ for all i; however, this does not hold for a realistic photon-number-resolving detector. Conservation of probability imposes that

$$\left(\sum_{i=1}^{K} w_i\right)^n = 1 \tag{3.3}$$

for all n. We rewrite this result thanks to the multinomial theorem:

$$\sum_{\{l_1,\ldots,l_K\}} \frac{n!}{l_1!\cdots l_K!} w_1^{l_1}\cdots w_K^{l_K} = 1. \tag{3.4}$$

The sum indicates that we must take into account all sequences of non-negative integers $\{l_1,\ldots,l_K\}$ such that $\sum_{i=1}^{K} l_i = n$.

In order to compute $\mathbf{C}$, we must determine the mode weights $\{w_i\}$ and apply Eq.(3.4)

[1]This may seem a hazardous assumption. As we shall see shortly, it isn't the case. For the time being, we point out that losses affect the statistical properties of most but not all quantum states of interest: coherent states are one such exception.

for a given range of values for n [66]. The reconstruction of the experimental conditional probability matrices associated with our time-multiplexed detectors is discussed in Appendix 4.3.

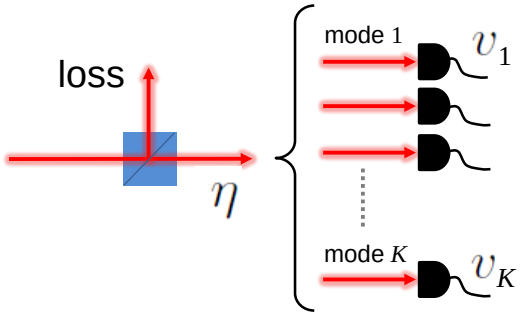

Figure 3.3 It is possible to model a multiplexed detector affected by loss as an array of K photon counters preceded by a beam splitter with reflectivity $(1-\eta)$. The parameter η represents the efficiency of detection of the considered mode multiplexer.

Let us turn to the effect of loss. As noted in [65], one way to address this aspect relies on the design of the considered mode multiplexer to identify specific sources of loss in the detector. While this is an entirely valid approach, a more general description which can apply to any PNRD based on mode multiplexing is desirable. To this end, we picture the detector as a device that splits an incoming signal into K detection modes (see Fig. 3.3). Loss is assumed to take place prior to detection: this operation is modelled by a beam splitter with transmissivity $|t|^2 = \eta$. If we assume the (lossless) detection modes to be orthogonal (that is, distinguishable) and to be each described by the probability v_i of containing one photon, we have that $\sum_{i=1}^{K} v_i = \eta$.

If n particles impinge on the BS with probability $\widetilde{f}_n$ and n' photons survive the

losses with probability $\widetilde{p}_{n'}$, we can write that

$$\widetilde{p}_{n'} = \sum_n \widetilde{P}(n'|n)\widetilde{f}_n \,, \tag{3.5}$$

where $\widetilde{P}(n'|n)$ is again a conditional probability. For each incoming particle, loss occurs with the same probability $(1-\eta)$ hence

$$\widetilde{P}(n'|n) = \binom{n}{n'} \eta^{n'} (1-\eta)^{n-n'} \,, \tag{3.6}$$

i.e. the detection process follows a binomial distribution. We remark that the above relation is not valid for $n' > n$ (physically, this would mean that more photons are present *after* loss); in fact, $\widetilde{P}(n'|n) = 0$ whenever $n < n'$. We can identify $\{\widetilde{P}(n'|n)\}$ as the elements of a loss matrix $\mathbf{L}(\eta)$, where we explicitly indicate its dependence on the efficiency of detection η. The parameter η (or, equivalently, the quantities $\{v_i\}$) can be experimentally determined, as explained in Chapter 4.

In the light of these results, mode multiplexing and loss are treated as independent effects. In other words, we can think of applying the conditional probability matrix to a photon distribution that has previously undergone loss. Therefore, the relation between counting statistics (given by the vector $\mathbf{p}$) and photon statistics (described by $\mathbf{f}$) for a lossy mode multiplexer reads [65]

$$\mathbf{p} = \mathbf{C} \cdot \mathbf{L}(\eta) \cdot \mathbf{f} \,. \tag{3.7}$$

This important result can be readily adapted to the scheme that interests us in this thesis, namely that of a two-mode weak-field homodyne detection layout (see Fig. 3.4). Eq.(3.7) applies to the individual outputs from each detector; what do we obtain if we look at coincidence events? The detection output is now a matrix of

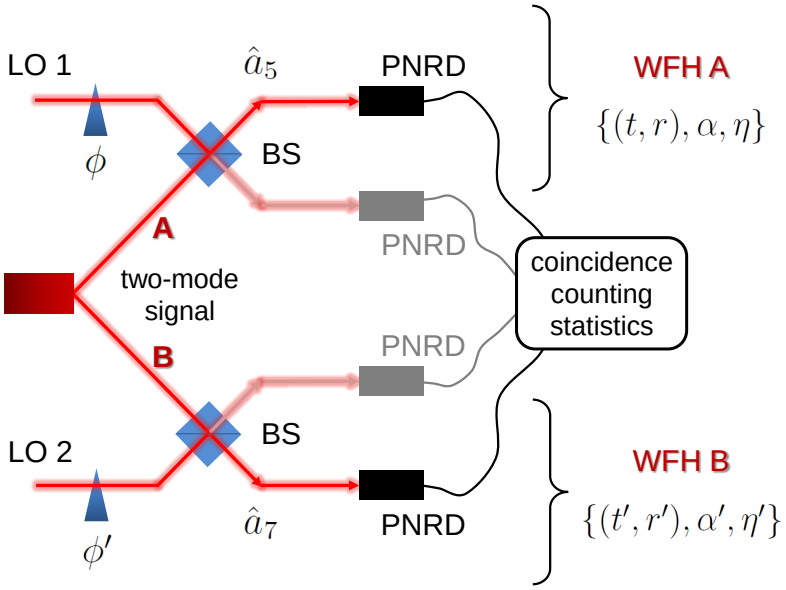

Figure 3.4 To study two-mode quantum states, we rely on weak-field homodyne detectors to probe each mode of the input state. For this purpose, mode A and mode B are interfered with LO 1 and LO 2, respectively; subsequently, we can choose to detect one or both modes out of the interference beam splitters. Each WFH detector is characterised by a set of parameters: the transmission and reflection coefficients (t, r) of the BS, the intensity of the weak coherent state $|\alpha|^2$, the LO phase ϕ – which we can set to arbitrary values – and the detection efficiency η. In our scheme, it is possible to tune $|\alpha|$, $|\alpha'|$, ϕ and ϕ' individually. The PNRDs provide us with a set of coincident click events conveniently visualised as a joint counting statistics matrix.

joint counting statistics $\{P_{jk}\}$, where rows and columns correspond to the available bins in each photon-number-resolving detector. The probability of counting j light quanta in one mode and k in the other is related to the probability of having n, m incoming photons in each mode, respectively. The distribution of photons is given

by a matrix $\mathbf{F}$ with elements $\{F_{nm}\}$. Extending Eq.(3.7) to two dimensions yields

$$P_{jk} = \sum_{n,m} \sum_{q,r} C_{jq} L_{qn}(\eta_{\mathrm{A}}) F_{nm} L_{mr}(\eta_{\mathrm{B}}) C_{rk} \,, \tag{3.8}$$

where indices j, k refer to numbers of photons detected, q, r to particles which survived loss, and n, m indicate the number of photons initially present in each mode. It is helpful to remember that C_{kn} corresponds to the probability of detecting k particles conditional on the generation of n photons, while $L_{n'n}$ is associated to the transmission of n' particles through the beam splitter in Fig. 3.3 out of n initial photons produced. Eq.(3.8) links the matrix elements of $\mathbf{F}$ to the counting statistics $\{P_{jk}\}$. We can recast this result in a more compact form:

$$\mathbf{P} = \mathbf{C}_{\mathrm{A}} \cdot \mathbf{L}(\eta_{\mathrm{A}}) \cdot \mathbf{F} \cdot \mathbf{L}(\eta_{\mathrm{B}})^{\mathrm{T}} \cdot \mathbf{C}_{\mathrm{B}}^{\mathrm{T}} \,. \tag{3.9}$$

All upper case bold letters indicate matrices; $\mathbf{M}^{\mathrm{T}}$ stands for the transpose of $\mathbf{M}$.

Eqn.(3.7) and (3.9) are the formulae that we set out to establish at the beginning of this section: they relate the (coincidence) counting statistics to the photon distribution over one or two optical modes. Let us go back to Eq.(3.7) to make an additional remark. The measurements performed in an experiment give access to the elements of $\mathbf{p}$. Therefore, the most straightforward way to deduce $\mathbf{f}$ from the counting statistics is to invert Eq.(3.7):

$$\mathbf{f} = \mathbf{L}(\eta)^{-1} \cdot \mathbf{C}^{-1} \cdot \mathbf{p} \,. \tag{3.10}$$

This operation is legitimate provided that the inverse matrices $\mathbf{L}(\eta)^{-1}$ and $\mathbf{C}^{-1}$ exist. This in turn means that the conditional probability matrix and the loss matrix have to be non-singular. This assumption may not always hold depending on which of two factors is predominant: a very bright signal or a low efficiency of detection. The lower-right diagonal elements of $\mathbf{C}$ are, for realistic PNRDs, very close to zero (see Appendix 4.3). If most available bins are populated (that is, $k \simeq N$), the inversion of the conditional probability matrix is likely to lead to an unreliable retrieval of $\mathbf{f}$ [65]. If η is small this will impact on the form of $\mathbf{L}(\eta)$, which in turn will negatively affect the reconstruction of the photon statistics. The above inversion can still be performed provided that suitable constraints are introduced (see Chapter 4).

Our next goal is to compute an explicit expression for $\mathbf{F}$ in the case of our WFH detection scheme; we expect the elements of the photon statistics matrix to exhibit a clear phase dependence.

3.2.2 Response of a WFH detector to a generic quantum state

Let us consider the interference of Fock state $|1\rangle$ with coherent state $|\alpha\rangle$ on a beam splitter characterised by real transmission and reflection coefficients t and $r = \sqrt{1-t^2}$, respectively. The BS transformation can be expressed as[2]

$$\begin{pmatrix} \hat{a}_3 \\ \\ \hat{a}_4 \end{pmatrix} = \begin{pmatrix} t & -r \\ \\ r & t \end{pmatrix} \cdot \begin{pmatrix} \hat{a}_1 \\ \\ \hat{a}_2 \end{pmatrix}, \tag{3.11}$$

[2]For the choice of (t, r) and the form of the scattering matrix, we refer to Eqn.(2.2) and (2.3).

which leads to the input-output relations

$$\begin{cases} \hat{a}_1^\dagger = t\hat{a}_3^\dagger + r\hat{a}_4^\dagger \\ \hat{a}_2^\dagger = -r\hat{a}_3^\dagger + t\hat{a}_4^\dagger \end{cases} . \tag{3.12}$$

The state impinging on the beam splitter reads

$$|\psi\rangle_{\text{in}} = |1\rangle_1|\alpha\rangle_2 = \hat{D}_2(\alpha)\hat{a}_1^\dagger|0\rangle_1|0\rangle_2 = e^{\alpha\hat{a}_2^\dagger - \alpha^*\hat{a}_2}\hat{a}_1^\dagger|0\rangle_1|0\rangle_2 \tag{3.13}$$

from the definition of the displacement operator $\hat{D}(\alpha)$ (see Chapter 1, Section 1.1). According to Eq.(3.12), the total state after the beam splitter is

$$|\psi\rangle_{\text{out}} = \hat{D}_3(-r\alpha)\hat{D}_4(t\alpha)(t\hat{a}_3^\dagger + r\hat{a}_4^\dagger)|0\rangle_3|0\rangle_4 \,. \tag{3.14}$$

If we consider a generic Fock state $|n\rangle$, we can generalise the above expressions for the input and output states:

$$\begin{aligned} &|\psi\rangle_{\text{in}} = \hat{D}_2(\alpha)(\hat{a}_1^\dagger)^n|0\rangle_1|0\rangle_2 \,, \\ &|\psi\rangle_{\text{out}} = \sum_{k=0}^{n} \binom{n}{k} t^{n-k} r^k \hat{D}_3(-r\alpha)\hat{D}_4(t\alpha)(\hat{a}_3^\dagger)^{n-k}(\hat{a}_4^\dagger)^k|0\rangle_3|0\rangle_4 \,. \end{aligned} \tag{3.15}$$

We now introduce the useful shorthand notation $|\alpha; n\rangle := \hat{D}(\alpha)(\hat{a}^\dagger)^n|0\rangle$ to indicate a displaced Fock state. $|\alpha; n\rangle$ is not normalised as $|\langle\alpha; n|\alpha; n\rangle|^2 = n!$. However, $\hat{D}(\alpha)$ preserves scalar products hence the displaced Fock states form an orthogonal set, for a given choice of α, with $\langle\alpha; n|\alpha; m\rangle = \sqrt{n!}\,\delta_{nm}$.

We rewrite the total output state $|\psi\rangle_{\rm out}$ as

$$|\psi\rangle_{\rm out} = \sum_{k=0}^{n} \binom{n}{k} t^{n-k} r^k |-r\alpha; n-k\rangle_3 |t\alpha; k\rangle_4. \tag{3.16}$$

Consequently, for any single-mode pure state in mode 1, expressed as $\sum_{n=0}^{+\infty} c_n |n\rangle_1$ in the Fock basis, the two-mode output state reads[3]

$$|\Psi\rangle_{\rm out} = \sum_{k=0}^{+\infty} \sum_{n=k}^{+\infty} \binom{n}{k} c_n \, t^{n-k} r^k |-r\alpha; n-k\rangle_3 |t\alpha; k\rangle_4 \, . \tag{3.17}$$

If both output modes are detected by suitable mode multiplexers, the photon statistics are described by the probability distribution function

$$f(m,m') = \sum_{k=0}^{+\infty} \left| \sum_{n=k}^{+\infty} \binom{n}{k} c_n \, t^{n-k} r^k \langle m| -r\alpha; n-k\rangle_3 \langle m'|t\alpha; k\rangle_4 \right|^2 . \tag{3.18}$$

In the following we shall be mainly interested in detection schemes where one output mode is discarded, i.e. it is not detected. If the unobserved mode is identified by the reflected component of the input state in mode 1, this corresponds to a partial trace operation over mode 4. We then record the statistics of the reduced output state

$$|\Phi\rangle_{\rm out} = \sum_{k=0}^{+\infty} r^k \sqrt{k!} \, |\Phi\rangle_k \, , \tag{3.19}$$

where

$$|\Phi\rangle_k = \sum_{n=k}^{+\infty} \binom{n}{k} c_n \, t^{n-k} |-r\alpha; n-k\rangle_3 \, . \tag{3.20}$$

[3]It is possible to invert the order of the summations over n and k.

Therefore, the probability of detecting m photons in mode 3 is given by

$$f(m) = \sum_{k=0}^{+\infty} r^{2k} k! \left| \sum_{n=k}^{+\infty} \binom{n}{k} c_n \, t^{n-k} \langle m| - r\alpha; n-k\rangle_3 \right|^2 . \tag{3.21}$$

It is possible to express $f(m)$ more explicitly thanks to the following result:

$$\hat{D}(\alpha)(\hat{a}^\dagger)^n|0\rangle = (\hat{a}^\dagger - \alpha^* \hat{I})^n \hat{D}(\alpha)|0\rangle \, . \tag{3.22}$$

To verify its validity, we recall that $\hat{D}^\dagger(\alpha)\hat{a}^\dagger\hat{D}(\alpha) = \hat{a}^\dagger + \alpha^*\hat{I}$. If we multiply both sides of Eq.(3.22) by $\hat{D}^\dagger(\alpha)$ from the left, we have that the right-hand side becomes

$$\begin{aligned} \hat{D}^\dagger(\alpha)(\hat{a}^\dagger - \alpha^*\hat{I})^n \hat{D}(\alpha)|0\rangle &= \hat{D}^\dagger(\alpha) \sum_{k=0}^{n} \binom{n}{k} (\hat{a}^\dagger)^{n-k} (-\alpha^*)^k \hat{D}(\alpha)|0\rangle = \\ &= \sum_{k=0}^{n} \binom{n}{k} (-\alpha^*)^k (\hat{a}^\dagger + \alpha^*)^{n-k}|0\rangle = \\ &= (\hat{a}^\dagger)^n|0\rangle \end{aligned} \tag{3.23}$$

since $\hat{D}^\dagger(\alpha)(\hat{a}^\dagger)^{n-k}\hat{D}(\alpha) = (\hat{a}^\dagger + \alpha^*\hat{I})^{n-k}$. Yet the left-hand side in Eq.(3.22) can be expressed as $\hat{D}^\dagger(\alpha)\hat{D}(\alpha)(\hat{a}^\dagger)^n|0\rangle = (\hat{a}^\dagger)^n|0\rangle$ given that the displacement operator is unitary. The two sides are equal, therefore Eq.(3.22) is verified.

This allows us to rewrite the inner product $\langle m|\alpha; n\rangle$ in Eq.(3.21) as

$$\begin{aligned} \langle m|\alpha; n\rangle &= \langle m| \sum_{\kappa=0}^{n} \binom{n}{\kappa} (\hat{a}^\dagger)^\kappa (-\alpha^*)^{n-\kappa}|\alpha\rangle = \\ &= \sum_{\kappa=0}^{n} \binom{n}{\kappa} \frac{\sqrt{m!}}{(m-\kappa)!} (-1)^{n-\kappa} |\alpha|^{m+n-2\kappa} e^{i(m-n)\phi} e^{-|\alpha|^2/2}, \end{aligned} \tag{3.24}$$

where $\alpha = |\alpha|e^{i\phi}$.

The results obtained for a single-mode state can be generalised to the two-mode layout (see Fig. 3.4). If we only look at the two transmitted output modes, the joint photon statistics for a generic state $\sum_{n,n'=0}^{+\infty} c_{n,n'}|n\rangle|n'\rangle$ measured with two WFH detectors identified by settings $\{(t,r),\alpha,\eta\}$ and $\{(t',r'),\alpha',\eta'\}$ can be computed as

$$F(m,m') = \sum_{k=0}^{+\infty}\sum_{k'=0}^{+\infty} k!\,k'!\,r^{2k}(r')^{2k'}\left|\sum_{n=k}^{+\infty}\sum_{n'=k'}^{+\infty} c_{nn'}\binom{n}{k}\binom{n'}{k'}\cdot \right. \\ \left. \cdot\, t^{n-k}(t')^{n'-k'}\langle m|-r\alpha;n-k\rangle_5\langle m'|-r'\alpha';n'-k'\rangle_7\right|^2 . \tag{3.25}$$

The probability amplitudes $\langle m|-r\alpha;n-k\rangle_5$ and $\langle m'|-r'\alpha';n'-k'\rangle_7$ determine the dependence of $F(m,m')$ on the phases ϕ, ϕ' of the local oscillators. As we consider different detection events, characterised by the pairs $\{(m,m')\}$, we effectively construct the photon statistics matrix $\mathbf{F}$. While we do not measure it directly in an experiment, this quantity is related to the matrix of recorded coincidence counting events $\{P(m,m')\}$ in the way prescribed by Eq.(3.9). Therefore, knowledge of the detection efficiencies (for the loss matrices) and of the specific design of the mode multiplexers (to determine each conditional probability matrix $\mathbf{C}$) makes it possible – in principle – to retrieve the distribution of photons for the observed state.

3.3 Photon statistics and representations in phase space

In the previous section we obtained closed expressions for the probability of detecting a given number of photons in one or two modes measured with weak-field homodyne

detectors. The elements of the photon statistics matrix **F** are determined from discrete photon counting with added phase sensitivity: $F(m, m')$ is calculated for a given joint detection event (m, m'), and it depends on the LO phase settings through the probability amplitudes in Eq.(3.25). In this sense, this result expresses the combination of particle-like and wave-like aspects that we mentioned earlier in this chapter as we introduced WFH detection.

In this section we shall see that the discrete photon statistics allow us to gain insights into phase space quasi-probability distributions for the observed state. The converse is also true: if the description of a given signal in quantum phase space is known, it is possible – in principle – to reconstruct its photon distribution **F**.

3.3.1 Laying out the theoretical framework

From the particle-like standpoint to the wave-like description

In Chapter 1 we defined the quadratures of the quantised electromagnetic field and introduced the concept of quasi-probability distributions such as the Wigner function $W(x, p)$ (or, in polar coordinates, $W(\alpha)$) for single-mode quantum states. In two seminal papers on foundational aspects of the quantum-mechanical formalism for (density) operators, Cahill and Glauber note that three orderings are most useful in the description of quantum-optical experiments – normal, symmetric and anti-normal [67]. They then introduce a convention that associates to every complex number s, also known as the order parameter, a unique arrangement of products of annihilation and creation operators. In this way, the three main forms of ordering are

characterised by $s = 1$, $s = 0$ and $s = -1$, respectively. This theoretical framework leads to the definition of an s-ordered displacement operator, $\hat{D}(\xi; s) := \hat{D}(\xi)e^{s|\xi|^2/2}$ for $s \in \mathbb{C}$, and of its complex Fourier transform $\hat{T}(\alpha; s)$:

$$\hat{T}(\alpha; s) := \frac{1}{\pi} \int e^{\alpha\xi^* - \alpha^*\xi} \hat{D}(\xi; s) d^2\xi \,. \tag{3.26}$$

Notably, $\hat{T}(\alpha; s)$ is Hermitian if $s \in \mathbb{R}$. From the properties of the displacement operator, it is possible to show that

$$\hat{T}(\alpha; s) = \hat{D}(\alpha)\hat{T}(0; s)\hat{D}^{-1}(\alpha) \,, \tag{3.27}$$

where the dependence of $\hat{T}(0; s)$ on s is found to be

$$\hat{T}(0; s) = \frac{2}{\pi(1-s)} \left(\frac{s+1}{s-1} \right)^{\hat{n}} . \tag{3.28}$$

We recall that $\hat{n} = \hat{a}^\dagger \hat{a}$ is the single-mode photon-number operator. Substituting Eq.(3.28) into Eq.(3.27) we obtain

$$\hat{T}(\alpha; s) = \frac{2}{\pi(1-s)} \hat{D}(\alpha) \left(\frac{s+1}{s-1} \right)^{\hat{n}} \hat{D}^\dagger(\alpha) \,. \tag{3.29}$$

It thus follows that $\hat{T}(\alpha; 0) = (2/\pi)\hat{D}(\alpha)\hat{\Pi}_1\hat{D}^\dagger(\alpha)$, where $\hat{\Pi}_1$ is the parity operator for a single-mode field:

$$\hat{\Pi}_1 := (-1)^{\hat{n}} = \sum_{n=0}^{+\infty} (-1)^n |n\rangle\langle n| \,. \tag{3.30}$$

From the results presented above, it is possible to introduce an s-parametrised quasi-probability distribution $\mathcal{W}(\alpha; s)$ for quantum states in phase space [68]. Particularly, we recover the Wigner function as $W(\alpha) = \mathcal{W}(\alpha; 0)$. The distribution $\mathcal{W}(\alpha; s)$ is closely related to the operator $\hat{T}(\alpha; s)$: indeed, Cahill and Glauber show that $\mathcal{W}(\alpha; s) = \langle \hat{T}(\alpha; s) \rangle$, where the expectation value is taken over the considered quantum state. It then follows that the Wigner function for a single-mode field described by the density operator $\hat{\rho}$ can be computed as

$$
\begin{aligned}
W(\alpha) &= \langle \hat{T}(\alpha; 0) \rangle = && (3.31)\\
&= \mathrm{Tr}[\hat{\rho}\, \hat{T}(\alpha; 0)] = && (3.32)\\
&= \frac{2}{\pi} \mathrm{Tr}[\hat{\rho} \hat{D}(\alpha) \hat{\Pi}_1 \hat{D}^\dagger(\alpha)] = && (3.33)\\
&= \frac{2}{\pi} \mathrm{Tr}[\hat{D}(-\alpha) \hat{\rho} \hat{D}^\dagger(-\alpha) \hat{\Pi}_1] = && (3.34)\\
&= \frac{2}{\pi} \sum_{n=0}^{+\infty} (-1)^n \langle n | \hat{D}(-\alpha) \hat{\rho} \hat{D}^\dagger(-\alpha) | n \rangle \,. && (3.35)
\end{aligned}
$$

From Eq.(3.33) to Eq.(3.34) we used the cyclic property of the trace operation, $\mathrm{Tr}[\hat{A}\hat{B}\hat{C}\hat{D}] = \mathrm{Tr}[\hat{B}\hat{C}\hat{D}\hat{A}] = \mathrm{Tr}[\hat{C}\hat{D}\hat{A}\hat{B}] = \mathrm{Tr}[\hat{D}\hat{A}\hat{B}\hat{C}]$, together with $\hat{D}^\dagger(\alpha) = \hat{D}(-\alpha)$. Eq.(3.35) follows by expressing the trace operation in the basis of Fock states and recalling the definition of $\hat{\Pi}_1$ given in Eq.(3.30).

These equalities draw an explicit connection between the Wigner function and the parity operator [69]. We can compute the value of $W(\alpha)$ for the state $\hat{\rho}$ at point $\alpha = (|\alpha|, \phi)$ in phase space as the expectation value of the displaced parity operator (see Eq.(3.33)), or equivalently – moving from the Heisenberg to the Schrödinger representation – as the expectation value of $\hat{\Pi}_1$ calculated on the displaced state

$\hat{\rho}_\alpha := \hat{D}(-\alpha)\hat{\rho}\hat{D}^\dagger(-\alpha)$. In Eq.(3.35), we recognise the n-th diagonal element of the displaced state $\hat{\rho}_\alpha$ as the probability of detecting n particles in a photon counting experiment, i.e. $\langle n|\hat{\rho}_\alpha|n\rangle \equiv f_n[\hat{\rho}_\alpha]$. Operationally, this means that we can apply different displacements to the initial state $\hat{\rho}$ to reconstruct $W(\alpha)$; for every probed point in phase space, the photon statistics given by the matrix with elements $\{f_n[\hat{\rho}_\alpha]\}$ provide access to the Wigner function in the considered phase space region.

How do we realise the displacement operation in practice? Two similar albeit independent answers were published in short succession by Wallentowitz and Vogel and by Banaszek and Wódkiewicz [23, 27]. In the absence of any displacement, the Wigner function at the origin of phase space reads (see Eq.(3.35) for $\alpha = 0$)

$$W(0) = \frac{2}{\pi}\sum_{n=0}^{+\infty}(-1)^n\langle n|\hat{\rho}|n\rangle = \frac{2}{\pi}\sum_{n=0}^{+\infty}(-1)^n f_n[\hat{\rho}]\,. \tag{3.36}$$

Let us now extend this result by considering the interference of the signal $\hat{\rho}$ with another single-mode field (referred to as the probe) at a beam splitter with transmittivity T [23, 27]. If the probe is in a coherent state $|\alpha\rangle$, and for a suitable choice of the parameters T and $|\alpha|$, a displaced signal state is produced as the result of the interaction [70]. In this case, measuring the transmitted output mode with a photodetector yields [27]

$$W_{\rm out}(0) = \langle\hat{T}_{\rm out}(0;0)\rangle = \frac{1}{T}\mathcal{W}_{\rm signal}\left(\sqrt{\frac{1-T}{T}}\,\alpha; -\frac{1-T}{T}\right). \tag{3.37}$$

Equivalently,

$$\mathcal{W}_{\rm signal}\left(\sqrt{\frac{1-T}{T}}\,\alpha;-\frac{1-T}{T}\right)=T\cdot\frac{2}{\pi}\sum_{n=0}^{+\infty}(-1)^n f_n[\hat{\rho}_{\rm out}]\,. \tag{3.38}$$

The distribution of photons associated with the output state that we measure allows us to compute $W_{\rm out}(0)$; in turn, $W_{\rm out}(0)$ is equal – up to a proportionality factor – to the s-parametrised quasi-probability distribution $\mathcal{W}_{\rm signal}(\alpha';s)$ for the original input state, with $\alpha'=\sqrt{(1-T)/T}\,\alpha$ and $s=1-(1/T)$ for the order parameter [27]. Therefore, as we move around in phase space by varying the intensity and phase of the coherent-state probe we reconstruct $\mathcal{W}_{\rm signal}(\alpha';s)$: this distribution approaches the Wigner function of the signal provided that T is sufficiently close to one. We remark that the condition $T\gg R$ limits the accessible values for α' unless α has a wide dynamic range. We see that Eq.(3.38) links the Wigner function of a quantum state to the photon statistics $\{f_n[\hat{\rho}_{\rm out}]\}$ retrieved at the output of an interferometric scheme where the initial quantum state interacts with a coherent field.

The framework that we have just presented suffers from a few restrictions: it only applies to single-mode fields, and it assumes ideal detection as well as perfect mode matching between signal and probe.

Let us start by extending the above results to the multi-mode case. The parity operator for K optical modes can be written as the tensor product of single-mode parity operators:

$$\hat{\Pi}_K=\bigotimes_{k=1}^{K}(-1)^{\hat{n}_k}=(-1)^{\sum_{k=1}^{K}\hat{n}_k}=\sum_{n_k}\left[\bigotimes_{k=1}^{K}(-1)^{n_k}\,|n_k\rangle\langle n_k|\right], \tag{3.39}$$

where $\hat{\Pi}_{n_k} = |n_k\rangle\langle n_k|$ is the projector on single-mode number state $|n_k\rangle$. In the Fock basis, $\hat{\Pi}_{n_k}$ is represented by a diagonal matrix.

Eq.(3.39) leads to the expression for the Wigner function associated to a signal $\hat{\rho}$:

$$W(\{\alpha_k\}) = \left(\frac{2}{\pi}\right)^K \mathrm{Tr}[\hat{D}(\{-\alpha_k\})\hat{\rho}\hat{D}^\dagger(\{-\alpha_k\})\hat{\Pi}_K]\,, \tag{3.40}$$

where $\{\alpha_k\} = \{\alpha_1, \ldots, \alpha_K\}$. At the origin of the K-dimensional phase space, this expression simplifies to

$$W(\mathbf{0}) = \left(\frac{2}{\pi}\right)^K \mathrm{Tr}[\hat{\rho}\,\hat{\Pi}_K]\,. \tag{3.41}$$

In the following we will focus our attention on two-mode quantum states: from here on, we shall thus restrict our analysis to this case. For $K = 2$, the Wigner function at a generic point (α_1, α_2) in the four-dimensional phase space reads

$$\begin{aligned} W(\alpha_1, \alpha_2) &= \frac{4}{\pi^2}\sum_{n_1}\sum_{n_2}(-1)^{n_1+n_2}\langle n_1, n_2|\hat{\rho}_{\{\alpha\}}|n_1, n_2\rangle = \\ &= \frac{4}{\pi^2}\sum_{n_1}\sum_{n_2}(-1)^{n_1+n_2}F(n_1, n_2)\,, \end{aligned} \tag{3.42}$$

where $\hat{\rho}_{\{\alpha\}}$ is the density operator for the displaced state and the expression for $F(n_1, n_2)$ is given by Eq.(3.25). We recall the shorthand notation $|n_1, n_2\rangle \equiv |n_1\rangle|n_2\rangle$.

To drop the assumption of ideal detection, we can take into account the specific design of the photon counters as well as loss, as explained in Section 3.2.1 for mode multiplexers. As an additional remark, we note that any detection system will provide counting statistics for the observed state, not its photon statistics. For this reason, the procedure of reconstruction of the Wigner function that we have

just discussed requires the computation of the photon distribution from the click statistics. Finally, we will comment on the hypothesis of perfect mode matching later on and shall regard it as a valid assumption unless otherwise stated.

Retrieving the photon statistics from the Wigner function

We now consider the converse approach: how does the Wigner function of a given quantum state provide access to its photon statistics? For a two-mode state, the Wigner distribution is a function of the quadratures (x_1, p_1, x_2, p_2) or, alternatively, of the complex amplitudes (α_1, α_2). If we extend the single-mode relation between the elements of $\hat{\rho}$ and $W(x,p)$ to the two-mode case, we find [14, 35]

$$\langle x_1, x_2|\hat{\rho}|y_1, y_2\rangle = \int_{-\infty}^{+\infty}\int_{-\infty}^{+\infty} e^{\imath(x_1-y_1)p_1} e^{\imath(x_2-y_2)p_2}\, W\Big(\frac{x_1+y_1}{2}, p_1, \frac{x_2+y_2}{2}, p_2\Big)\, dp_1 dp_2\,, \tag{3.43}$$

along with the reciprocal expression

$$\begin{aligned} W(x_1,p_1,x_2,p_2) = \frac{1}{(2\pi)^2}\int_{-\infty}^{+\infty}\int_{-\infty}^{+\infty} e^{\imath\nu_1 p_1 + \imath\nu_2 p_2}\cdot \\ \cdot \langle x_1 - \frac{\nu_1}{2}, x_2 - \frac{\nu_2}{2}|\,\hat{\rho}\,|x_1 + \frac{\nu_1}{2}, x_2 + \frac{\nu_2}{2}\rangle\, d\nu_1 d\nu_2\,. \end{aligned} \tag{3.44}$$

The latter formula is a generalisation of the definition for $W(x,p)$ in the single-mode case (see Eq.(1.31)). These expressions reaffirm that the discrete- and continuous-variable formalisms are not distinct descriptions of quantum-optical phenomena. Rather, the choice of one framework over the other is a matter of convenience determined by the specific aspect(s) under consideration. Eq.(3.43) is a useful starting point, yet we would rather leave the quadrature representation for the Fock basis.

If $\phi_n(x)$ is the wave function of number state $|n\rangle$, we can write that

$$\begin{aligned}\langle m_1, m_2|\hat{\rho}|n_1, n_2\rangle = &\int_{-\infty}^{+\infty}\int_{-\infty}^{+\infty}\int_{-\infty}^{+\infty}\int_{-\infty}^{+\infty}\langle x_1, x_2|\hat{\rho}|y_1, y_2\rangle\ \phi^*_{m_1}(x_1)\phi_{n_1}(y_1)\cdot \\ &\cdot \phi^*_{m_2}(x_2)\phi_{n_2}(y_2)\, dx_1 dy_1 dx_2 dy_2\,.\end{aligned} \tag{3.45}$$

for the elements of $\hat{\rho}$ in the photon-number basis. The wave function $\phi_n(x)$ is expressed as

$$\phi_n(x) = \frac{1}{\pi^{1/4}\sqrt{n!2^n}} H_n(x) e^{-x^2/2}\,, \tag{3.46}$$

where $H_n(x)$ is the n-th Hermite polynomial (and we set $\hbar = 1$).

Substituting Eq.(3.46) into Eq.(3.45) yields

$$\begin{aligned}\langle m_1, m_2|\hat{\rho}|n_1, n_2\rangle = &C(n_1, m_1, n_2, m_2)\cdot\left[\frac{\partial^{n_1}}{\partial t_1^{n_1}}\frac{\partial^{m_1}}{\partial z_1^{m_1}}\frac{\partial^{n_2}}{\partial t_2^{n_2}}\frac{\partial^{m_2}}{\partial z_2^{m_2}}\left(e^{-(t_1^2+z_1^2+t_2^2+z_2^2)}\,.\right.\right. \\ &\cdot\int\int\int\int\int\int e^{-\frac{y_1^2}{4}-\imath y_1 p_1}e^{-\frac{y_2^2}{4}-\imath y_2 p_2}e^{-(x_1^2+x_2^2)}\,. \\ &\cdot e^{2x_1(t_1+z_1)}e^{-y_1(t_1-z_1)}e^{2x_2(t_2+z_2)}e^{-y_2(t_2-z_2)}. \\ &\left.\left.\cdot W(x_1, p_1, x_2, p_2)\, dy_1 dx_1 dp_1 dy_2 dx_2 dp_2\right)\right]_{t_1=z_1=t_2=z_2=0}\end{aligned} \tag{3.47}$$

where $C(n_1, m_1, n_2, m_2) := 1/\left(\pi\sqrt{n_1!m_1!n_2!m_2!\,2^{n_1+m_1+n_2+m_2}}\right)$ and we omitted the extrema of integration for ease of read.

Eq.(3.47) provides all elements of $\hat{\rho}$ for a two-mode state in the Fock basis. Depending on the detection system, we may not be able to reconstruct the whole density matrix. Photon-number-resolving detectors, for instance, lack a phase reference and

for this reason do not provide access to off-diagonal terms[4]. Although this is a limitation of the considered detection system, we can still access relevant information about the observed quantum state. Indeed, for $m_1 = n_1$ and $m_2 = n_2$ we find (see the overlap formula given by Eq.(1.32))

$$F(n_1, n_2) = \langle n_1, n_2|\hat{\rho}|n_1, n_2\rangle = \mathrm{Tr}[\hat{\rho}\hat{N}_{12}] = \\ = (2\pi)^2 \iiiint W(x_1, p_1, x_2, p_2) W_{n_1}(x_1, p_1)\, W_{n_2}(x_2, p_2)\, dx_1 dp_1 dx_2 dp_2\,, \tag{3.48}$$

where $W(x_1, p_1, x_2, p_2)$ is the Wigner function of the studied state, $W_{n_1}(x_1, p_1)$ and $W_{n_2}(x_2, p_2)$ are associated with Fock states $|n_1\rangle$ and $|n_2\rangle$ (see Eq.(1.39)), and we have that $\hat{N}_{12} = \hat{n}_1 \otimes \hat{n}_2$. We will make use of Eq.(3.48) in the following section.

3.3.2 Designing an experiment

The WFH layout proposed in [23, 27] was successfully applied to the experimental study of single-mode fields such as coherent and phase-diffused coherent states [72], as well as single-photon fields generated by heralded downconversion in a waveguide [28]. As a first test of our two-mode weak-field homodyne setup, we extended the scheme introduced in [23, 27] to study the capabilities of our system in the direct reconstruction of a two-mode squeezed vacuum state. This allows us to investigate the quantum correlations predicted for this state in the phase-space representation

[4]The action of a PNRD is described by its positive operator-valued measure (POVM) $\hat{M}$. The latter is represented by a diagonal matrix because the detector is not phase-sensitive. The probability of counting n photons can be calculated as $p_n = \mathrm{Tr}[\hat{\rho}\hat{M}_n]$; therefore, the structure of $\hat{M}_n$ precludes any access to the coherences in the density matrix [71].

and assess how reliably we can access such information with weak-field homodyning.

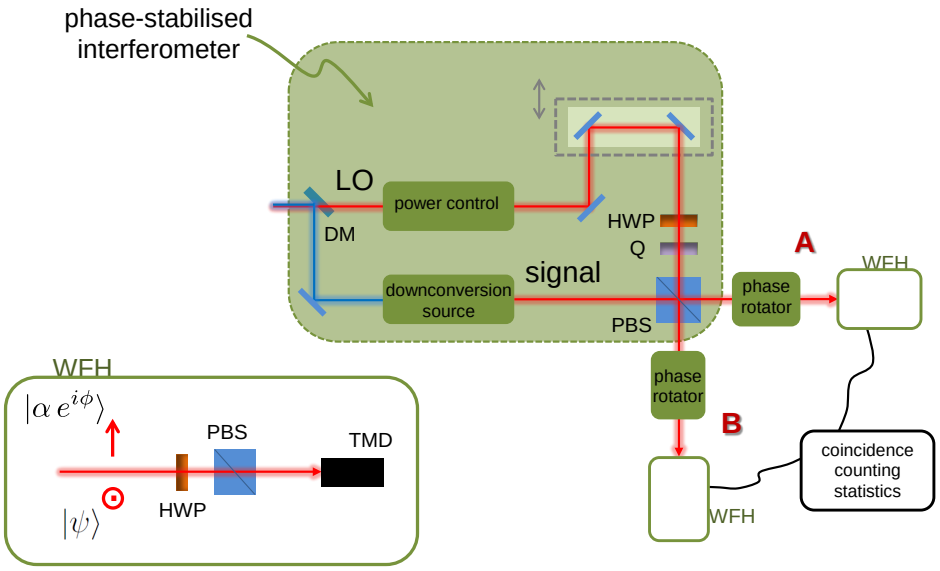

Figure 3.5 This is a simplified sketch of our experimental setup where we indicate the key elements which characterise it. A dichroic mirror (DM) separates the ultraviolet pump beam (in blue) and the infrared beam (in red); the latter becomes our local oscillator. The interaction of the pump beam with a non-linear crystal generates squeezed vacuum states through parametric downconversion. In the LO path, a power control allows us to set the coherent-state intensity, and the half-wave plate (HWP) provides two orthogonally polarised coherent-state probes. The temporal overlap between signal and LO can be optimised thanks to a motorised translation stage and a walk-off compensation element (Q). The downconversion signal and the LOs recombine at a polarising beam splitter (PBS); phase rotators placed in each output mode allow us to change the phase of each local oscillator individually. Interference between one signal mode and the corresponding LO takes place in the WFH detector, comprising a HWP and PBS that erase all polarisation information. Time-multiplexed detectors (TMDs) measure the radiation transmitted out of the interference PBSs; our TMDs can discriminate up to 8 incoming photons. We actively stabilise the phase inside the interferometer (identified by the DM and the recombination PBS) thanks to an ancillary laser system back-propagating through the setup. More details on the experimental setup are found in Chapter 4.

Let us consider the experimental layout shown in Fig. 3.5; we do not include the most technical details as these will be discussed in Chapter 4. We generate a two-mode squeezed vacuum state (TMSS) by parametric downconversion in a bulk

type-II non-linear crystal. Degenerate daughter photons at $\lambda_{\mathrm{IR}} = 830\,\mathrm{nm}$ are produced in orthogonal polarisation modes and in a collinear configuration. As proposed in [23, 27], we probe the squeezed vacuum by interfering each mode with a weak coherent field; subsequently, we measure the output state with two WFH detectors and record the resulting joint counting statistics. With reference to Fig. 3.5, we set the half-wave plates in each WHF detector so that they realise an imbalanced splitting ratio for the interference polarising beam splitters (PBSs) preceding the PNRDs: about 10% of the incident power in each coherent field reaches the detectors. This highly asymmetric configuration[5] guarantees – in principle – that we access the Wigner function of the considered state (see Eq.(3.38)).
Every data acquisition required the optimisation of the downconversion process as well as of the temporal mode overlap between signal and probe. Spectral indistinguishability was achieved by appropriate spectral filtering, while spatial mode overlap was partly guaranteed by coupling both output beams into single-mode fibres just before detection. We postpone a more detailed account of the system preparation prior to a measurement run to the next chapter.

Before we present the outcomes of our experimental investigation, it is useful to make a general observation about the way we probe the quantum phase space to reconstruct the Wigner function of a given state. If we consider the phase-space representation of the vacuum or of a thermal field, we see that these states are insensitive to phase – to reconstruct their Wigner functions it is sufficient to vary $|\alpha|$

[5] One may wonder why we chose a $90:10$ splitting ratio instead of $99:1$, for example. A very imbalanced condition may deteriorate the quality of the probe: indeed, we do not know of beam samplers which guarantee the absence of depolarised background in the transmitted 1% fraction of the LOs.

and take advantage of the central symmetry exhibited by $W(x, p)$ for these fields (see Chapter 1, Section 1.2). By contrast, the study of squeezed light requires phase sensitivity, as also illustrated by its Wigner function. If we are to apply the discussed weak-field homodyne detection scheme to the study of a TMSS, Eq.(3.42) informs us of the dependence of its Wigner distribution on the phases of the local oscillators (through its photon statistics, given by Eq.(3.25)). However, the two-mode squeezed vacuum inherits a phase from the pump beam (see Chapter 2, Section 2.2); consequently, we must be able to vary the LO phases and scan the desired region in phase space while ensuring that the relative phase between signal and coherent fields does not fluctuate significantly before the two beams recombine and become collinear. This motivated the addition of an active phase locking system to our setup; in Chapter 4 we will discuss in more detail the role of active phase stabilisation as well as its implementation.

Preliminary tests on single-mode vacuum and thermal states

To measure the vacuum state, we blocked the radiation coming from the parametric source and directed all light towards one time-multiplexed detector (TMD). The collected data consists then of a set of counting statistics for each considered value $|\alpha|$ of the local oscillator amplitude. To produce a thermal state, we interfered the squeezed vacuum with the LO and subsequently detected one output mode only. This operation is equivalent to performing a partial trace operation on the full two-mode output state[6]. As illustrated in Fig. 3.6 and Fig. 3.7, it is interesting to

[6]This result was mentioned in Chapter 2: if the downconversion modes are spectrally uncorrelated, performing a partial trace over one mode yields a thermal state in the other (see Eq.(2.16)).

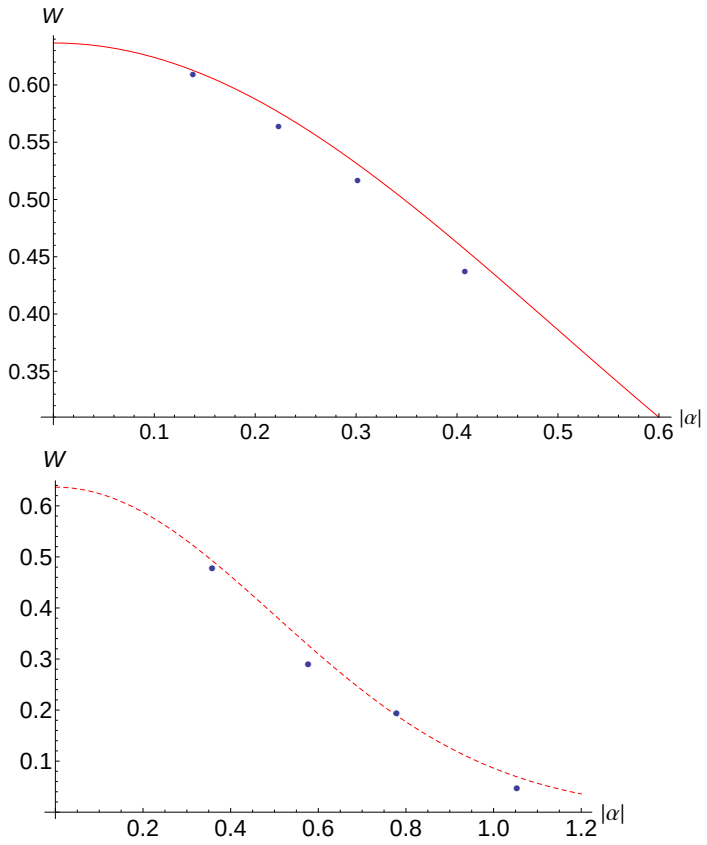

Figure 3.6 We compare the experimental data corresponding to the Wigner function of the vacuum state (blue dots) with two theoretical scenarios. In one case we do not account for loss (top - solid red curve), while in the second scenario we compute the naive inversion of the loss matrices characterising the TMDs (bottom - dashed red curve). In both cases, the data points follow the theoretical curves quite closely.

compare the results of a data analysis which takes into account losses with those where loss is unaccounted for. While we do not observe a significant difference between the two approaches for the vacuum state, the outcome for thermal states is striking. With reference to Fig. 3.7, we see that performing the inversion of the loss matrices naively (that is, without constraints) leads to evident deviations from the predicted behaviour and, most importantly, to unphysical results. Notably, the straightforward inversion of the loss matrices fails most dramatically for higher

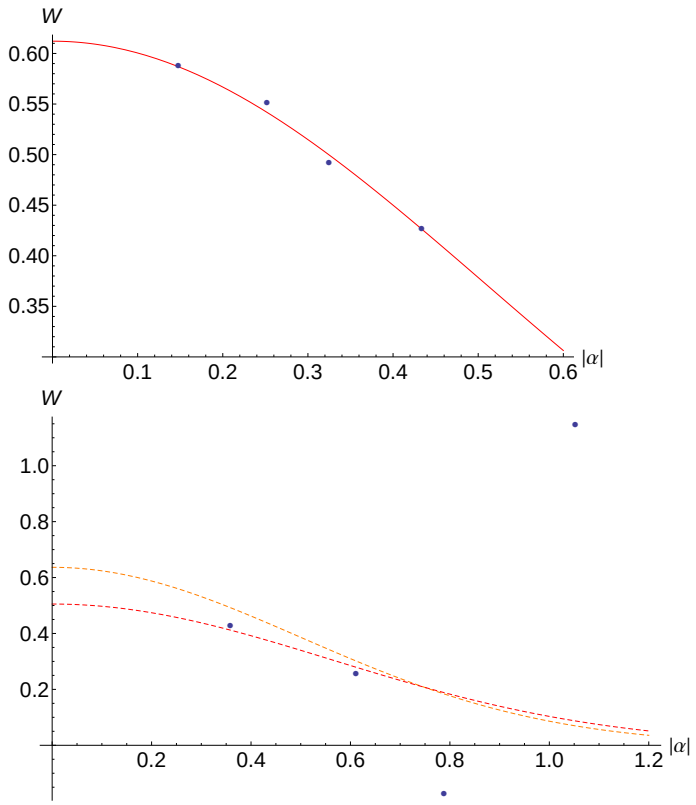

Figure 3.7 We show the experimental Wigner function for a thermal state (blue dots) together with the theoretical behaviour without accounting for loss (top - solid red curve) and the prediction given by naive inversion of the loss matrices (bottom - dashed red curve). We add the Wigner function of the ideal vacuum state (bottom - dashed orange curve) for comparison with the theoretical quasi-probability distribution for a thermal state. While the experimental thermal state after loss is reasonably well described by the corresponding theoretical curve (top plot), the outcome is very different when we invert the detection losses. Notably, one value of the experimental Wigner function is negative, which is clearly unphysical for a thermal state.

values of $|\alpha|$ (in Fig. 3.7, $|\alpha| \simeq 0.8$ and $|\alpha| > 1$). We attribute this behaviour to the structure of $\mathbf{L}(\eta_{\mathrm{A}})$ and $\mathbf{L}(\eta_{\mathrm{B}})$: given the range of our detection efficiencies ($\eta_{\mathrm{A,B}} \in (0.1, 0, 2)$), the lower-right elements of these upper triangular matrices are very close to zero. As observed earlier, this feature can negatively affect the retrieval of the photon statistics from the click counting distribution (see the comment following Eq.(3.10)).

Measurement of the two-mode squeezed vacuum with WFH detectors – optimal parameters for a TMSS in the Wigner function representation

The study of the vacuum state allowed us to verify the photon statistics of our coherent-state probes as well as to test our setup and data acquisition system. We now make use of the full capabilities of our experimental layout to observe a two-mode squeezed vacuum state.

In the Fock basis, we know that a TMSS can be written as

$$|\Psi\rangle_{\mathrm{TMSS}} = \sqrt{1-|\lambda|^2}\sum_{n=0}^{+\infty}\lambda^n|n\rangle_{\mathrm{A}}|n\rangle_{\mathrm{B}}, \tag{3.49}$$

where subscripts A and B identify the modes and λ is the squeezing parameter (see Chapter 2, Section 2.2). This discrete-variable description highlights the photon-number correlations between the two modes, which in our case are conveniently identified by orthogonal polarisations. In the CV framework, the features of the two-mode squeezed vacuum are captured by its Wigner function:

$$W^{\{\sigma,\tau\}}_{\mathrm{TMSS}}(x_{\mathrm{A}},p_{\mathrm{A}},x_{\mathrm{B}},p_{\mathrm{B}}) = \frac{1}{\pi^2\sigma^2\tau^2}e^{-\frac{1}{2\sigma^2}(x_{\mathrm{A}}-x_{\mathrm{B}})^2}e^{-\frac{1}{2\tau^2}(x_{\mathrm{A}}+x_{\mathrm{B}})^2}e^{-\frac{1}{2\sigma^2}(p_{\mathrm{A}}+p_{\mathrm{B}})^2}e^{-\frac{1}{2\tau^2}(p_{\mathrm{A}}-p_{\mathrm{B}})^2}, \tag{3.50}$$

where σ^2 and τ^2 are the variances of the quadrature amplitudes (see Chapter 1, Section 1.2 for the single-mode expression[7]).

[7]The result for a two-mode state is obtained by applying a beam-splitter transformation to the quadratures associated with two single-mode squeezed vacuum states.

If we consider the coordinate transformation

$$\begin{aligned} x &= \langle\alpha|\hat{x}|\alpha\rangle = \sqrt{2}\,|\alpha|\cos\phi \\ p &= \langle\alpha|\hat{p}|\alpha\rangle = \sqrt{2}\,|\alpha|\sin\phi \end{aligned} \tag{3.51}$$

with $|\alpha|^2 = (x^2+p^2)/2$, we obtain

$$\begin{aligned} W_{\mathrm{TMSS}}^{\{\sigma,\tau\}}(|\alpha_{\mathrm{A}}|,\phi_{\mathrm{A}},|\alpha_{\mathrm{B}}|,\phi_{\mathrm{B}}) = \frac{(2/\pi)^2}{\sigma^2\tau^2}\, e^{-\frac{1}{\sigma^2}(|\alpha_{\mathrm{A}}|\cos\phi_{\mathrm{A}}-|\alpha_{\mathrm{B}}|\cos\phi_{\mathrm{B}})^2} e^{-\frac{1}{\tau^2}(|\alpha_{\mathrm{A}}|\cos\phi_{\mathrm{A}}+|\alpha_{\mathrm{B}}|\cos\phi_{\mathrm{B}})^2} \cdot \\ \cdot\, e^{-\frac{1}{\sigma^2}(|\alpha_{\mathrm{A}}|\sin\phi_{\mathrm{A}}+|\alpha_{\mathrm{B}}|\sin\phi_{\mathrm{B}})^2} e^{-\frac{1}{\tau^2}(|\alpha_{\mathrm{A}}|\sin\phi_{\mathrm{A}}-|\alpha_{\mathrm{B}}|\sin\phi_{\mathrm{B}})^2}\,. \end{aligned} \tag{3.52}$$

Eq.(3.51) corresponds to a specific commutation relation for the quadratures, i.e. $[\hat{x},\hat{p}] = \imath$ (see Chapter 1, Section 1.1). The interest of the polar-coordinate representation is that it introduces experimentally determined quantities in the expression for the Wigner function of the TMSS. Indeed, $|\alpha_{\mathrm{A}}|$ and $|\alpha_{\mathrm{B}}|$ are the amplitudes of the coherent states which probe each mode of the squeezed vacuum in our WFH scheme, while ϕ_{A} and ϕ_{B} are the phases of the two local oscillators.

Importantly, we remark that the notation adopted in Eq.(3.50) and Eq.(3.52) avoids the complications brought by the dependence of the quadrature variances σ^2 and τ^2 on the choice of coordinates: in the present section, these quantities are relative to the variance of the vacuum (see Chapter 1, Eqn.(1.40) to (1.42)).

If we define $\phi^+ = \phi_{\mathrm{A}} + \phi_{\mathrm{B}}$ as the sum of the two LO phases, we can simplify the

expression in Eq.(3.52) and make the phase dependence of $W_{\mathrm{TMSS}}^{\{\sigma,\tau\}}$ more explicit:

$$W_{\mathrm{TMSS}}^{\{\sigma,\tau\}}(|\alpha_{\mathrm{A}}|,|\alpha_{\mathrm{B}}|,\phi^{+}) = \left(\frac{2}{\pi}\right)^{2} \frac{1}{\sigma^{2}\tau^{2}} e^{-(|\alpha_{\mathrm{A}}|^{2}+|\alpha_{\mathrm{B}}|^{2})\frac{\sigma^{2}+\tau^{2}}{\sigma^{2}\tau^{2}}} e^{-2|\alpha_{\mathrm{A}}||\alpha_{\mathrm{B}}|\frac{\sigma^{2}-\tau^{2}}{\sigma^{2}\tau^{2}}\cos\phi^{+}}, \quad (3.53)$$

The expressions for $W_{\mathrm{TMSS}}^{\{\sigma,\tau\}}$ that we have just introduced are more general than the ones commonly associated with squeezed vacuum states: we do not assume the amplified variance τ^2 to be the inverse of the squeezed variance σ^2. Therefore, we only constrain these quantities through the inequalities $\sigma^2 \leq 1$ and $\tau^2 \geq 1$.

Experimentally, we interfere the TMSS with the local oscillators and record the coincidence counting statistics with our two weak-field homodyne detectors (see Fig. 3.5) for different values of $|\alpha_{\mathrm{A}}|$, $|\alpha_{\mathrm{B}}|$ and ϕ^{+}; in practice, it is sufficient to vary ϕ_{A} or ϕ_{B}. While the phase locking system ensures that ϕ^{+} does not fluctuate with respect to the phase associated with the TMSS, this only fixes relative quantities. As a consequence, we must add an offset to the argument of the cosine function in Eq.(3.53) to take into account this aspect[8].

The distribution of click counts for the output state is suitably described by a matrix $\mathbf{P}$ of dimension ${n_{\mathrm{A}}}^{\max} \times {n_{\mathrm{B}}}^{\max}$, where in our case ${n_{\mathrm{A}}}^{\max} = {n_{\mathrm{B}}}^{\max} = 9$. What do the counting statistics tell us about the input state? In the light of the results discussed in the previous sections, we first need to reconstruct the distribution of photons $\mathbf{F}$ prior to detection. As highlighted by the study of the vacuum and thermal states, this step in the data analysis is not as straightforward as it may seem: the inversion of Eq.(3.9) can lead to meaningless results in the absence of

[8]For instance, we do not know the value of the LO phase in the output mode where the phase rotator is inactive.

appropriate constraints. To make the post-processing of our experimental data as minimal as possible, we shall only account for the distribution of the incident photons among the available temporal modes through the conditional probability matrices $\mathbf{C}_{\mathrm{A}}$ and $\mathbf{C}_{\mathrm{B}}$. Effectively, this choice amounts to observing the considered state after loss or, equivalently, to measuring a state that underwent loss with unit detection efficiency. As a consequence, all reconstructed information about the TMSS – from the variances σ^2 and τ^2 to its photon statistics – is not corrected for this adverse effect. We can thus make use of the results obtained in the previous sections as long as we are consistent with this assumption.

Let us rewrite Eq.(3.9) as follows:

$$\mathbf{P} = \mathbf{C}_{\mathrm{A}} \cdot \mathbf{F}^{\{\eta_{\mathrm{A}},\eta_{\mathrm{B}}\}} \cdot \mathbf{C}_{\mathrm{B}}^{\mathrm{T}}\,, \quad \text{with} \quad \mathbf{F}^{\{\eta_{\mathrm{A}},\eta_{\mathrm{B}}\}} := \mathbf{L}(\eta_{\mathrm{A}}) \cdot \mathbf{F} \cdot \mathbf{L}(\eta_{\mathrm{B}})^{\mathrm{T}}\,. \tag{3.54}$$

Consequently,

$$\mathbf{F}^{\{\eta_{\mathrm{A}},\eta_{\mathrm{B}}\}} = \mathbf{C}_{\mathrm{A}}^{-1} \cdot \mathbf{P} \cdot (\mathbf{C}_{\mathrm{B}}^{\mathrm{T}})^{-1}\,. \tag{3.55}$$

The photon statistics given by $\mathbf{F}^{\{\eta_{\mathrm{A}},\eta_{\mathrm{B}}\}}$ allow us to sample the Wigner function of the input two-mode squeezed vacuum according to Eq.(3.42):

$$\begin{aligned} W_{\mathrm{exp}}(\alpha_{\mathrm{A}},\alpha_{\mathrm{B}}) &= \frac{4}{\pi^2}\sum_{n_{\mathrm{A}}}\sum_{n_{\mathrm{B}}}(-1)^{n_{\mathrm{A}}+n_{\mathrm{B}}}\langle n_{\mathrm{A}},n_{\mathrm{B}}|\hat{\rho}_{\{\alpha\}}|n_{\mathrm{A}},n_{\mathrm{B}}\rangle = \\ &= \frac{4}{\pi^2}\sum_{n_{\mathrm{A}}}\sum_{n_{\mathrm{B}}}(-1)^{n_{\mathrm{A}}+n_{\mathrm{B}}}F^{\{\eta_{\mathrm{A}},\eta_{\mathrm{B}}\}}(n_{\mathrm{A}},n_{\mathrm{B}})\,. \end{aligned} \tag{3.56}$$

We now consider a discretised version of this expression as we do not vary the phases

of the local oscillators continuously:

$$W_{\mathrm{exp}}^{\{|\alpha_{\mathrm{A}}|,|\alpha_{\mathrm{B}}|\}}(\phi_i^+) = \frac{4}{\pi^2}\sum_{j=0}^{8}\sum_{k=0}^{8}(-1)^{j+k}F_i^{\{\eta_{\mathrm{A}},\eta_{\mathrm{B}}\}}(j,k)\,, \tag{3.57}$$

where the index i identifies the setting of the active phase rotator determining the value of ϕ^+. On the other hand, we can compute $W_{\mathrm{th}}^{\{|\alpha_{\mathrm{A}}|,|\alpha_{\mathrm{B}}|\}}(\phi_i^+)$ from Eq.(3.53) as

$$W_{\mathrm{th}}^{\{|\alpha_{\mathrm{A}}|,|\alpha_{\mathrm{B}}|\}}(\phi_i^+) = \frac{4}{\pi^2\sigma^2\tau^2}e^{-\frac{\sigma^2+\tau^2}{\sigma^2\tau^2}\left[|\alpha_{\mathrm{A}}|_i^2+|\alpha_{\mathrm{B}}|_i^2\right]}e^{-2|\alpha_{\mathrm{A}}|_i|\alpha_{\mathrm{B}}|_i\frac{\sigma^2-\tau^2}{\sigma^2\tau^2}\cos\left(\phi_i^+-\phi_0\right)}\,, \tag{3.58}$$

where ϕ_0 is a phase offset and, once more, the index i identifies the setting of the active phase rotator. The values of the coherent-state amplitudes $|\alpha_{\mathrm{A}}|$ and $|\alpha_{\mathrm{B}}|$ depend on this setting because of an undesired modulation of the intensity of the probe beams induced by non-ideal phase rotators. We postpone a more detailed description of these components to Chapter 4.

To compute $W_{\mathrm{exp}}^{\{|\alpha_{\mathrm{A}}|,|\alpha_{\mathrm{B}}|\}}$ from Eq.(3.57), we first acquire data in the form of $\{P_i(j,k)\}$, i.e. sets of counting statistics; for each considered pair of coherent-state intensities, we vary ϕ^+ within a specified range of phase values. Additionally, for every intensity regime and for each setting of the active phase rotator we measure the counting statistics of the local oscillators only; this allows us to account for the dependence of $|\alpha|$ on ϕ^+, as illustrated by the experimental data in Fig. 3.8. We then apply Eq.(3.55) to reconstruct the photon statistics which appear in Eq.(3.57): this leads to the computation of the experimental (discretised) Wigner function for the TMSS. Every sampled point of the experimental distribution – for a given pair

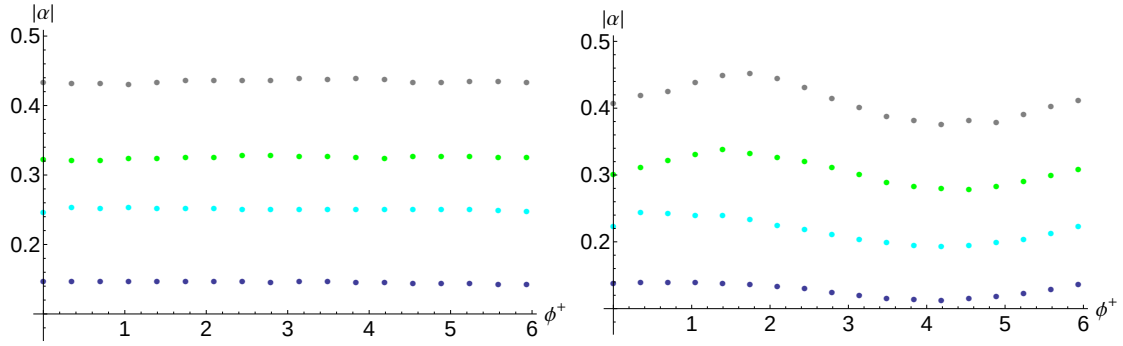

Figure 3.8 In the output mode where the phase rotator is not active (left), we see that the coherent-state amplitude is essentially constant with respect to ϕ^+ as we scan four regimes (blue – $|\alpha| \simeq 0.137$, cyan – $|\alpha| \simeq 0.234$, green – $|\alpha| \simeq 0.316$, gray – $|\alpha| \simeq 0.423$). When we look at the phase dependence of the coherent-state amplitude in the mode where the phase rotator is active (right), we observe an evident modulation of $|\alpha|$ as we vary the phase sum; the effect is more pronounced at higher LO intensity. This undesired modulation may be caused by mechanical imperfections in the active phase rotator (see Chapter 4).

$\big(|\alpha_{\rm A}|, |\alpha_{\rm B}|\big)$ – can then be compared with the corresponding theoretical value derived from Eq.(3.58).

In the light of the procedure that we have just described, we adopt a numerical approach to estimate the variances σ^2 and τ^2 that characterise $W_{\rm th}^{\{|\alpha_{\rm A}|,|\alpha_{\rm B}|\}}$. Let us define the quantity

$$R_1(|\alpha_{\rm A}|, |\alpha_{\rm B}|) := \sum_{i=1}^{M} \left[\ln\left(\frac{W_{\rm exp}(\phi_i^+)}{W_{\rm th}(\phi_i^+)} \right) \right]^2 , \tag{3.59}$$

where M is the number of considered phase settings. We make use of the software Mathematica to run a numerical optimisation on the parameters $(\sigma^2, \tau^2, \phi_0)$ in R_1. Specifically, we call the function NMinimize which outputs values of σ^2, τ^2 and ϕ_0 such that the sum given by the quantities $R_1(|\alpha_{\rm A}|, |\alpha_{\rm B}|)$ for all considered LO intensity regimes is minimised under the assumption $\{\sigma > 0\} \cup \{\tau > 0\}$. The Wigner

$P_{\mathrm{UV}} = 12\,\mathrm{mW}$		$P_{\mathrm{UV}} = 30\,\mathrm{mW}$	
$\eta_{\mathrm{A}} = 0.152$		$\eta_{\mathrm{A}} = 0.139$	
$\eta_{\mathrm{B}} = 0.167$		$\eta_{\mathrm{B}} = 0.187$	
σ^2	0.964	σ^2	1.236
τ^2	1.121	τ^2	0.959
res	$2.8 \cdot 10^{-3}$	res	$6.3 \cdot 10^{-5}$
Individual optimisations			
σ^2_{I}	0.957	σ^2_{II}	1.101
τ^2_{I}	1.129	τ^2_{II}	0.985
$\mathrm{res}_{\mathrm{I}}$	$3.5 \cdot 10^{-5}$	$\mathrm{res}_{\mathrm{II}}$	$3.7 \cdot 10^{-4}$
σ^2_{III}	1.124	σ^2_{IV}	1.122
τ^2_{III}	0.958	τ^2_{IV}	0.964
$\mathrm{res}_{\mathrm{III}}$	$5.7 \cdot 10^{-4}$	$\mathrm{res}_{\mathrm{IV}}$	$1.3 \cdot 10^{-3}$

Table 3.1 Given two datasets (corresponding to different power settings P_{UV} for the ultraviolet pump beam), we perform a numerical minimisation based on the quantity $R_1(|\alpha_{\mathrm{A}}|, |\alpha_{\mathrm{B}}|)$ (see Eq.(3.59)) and find optimal values for σ^2 and τ^2. The function NMinimize provides these estimates along with the residual of the minimisation, which we indicate here as 'res'. The detection efficiencies are experimentally determined (see Chapter 4). For completeness, we also list the individual values $(\sigma^2, \tau^2)_{\{\mathrm{I,II,III,IV}\}}$ obtained by applying NMinimize to each function $R_1(|\alpha_{\mathrm{A}}|, |\alpha_{\mathrm{B}}|)$ rather than to the sum over all intensity regimes. The individual predicted values for the variances of the TMSS do not differ greatly from σ^2 and τ^2, and the residuals of the individual optimisations are not significantly higher.

function describes the input state over the whole phase space, hence one pair of values for the two variances should be sufficient to determine W_{th}. On the other hand, the offset phase ϕ_0 can vary from one data acquisition to the next[9]: for this reason, each term in the sum is characterised by an offset parameter $\phi_0(|\alpha_{\mathrm{A}}|, |\alpha_{\mathrm{B}}|)$. It is interesting to compare the optimal values found with this approach to the results given by a different strategy, where we apply NMinimize to each function $R_1(|\alpha_{\mathrm{A}}|, |\alpha_{\mathrm{B}}|)$ individually, i.e. every intensity regime is treated separately. Particularly, the residuals of these least squares fits might identify datasets with more or less pronounced

[9]We had to restart the active phase locking system each time that one beam was blocked – for example, as we detected light coming from the local oscillators only. The locking system was then reactivated, but the value of the phase that we locked to would change at every such reset.

deviations from the expected behaviour. We summarise the outcome of the numerical optimisations run on two datasets in Table 3.1; we omit the values of the phase offsets for ease of read. The optimal values of σ^2 and τ^2 allow us to compare the experimental data points with W_{th}, as shown in Fig. 3.9 and Fig. 3.10. The graphs obtained with the individual values $(\sigma^2, \tau^2)_{\{\mathrm{I,II,III,IV}\}}$ do not reveal any additional feature, for which reason we did not include them here. The orange points which

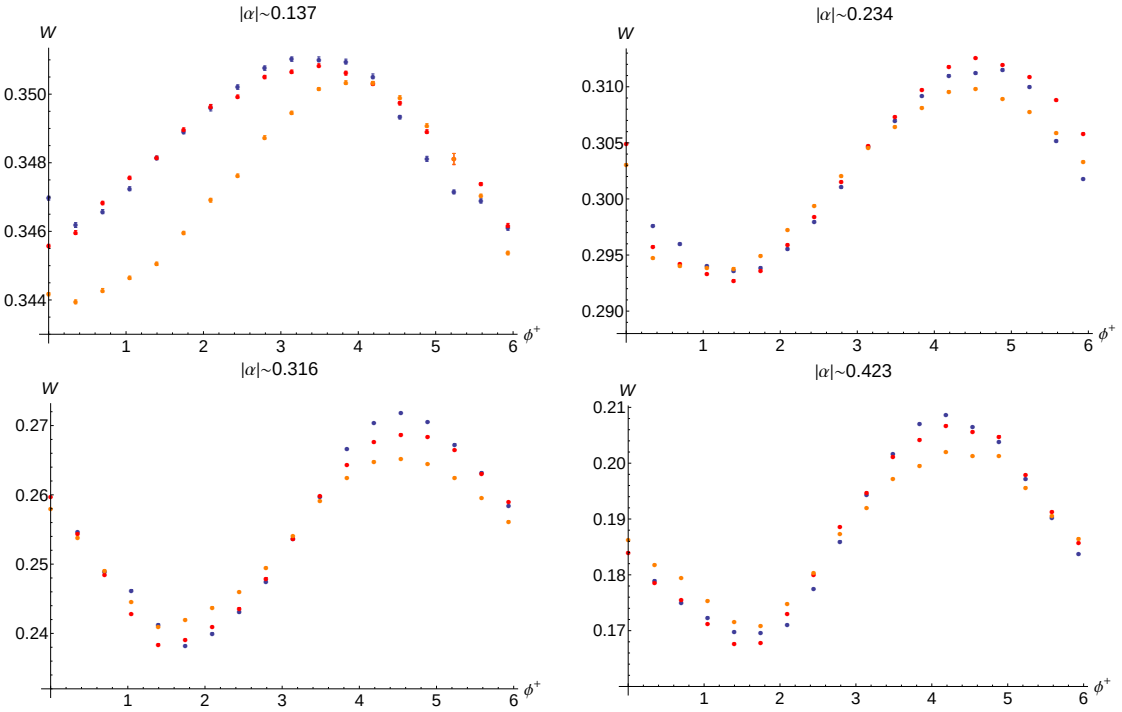

Figure 3.9 For $P_{\mathrm{UV}} = 12\,\mathrm{mW}$, we show our sampling of the Wigner function for the squeezed vacuum and compare the experimental data points (blue dots) with two scenarios: the first one corresponds to a model which predicts $\sigma^2 < 1$ or $\tau^2 < 1$ for the Wigner function of the input state (red dots), whereas the second one excludes this possibility (orange dots). The theoretical graphs 'with squeezing' refer to the values of σ^2 and τ^2 quoted in Table 3.1. Error bars, determined by a Monte Carlo routine, are within the data points. We observe that the agreement varies depending on the considered value of $|\alpha|$ (the indicated values are estimated as an average over all phase settings and over both output modes), although in no case it delivers an incontrovertible answer as to the successful estimation of squeezing with WFH detection on a TMSS.

appear in all plots correspond to a different assumption in the numerical optimisation: in this case we find the minimum of the sum given by the terms $R_1(|\alpha_A|, |\alpha_B|)$ for all intensity regimes under the hypothesis $\{\sigma \geq 1\} \cup \{\tau \geq 1\}$. We thus compare the experimental data with two distinct scenarios: the first one involves a theoretical model which predicts a squeezed variance for the Wigner function describing the input state (red points), whereas the second one excludes this possibility. In this sense, if our experimental blue curves are better described by the former model then we can claim that we are able to observe squeezing in the initial quantum state with our weak-field homodyne detection setup.

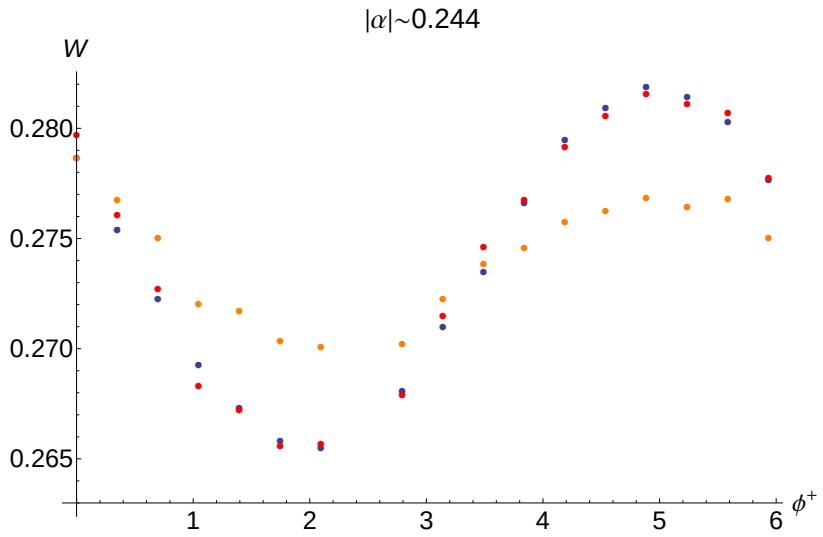

Figure 3.10 For $P_{UV} = 30\,\text{mW}$, we sample the Wigner function for a TMSS and compare the experimental data (blue dots) with the same scenarios considered in Fig. 3.9. The theoretical plot 'with squeezing' refers to the values of σ^2 and τ^2 given in Table 3.1. The quoted value of $|\alpha|$ is estimated as an average over all phase settings and over both output modes. Error bars, determined by a Monte Carlo routine, are within the data points. In this case there seems to be good agreement between the experimental data and the theoretical graph which predicts one squeezed variance; however, this result would have to be confirmed for different LO intensities in order to deliver conclusive evidence of success.

Before we comment on these results, let us discuss an alternative approach to the estimation of the variances which characterise the theoretical Wigner function of our two-mode squeezed state. With reference to Eq.(3.48), we identify $W(x_1, p_1, x_2, p_2)$ with $W^{\{\sigma,\tau\}}_{\mathrm{TMSS}}(|\alpha_{\mathrm{A}}|, |\alpha_{\mathrm{B}}|, \phi_{\mathrm{A}}, \phi_{\mathrm{B}})$ in Eq.(3.53) and perform the integrals over the whole phase space to determine the elements $\{F_{\mathrm{th}}(n_{\mathrm{A}}, n_{\mathrm{B}})\}$ of the expected photon statistics matrix. We start with

$$\begin{aligned} F_{\mathrm{th}}(n_{\mathrm{A}}, n_{\mathrm{B}}) = (2\pi)^2 \int_0^{+\infty} \int_0^{2\pi} \int_0^{+\infty} \int_0^{2\pi} W^{\{\sigma,\tau\}}_{\mathrm{TMSS}}(|\alpha_{\mathrm{A}}|, |\alpha_{\mathrm{B}}|, \phi_{\mathrm{A}}, \phi_{\mathrm{B}}) \cdot \\ \cdot W_{n_{\mathrm{A}}}(|\alpha_{\mathrm{A}}|) W_{n_{\mathrm{B}}}(|\alpha_{\mathrm{B}}|) |\alpha_{\mathrm{A}}||\alpha_{\mathrm{B}}| \, d|\alpha_{\mathrm{A}}| d\phi_{\mathrm{A}} d|\alpha_{\mathrm{B}}| d\phi_{\mathrm{B}} \,, \end{aligned} \tag{3.60}$$

where we expressed all functions in polar variables and the term $|\alpha_{\mathrm{A}}||\alpha_{\mathrm{B}}|$ comes from the Jacobian determinant of the coordinate transformation.

The two integrals with respect to the angular variables only involve $W^{\{\sigma,\tau\}}_{\mathrm{TMSS}}$:

$$\begin{aligned} f(|\alpha_{\mathrm{A}}|, |\alpha_{\mathrm{B}}|) = \int_0^{2\pi} \int_0^{2\pi} W^{\{\sigma,\tau\}}_{\mathrm{TMSS}}(|\alpha_{\mathrm{A}}|, |\alpha_{\mathrm{B}}|, \phi_{\mathrm{A}}, \phi_{\mathrm{B}}) \, d\phi_{\mathrm{A}} d\phi_{\mathrm{B}} = \\ = u(\sigma, \tau) \cdot 4\pi^2 I_0 \left(-2|\alpha_{\mathrm{A}}||\alpha_{\mathrm{B}}| \frac{\sigma^2 - \tau^2}{\sigma^2 \tau^2} \right) , \end{aligned} \tag{3.61}$$

where we defined $u(\sigma, \tau) = \frac{4}{\pi^2 \sigma^2 \tau^2}$ and $I_0(z)$ is a modified Bessel function. The expression for the generic element of the photon statistics matrix then reads

$$F_{\mathrm{th}}(n_{\mathrm{A}}, n_{\mathrm{B}}) = (2\pi)^2 \int_0^{+\infty} \int_0^{+\infty} f(|\alpha_{\mathrm{A}}|, |\alpha_{\mathrm{B}}|) W_{n_{\mathrm{A}}}(|\alpha_{\mathrm{A}}|) W_{n_{\mathrm{B}}}(|\alpha_{\mathrm{B}}|) |\alpha_{\mathrm{A}}||\alpha_{\mathrm{B}}| \, d|\alpha_{\mathrm{A}}| d|\alpha_{\mathrm{B}}| \,, \tag{3.62}$$

which leads to

$$F_{\rm th}(n_{\rm A},n_{\rm B}) = \frac{4^3}{\sigma^2\tau^2}(-1)^{n_{\rm A}}(-1)^{n_{\rm B}}\int_0^{+\infty}\int_0^{+\infty} I_0\left(-2|\alpha_{\rm A}||\alpha_{\rm B}|\frac{\sigma^2-\tau^2}{\sigma^2\tau^2}\right)\cdot \\ \cdot\,\mathcal{L}_{n_{\rm A}}\left(4|\alpha_{\rm A}|^2\right)\mathcal{L}_{n_{\rm B}}\left(4|\alpha_{\rm B}|^2\right)e^{-2(|\alpha_{\rm A}|^2+|\alpha_{\rm B}|^2)}d|\alpha_{\rm A}|\,d|\alpha_{\rm B}|\,. \tag{3.63}$$

We recall that $\mathcal{L}_n(z)$ is a Laguerre polynomial (see Chapter 1, Section 1.2).

This formula provides analytical expressions for all matrix elements $\{F_{\rm th}(n_{\rm A},n_{\rm B})\}$. We chose to truncate the reconstructed matrix to ${n_{\rm A}}^{\rm max} = {n_{\rm B}}^{\rm max} = 2$ given the brightness of our downconversion source. Following a procedure analogous to the one considered earlier, we can estimate σ^2 and τ^2 numerically such that the quantity

$$R_2 := \sum_{n_{\rm A}=0}^{2}\sum_{n_{\rm B}=0}^{2}\left|F_{\rm th}(n_{\rm A},n_{\rm B}) - F_{\rm exp}^{\{\eta_{\rm A},\eta_{\rm B}\}}(n_{\rm A},n_{\rm B})\right|^2 \tag{3.64}$$

is minimised. Once again, $F_{\rm exp}^{\{\eta_{\rm A},\eta_{\rm B}\}}(n_{\rm A},n_{\rm B})$ is calculated from Eq.(3.55).

$P_{\rm UV} = 12\,{\rm mW}$		$P_{\rm UV} = 30\,{\rm mW}$	
$\eta_{\rm A} = 0.152$		$\eta_{\rm A} = 0.139$	
$\eta_{\rm B} = 0.167$		$\eta_{\rm B} = 0.187$	
σ^2	0.935	σ^2	1.263
τ^2	1.157	τ^2	0.948
res	$7.3\cdot10^{-8}$	res	$6.9\cdot10^{-5}$

Table 3.2 For the same two datasets considered previously, we list the outcomes of a different numerical minimisation based on the quantity R_2 (see Eq.(3.64)). Once again, 'res' stands for the residual of the minimisation. The detection efficiencies are experimentally determined.

We stress that in this case the photon distributions correspond to 'downconversion signal only' (that is, the LO is absent); however, we do not detect the full input state as we only measure the fraction transmitted by the PBSs in the chosen splitting

condition – which is given by $T = 0.9$ here. Therefore, the variances σ^2 and τ^2 associated with the TMSS are related to the optimal values through $\sigma^2_{\rm opt} = 0.9\,\sigma^2 + 0.1$, and similarly for $\tau^2_{\rm opt}$.

In Table 3.2 we summarise the results obtained for the two datasets considered previously. Fig. 3.11 and Fig. 3.12 show the experimental data along with the expected behaviour determined by the variances quoted in Table 3.2.

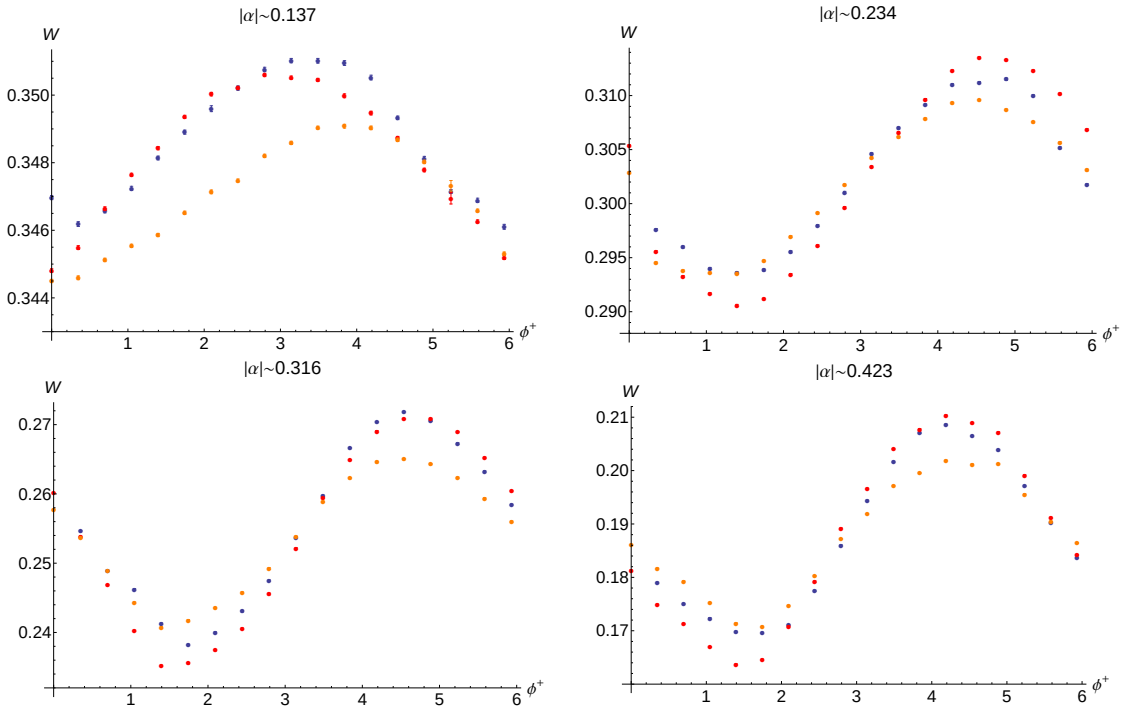

Figure 3.11 For $P_{\rm UV} = 12\,$mW, we show our sampled Wigner function for the squeezed vacuum and compare the experimental data points (blue dots) with two scenarios (see caption of Fig. 3.9). Here the theoretical graphs 'with squeezing' refer to the values of σ^2 and τ^2 given in Table 3.2. Error bars, determined by a Monte Carlo routine, are within the data points. As in Fig. 3.9, the agreement varies with the value of $|\alpha|$ and provides no definitive answer as to the successful estimation of squeezing with WFH detectors.

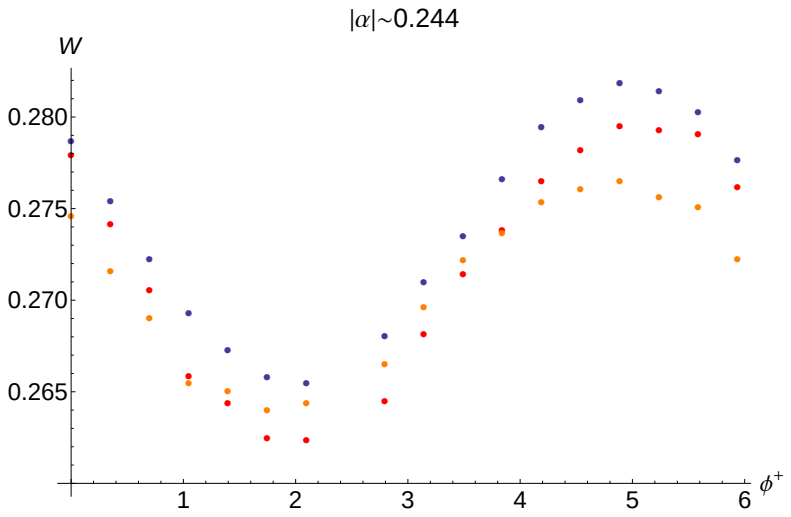

Figure 3.12 For $P_{\mathrm{UV}} = 30\,\mathrm{mW}$, we compare the experimental data (blue dots) with the same two scenarios considered in Fig. 3.9. The theoretical graph 'with squeezing' refers to the values of σ^2 and τ^2 quoted in Table 3.2, and $|\alpha|$ is estimated as an average over all phase settings and over both output modes. Error bars, determined by a Monte Carlo routine, are within the data points. If we compare these graphs with those in Fig. 3.10, we observe that in this case the agreement between experiment and theory predicting one squeezed variance is not as striking. This outcome seems to suggest that the obtained result is encouraging although it does not provide conclusive evidence of success.

Results and limitations of the present study

As a way to compare the two approaches leading to the numerical estimates of σ^2 and τ^2 given in Table 3.1 and Table 3.2, we can compute the elements of the theoretical photon statistics matrix determined by the pairs of optimal variances. This allows us to calculate how 'distant' these expected matrices are from the experimental ones provided that we identify an appropriate metric for the comparison: we choose $||F_{\mathrm{th}} - F_{\mathrm{exp}}^{\{\eta_{\mathrm{A}},\eta_{\mathrm{B}}\}}||_2$, which corresponds to the largest singular value of the considered matrix. The outcome of this investigation is found in Table 3.3.

$||F_{\mathrm{th}} - F_{\mathrm{exp}}^{\{\eta_{\mathrm{A}},\eta_{\mathrm{B}}\}}||_2$ is smaller for the values of the variances determined by the least

squares fit applied to the reconstructed photon matrices. In fact, we do expect this calculation to give a better agreement between the two quantities; it is precisely the fact that this approach is bound to output small values for $||F_{\text{th}} - F_{\text{exp}}^{\{\eta_{\text{A}},\eta_{\text{B}}\}}||_2$ which makes it a useful term of comparison for the figures shown in the first column of Table 3.3. For instance, when we look at the data corresponding to the setting $P_{\text{UV}} = 30\,\text{mW}$, the value of $||F_{\text{th}} - F_{\text{exp}}^{\{\eta_{\text{A}},\eta_{\text{B}}\}}||_2$ obtained from the variances in Table 3.1 is only marginally higher than that based on the information reported in Table 3.2. The discrepancy is more pronounced for the low-power data, where the difference amounts to more than one order of magnitude.

	$\|\|F_{\text{th}} - F_{\text{exp}}^{\{\eta_{\text{A}},\eta_{\text{B}}\}}\|\|_2$	
	(σ^2, τ^2) from Table 3.1	(σ^2, τ^2) from Table 3.2
$P_{\text{UV}} = 12\,\text{mW}$	$6.9 \cdot 10^{-2}$	$4.3 \cdot 10^{-3}$
$P_{\text{UV}} = 30\,\text{mW}$	$5.6 \cdot 10^{-2}$	$1.3 \cdot 10^{-2}$

Table 3.3 We compute $||F_{\text{th}} - F_{\text{exp}}^{\{\eta_{\text{A}},\eta_{\text{B}}\}}||_2$ in order to compare the experimental and reconstructed photon statistics matrices for both considered datasets. Because F_{th} is a function of σ^2 and τ^2, we can evaluate the theoretical photon statistics matrix based on the two optimisation strategies that we discussed. The results listed in this table show that the two approaches yield similar outcomes for the high-power scenario, while there is a clearer disagreement when it comes to the low-power dataset.

With these remarks in mind, let us go back to the graphs in Figs. 3.9 to 3.12. The dataset corresponding to $P_{\text{UV}} = 12\,\text{mW}$ does not provide us with a unified picture (see Fig. 3.9 and Fig. 3.11). Both theoretical descriptions fail to capture the features of the experimental Wigner functions for all regimes (identified by different intensities of the LO). Although there are promising results – such as the plots corresponding to $|\alpha| \simeq 0.316$ – it would be premature to claim that we can directly observe squeezing from this data. If we now refer to Fig. 3.10 and Fig. 3.12, we

see that the former figure shows good agreement between our data and the model predicting one squeezed variance for the Wigner function of the TMSS. However, the outcome in Fig. 3.12 is less clear-cut; if we are to consider both approaches equally meaningful (as suggested by Table 3.3), this casts doubts on the absolute significance of the result shown in Fig. 3.10.

Two viewpoints can be adopted with respect to the issues associated with the direct reconstruction of the properties of a TMSS that we have just presented. On one hand, the limited agreement between our data and the theoretical predictions may depend, at least partly, on imperfections in our experimental layout which affect its performance – we can think of delicate aspects such as the efficiency of detection and the quality of the mode overlap between signal and coherent probes. In this view, one could envisage to modify the setup in order to replace the most critical components. On the other hand, the theoretical model could be adjusted so as to take into account such experimental imperfections. In previous experimental direct reconstructions of single-mode states [73, 74], the authors addressed some effects of mode mismatch in weak-field homodyne schemes; as for non-ideal detection, modelling it through loss matrices associated with the considered detectors makes the characterisation of the system loss-tolerant [74].

Finally, we note that in the presence of a detector with non-unit efficiency $\eta \neq 1$ it is possible to rewrite Eq.(3.37) as [27]

$$W^{\eta}_{\mathrm{out}}(0) = \frac{1}{\eta T}\mathcal{W}_{\mathrm{signal}}\left(\sqrt{\frac{1-T}{T}}\alpha; -\frac{1-\eta T}{\eta T}\right) \tag{3.65}$$

for the single-mode case. This result becomes important as soon as we do not observe the studied state 'after loss', but invert the loss matrix in Eq.(3.7) instead. We see that the order parameter now depends on the transmittivity of the interference beam splitters as well as on the detection efficiency. Therefore, for fixed (T, η) one reconstructs a quasi-probability distribution with order parameter $\left[-(1-\eta T)/(\eta T)\right]$ – the higher the efficiency of detection, the closer $\mathcal{W}_{\text{signal}}$ is to the Wigner function of the input state. In the original theory of s-ordered operator expansions by Cahill and Glauber, we remark that the order parameter is indeed taken to vary continuously in the complex plane; however, it is not clear what the physical significance of a quasi-probability distribution function $\mathcal{W}(\alpha; s)$ with arbitrary s would be.

The investigation carried out in this chapter constitutes a first study of the capabilities of our weak-field homodyne detection setup, which we tested on the direct retrieval of the properties of a quantum state in a two-mode layout. On a more general note, the difficulties encountered when estimating the variances of the TMSS from the coincidence counting statistics through the reconstruction of the corresponding detection probabilities reaffirms the importance of robust methods to quantify key properties of quantum states with minimal data post-processing [64]. In this sense, theoretical proposals and experimental demonstrations have proved that the counting statistics can also be informative about specific aspects of given quantum resources. For example, click counts allow for the observation of a signature of non-classicality – the sub-binomial character of the counting statistics [75] – for different classes of single-mode quantum states [76].

Chapter 4

Direct observation of non-classical optical coherence

In the previous chapter we reviewed weak-field homodyning, a technique that offers a valid alternative to its strong-field analogue for applications to quantum information. We presented key concepts such as the difference between counting and photon statistics, and computed the expressions for phase-dependent detection probabilities in a WFH layout. Furthermore, we investigated how to directly access important properties of a given two-mode quantum state with weak-field homodyne detectors, building on previous theoretical and experimental work for single-mode schemes.

Here we report on the application of weak-field homodyne detection to the study of a specific type of quantum optical coherence [77]. The observation of this phenomenon contributes to ongoing research into the role and characterisation of coherence as a resource. From a more practical viewpoint, this experiment constitutes a full testbed for the capabilities of our WFH technique combining phase sensitivity

and photon-number resolution. Indeed, the results discussed in Chapter 3 suggested strengths and limitations of our proposed layout; here we shall analyse some relevant aspects of the experimental setup with greater detail.

This chapter is structured as follows: in the first section we motivate our investigation and provide technical insights into the experimental layout, from the generation of two-mode quantum states to their measurement. The second section is devoted to the interpretation of the data collected for a split single-photon state and a two-mode squeezed vacuum state, along with the theoretical models that we developed for this purpose. In the third and final section, we move onto a different albeit closely related topic and consider – from a purely theoretical standpoint – the violation of generalised Bell inequalities with weak-field homodyning.

4.1 Experimental realisation

4.1.1 Rationale for the investigation

The purpose of the experiments presented here is to bring together two aspects with relevant and promising roles in quantum information science. On the one hand there are quantum correlations, a key manifestation of fundamental quantum theory and an invaluable resource for quantum-based technologies. On the other hand there is the growing interest for hybrid approaches to QIP, whereby it becomes possible to exploit the dual nature of the electromagnetic field. A rather natural development is then to consider quantum correlations that manifest themselves *across* the wave and particle regimes. Are there ways to access these phenomena? How can we

take advantage of the interplay between quadrature and particle entanglement for quantum enhancement? These questions drive the present study, which is limited in scope yet contributes to gaining better understanding, access and control over such quantum correlations.

Optical coherence is an example of correlations exhibited between light fields. In a picture that suits both classical and quantum phenomena, one can regard coherence as a well-defined relation between (optical) phases; this is the viewpoint adopted in the present chapter.

Let us reconsider the results obtained in Chapter 3 to highlight the significance of Eq.(3.21) (for single-mode states) and Eq.(3.25) (two-mode case) for our current purpose. Given a generic state expressed in the photon-number basis, our WFH detectors displace each Fock layer into a state $|\alpha; n\rangle$ and subsequently record clicks produced by the total output state with mode multiplexers. In this way we access the probability amplitudes $\{\langle m|\alpha; n\rangle\}$, where

$$\begin{aligned}\langle m|\alpha; n\rangle &= \langle m| \sum_{\kappa=0}^{n} \binom{n}{\kappa} (\hat{a}^\dagger)^\kappa (-\alpha^*)^{n-\kappa} |\alpha\rangle = \\ &= \sum_{\kappa=0}^{n} \binom{n}{\kappa} \frac{\sqrt{m!}}{(m-\kappa)!} (-1)^{n-\kappa} |\alpha|^{m+n-2\kappa} e^{i(m-n)\phi} e^{-|\alpha|^2/2}\end{aligned}$$

for fixed α and n, m varying in a range determined by the brightness of the source and the resolution of the PNRDs. As we sum over n, we effectively address the output state layer by layer. At the same time, the terms $e^{i(m-n)\phi}$ (see above) which appear in Eq.(3.21) (and Eq.(3.25), reproduced below) establish well-defined phase relations between these Fock states. Consequently, we expect a coherent modulation

of the detection probabilities as we change the phase of the coherent-state probes. In other words, we deconstruct the observed quantum state into its discrete photon-number building blocks thanks to photon counting, and we detect the coherence present in this layered structure through weak-field homodyning. The two-mode case, which is of interest to us here, does not differ conceptually from what happens with single-mode states. Indeed, it is now the coherence across *joint* detection events that we observe in the modulation of the joint detection probability described by Eq.(3.25):

$$F(m,m') = \sum_{k=0}^{+\infty}\sum_{k'=0}^{+\infty} k!\,k'!\,r^{2k}(r')^{2k'}\left|\sum_{n=k}^{+\infty}\sum_{n'=k'}^{+\infty} c_{nn'}\binom{n}{k}\binom{n'}{k'}\cdot \right.$$
$$\left.\cdot\, t^{n-k}(t')^{n'-k'}\langle m|-r\alpha;n-k\rangle\langle m'|-r'\alpha';n'-k'\rangle\right|^2 .$$

The amplitudes $\langle m|-r\alpha;n-k\rangle$ and $\langle m'|-r'\alpha';n'-k'\rangle$ are responsible for the dependence on the LO phases ϕ,ϕ' (see above). The quantities $\{c_{nn'}\}$ are the coefficients of a generic two-mode state written in the Fock basis.

In this thesis we shall consider two special classes of two-mode quantum fields: a split single-photon state (SSPS) and a squeezed vacuum state (TMSS). The former is one of the most basic instances of two-mode quantum state. The squeezed vacuum is a most prominent example of a quantum resource characterised by strong correlations between its Fock layers; for this reason, it constitutes the ideal candidate for our experimental demonstration of optical coherence across number states.

4.1.2 Layout and test of individual components

Now that we have clarified the purpose of our investigation, we set out to describe the specific implementation that we adopted. The main building blocks shown in

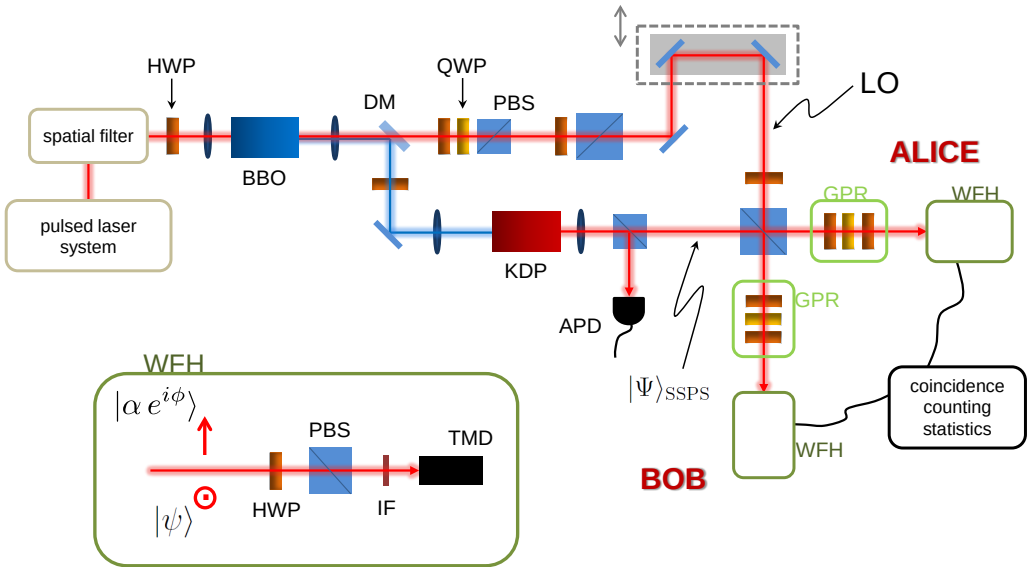

Figure 4.1 The setup for the study of the SSPS via WFH detection can be divided into three main stages. The beam preparation starts with the laser system, followed by spatial filtering and frequency doubling of the infrared beam into a non-linear crystal (BBO – see text). Second, we perform local operations in each arm of the interferometer identified by the DM and the PBS where the PDC signal and the local oscillators recombine. One PDC mode is detected by an APD straight after the non-linear medium (KDP – see text), acting as a herald for its twin beam. The LO path includes a polarisation cleaner and a power control. Finally, the two-mode output state is measured with two WFH detectors; a geometric phase rotator (GPR) allows us to vary the phase ϕ of the LO in each output mode (see inset). Temporal overlap at the recombination PBS can be optimised thanks to the motorised delay stage in the LO path. Interference filters (IF – $\Delta\lambda_{\mathrm{IF}} \simeq 3\,\mathrm{nm}$) precede each time-multiplexed detector (TMD) to ensure spectral overlap between signal and local oscillator; we do not filter the herald mode in order to have higher coincidence rates. Spatial indistinguishability is partially guaranteed by coupling each output mode into single-mode fibres connected to our detectors (not shown).

Fig. 4.1 – and Fig. 4.2, with some notable modifications – were already mentioned in the previous chapter; however, we voluntarily postponed a more detailed discussion

of the features of each constituent to the current chapter.

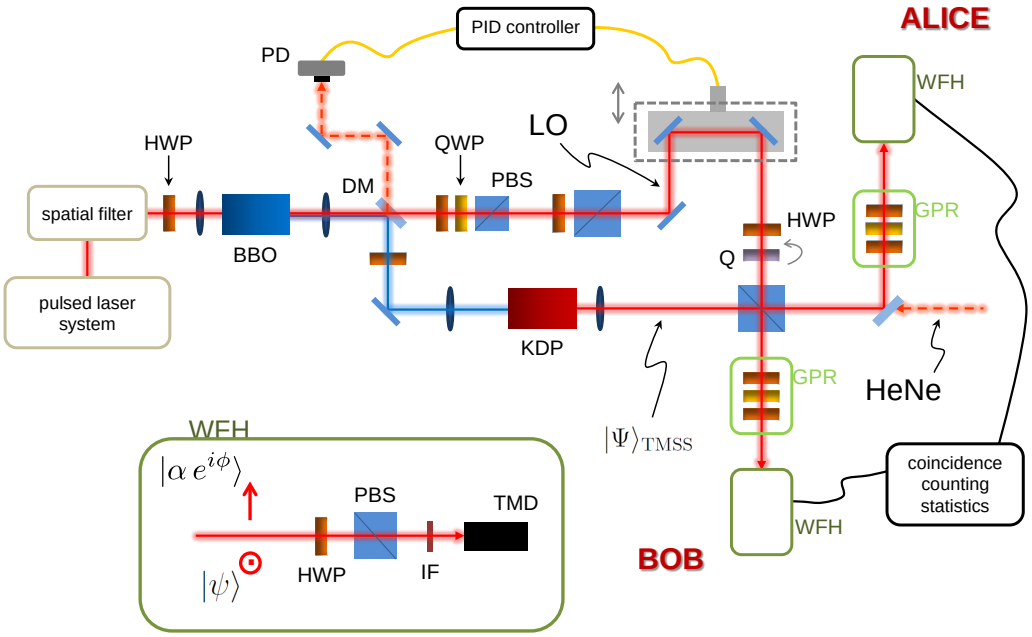

Figure 4.2 The setup for the study of the TMSS via WFH detection is almost identical to the layout adopted to observe a split single photon. A notable addition is the back-propagating ancillary laser beam (HeNe – indicated as a dashed red line) which constitutes the signal for our active phase locking mechanism. The classical interference pattern observed after the DM is detected by a photodiode (PD): this allows us to implement a feedback loop controlled by a PID device connected to the translation stage in the LO path (see text for details). Once more, we adjust the temporal overlap between signal and local oscillators at the recombination PBS with the motorised delay stage shown in the sketch; however, we must add a birefringent element (quartz, Q) in order to account for the temporal walk-off inside the KDP crystal (see text). The interference filters (IF) preceding each TMD ensure spectral overlap: in this case they have different widths, depending on which output polarisation mode is detected ($\Delta\lambda_{\mathrm{IF}}(\mathrm{H}) \simeq 3\,\mathrm{nm}$, $\Delta\lambda_{\mathrm{IF}}(\mathrm{V}) \simeq 10\,\mathrm{nm}$ – see text).

Laser beam preparation

By 'beam preparation' we refer to the parts of the setup that determine the features of our main infrared (IR) beam. As illustrated in Fig. 4.3, the first element is

the laser system. This delivers femtosecond pulses centred at $\lambda_{\mathrm{IR}} = 830\,\mathrm{nm}$ (see caption of Fig. 4.3 for additional specifications). Unfortunately, a number of factors contributed to a gradual degradation of the laser performance over time, making it less reliable on a daily basis – in terms of peak power and quality of the output mode. When we rebuilt the setup in 2013 to achieve a compact design that would be more reproducible in its alignment while ensuring better passive stability, it also became

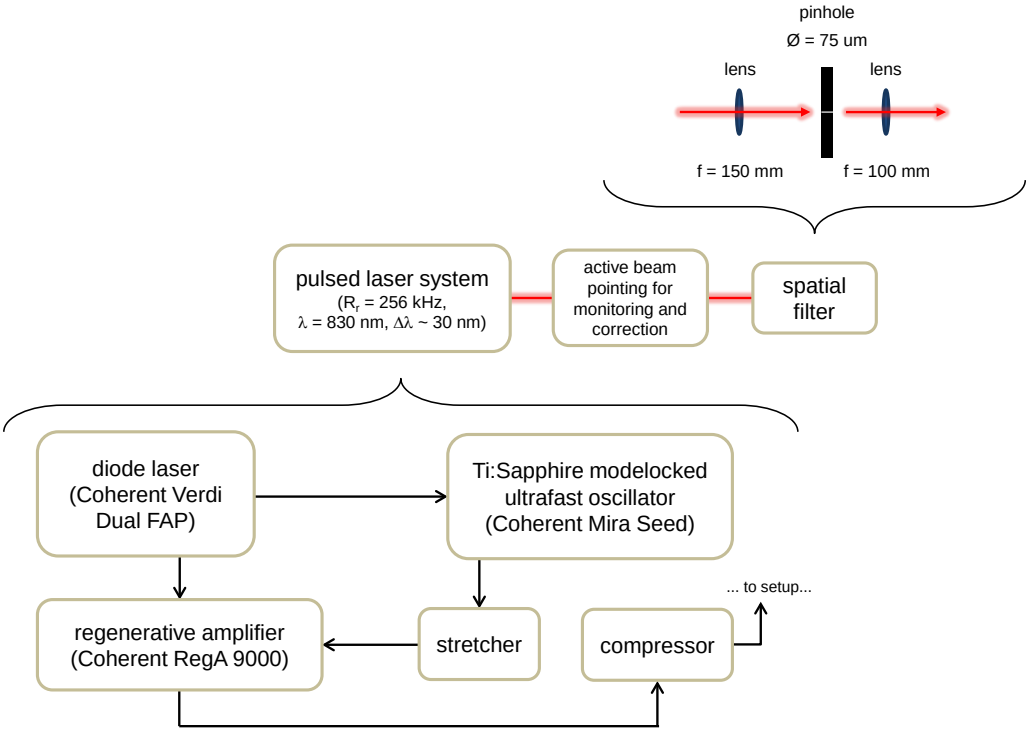

Figure 4.3 The combination of the Ti:Sapphire oscillator with the regenerative amplifier reduces the repetition rate R_{r} from 80 MHz to 256 kHz – a limitation imposed by the detectors, as we shall see later. When every component is correctly set, we record $P_{\mathrm{IR}} \simeq 1.3\,\mathrm{W}$ out of the compressor. The most delicate preparation step involves the oscillator, for which a reliable and stable condition of modelocking is necessary not to jeopardise the functioning of the amplifier. Before the spatial filter, a sequence of HWP and PBS controls the intensity of the initial beam; typical settings of the HWP produce an IR beam with P_{IR} between 30 mW and 80 mW after the spatial filter. The transmission through this element constitutes the main quantitative reference when the point locking system is active (see text).

apparent that the parametric source would benefit from a spatial filter. The latter is composed of a lens that focusses the IR beam onto a circular aperture, followed by a second lens that ensures the collimation of the beam throughout the setup. In order to reduce the area occupied by the filter on the optical table, we carefully chose the diameter of the aperture as well as the focal lengths of the lenses. For each combination of aperture size and lenses, we verified the collimation of the beam in the near and far field; a further check would involve aligning the parametric source to maximise the detection efficiencies, observing the effect of the spatial filter on the downconversion process. The geometry reported in Fig. 4.3 corresponds to the definitive choice of components. The transmission through the filter is a key daily check on our setup: drops in the transmitted IR power indicate a modified mode shape or, most probably, an issue with the reproducibility and stability of the beam pointing from the laser system. A home-built point locking software, conceived and realised by another D.Phil. student in the group, allows us to partially counteract the latter problem by monitoring the beam position on two CCD cameras, correcting for undesired changes in the pointing with two motorised mirrors preceding the spatial filter (see Fig. 4.3). In this sense, the transmission through the latter element is also an effective benchmark to evaluate the performance of the point locking system.

Following the spatial filter, the IR field is doubled in a type-I β-barium borate (BBO) crystal as shown in Fig. 4.1 and Fig. 4.2. The second-harmonic process inside the non-linear medium produces ultraviolet (UV) photons at $\lambda_{\mathrm{UV}} = 415\,\mathrm{nm}$. The position of the focussing lens before the crystal maximises the SHG conversion efficiency (typically around 20%), while the collimating lens following the BBO

ensures that the ultraviolet beam does not diverge as it reaches the second non-linear crystal. A dichroic mirror (DM) splits the residual IR radiation and the UV pump: from the DM on, we shall refer to the infrared beam as the local oscillator (LO) of our WFH scheme.

Parametric downconversion source

The ultraviolet beam pumps a type-II parametric downconversion (PDC) process in a potassium dihydrogen phosphate (KDP) non-linear crystal: this is our source of two-mode quantum states. The geometry of this bulk squeezer was conceived by a former D.Phil. student in the group, whose work focussed on the generation of heralded pure single photons [78]. To this end, the parametric source is designed so that group velocity mismatch inside the birefringent medium determines spectrally uncorrelated modes at the output [57, 79, 80]. The orthogonally polarised daughter photons have the same central wavelength $\lambda_{\mathrm{IR}} = 830\,\mathrm{nm}$; however, they have different spectral widths (see Chapter 2, Section 2.2). As shown in Fig. 4.4, we have $\Delta\lambda_{\mathrm{H}} \simeq 5\,\mathrm{nm}$ and $\Delta\lambda_{\mathrm{V}} \simeq 12\,\mathrm{nm}$.

The same source generates the split single-photon state and the squeezed vacuum. The brightness of the pump beam determines which class we observe: typically, $P_{\mathrm{UV}} < 10\,\mathrm{mW}$ for the SSPS, while P_{UV} could reach up to 30 mW for the squeezed vacuum. We can characterise the performance of our parametric source by estimating the second-order correlation function for the two single-mode output states detected on each time-multiplexed detector (also referred to as the marginal distributions in the following). For the SSPS, a typical experimental value is $g^{(2)} = 0.39 \pm 0.04$ [81];

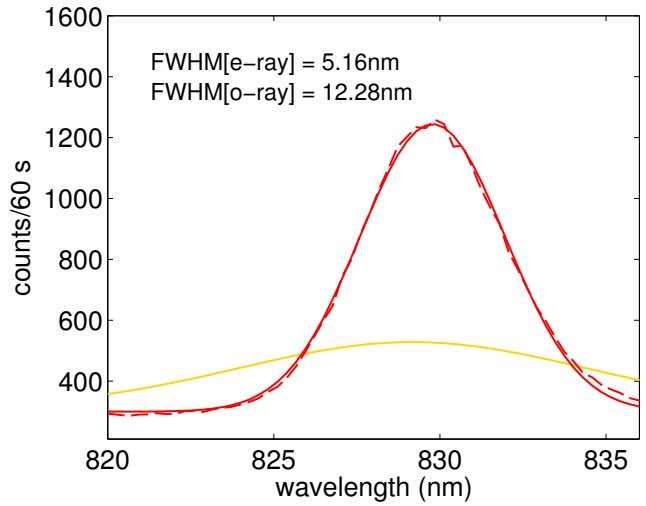

Figure 4.4 These curves correspond to the single-photon spectra for the two downconversion modes: the 'e-ray' is horizontally polarised (red – detected by Alice), while the 'o-ray' is vertically polarised (copper – measured by Bob). We fit the experimental data (dashed curves) with Gaussian functions (solid lines) to estimate the full width at half maximum (FWHM) and choose appropriate interference filters for the setup. We acquired this data with a single-photon spectrometre (Andor SR163 and DV420A).

this compares to $g^{(2)} = 0$ for a pure single photon. For the TMSS, if the PDC modes are spectrally uncorrelated we expect that the marginal distributions for the squeezed vacuum are those of thermal states, hence $g_{\mathrm{A}}^{(2)} = g_{\mathrm{B}}^{(2)} = 2$ (see Chapter 2, Section 2.2). Typical measured values are $g_{\mathrm{A}}^{(2)} = 1.92 \pm 0.04$ and $g_{\mathrm{B}}^{(2)} = 1.98 \pm 0.04$. In the next section we shall refer to these values and discuss the observed deviations from the ideal case.

The alignment and optimisation procedures for the parametric source are independent of the considered state. Fig. 4.5 illustrates the optical elements and diagnostics that allow us to control the PDC process. The orange and blue coloured glass filters OF and BF1 can block out one of the two wavelengths in use before the dichroic mirror which separates them. We found it more reliable to take advantage

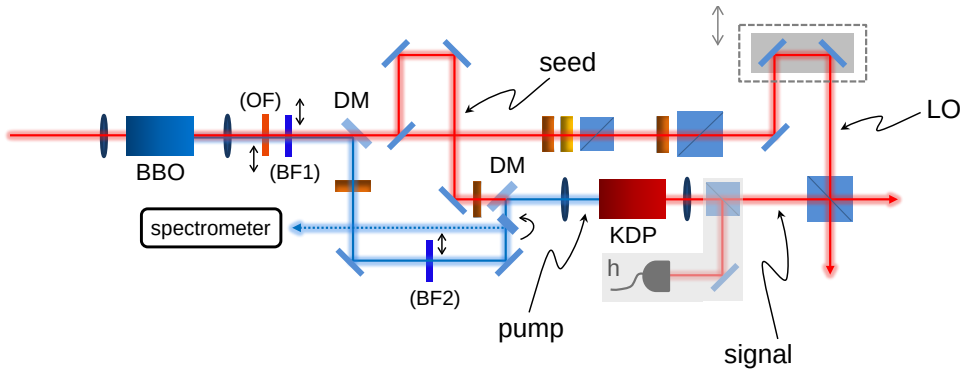

Figure 4.5 In this experimental sketch we include details that were previously omitted; these are not necessary to describe the general design of the layout, but they constitute useful diagnostics when aligning the setup and particularly the PDC source. A mirror on a flip mount allows us to monitor the spectrum of the UV pump as we optimise the SHG. We can adjust the phase matching condition for the KDP by shining the seed and the residual IR beam (reflected by the DM) on the crystal to observe SHG (see text); if we change the polarisation of the seed we should find a setting of its dedicated HWP which frustrates the second-harmonic emission, thereby confirming that the effect is genuine. The same reasoning holds for the downconversion process: this justifies the presence of a HWP after the DM on the pump beam path. The role of the coloured filters (OF, BF1 and BF2) is discussed in the text. We note that the heralding APD (labelled 'h' in the sketch) is only present for the study of the SSPS.

of a bright signal – labelled 'seed' in Fig. 4.5 – as a reference for coarse alignment. The seed is also useful to check the phase matching condition in the non-linear medium: if the crystal is correctly set, one should observe SHG as the pump and seed beams interact with the KDP.

The *ab initio* alignment of the setup proceeds as follows:

1. Verify transmission through spatial filter with point locking on (expected to be above 85%) and align IR beam to irises around BBO.
2. Optimise SHG by looking at UV pump power and spectrum (BF1, BF2 inserted).
3. Align seed beam to irises around KDP (OF inserted).

4. Align UV pump to irises; overlap with seed in far field (only BF2 inserted).
5. Shine pump and seed beams on KDP crystal to verify phase matching condition for PDC (see text above – OF inserted, hence the 'pump' identifies the fraction of IR radiation reflected from the first DM here).
6. Insert lenses around KDP (preferably with UV beam).
7. Add filters to block residual UV pump after KDP (BF1, BF2 inserted).
8. Align Alice's and Bob's fibre couplers with seed beam (OF inserted). For the SSPS, optimise position of coupler for herald signal in the same way.
9. Couple local oscillator into single-mode fibres (OF inserted).

Once this alignment with 'bright light' is completed, we can perform further tests:

I. With both blue filters inserted and OF moved to the LO path, we optimise the coupling into single-mode fibre (SMF) directly on the PDC signal. This procedure aims at maximising the recorded coincidence counts, and even more so the efficiencies of detection. At this stage we operate with standard APDs, but the same observation holds for time-multiplexed detectors (TMDs).

II. Alternatively, we focus on the temporal overlap between signal and local oscillator by looking at the (classical) spectral interference fringes between these two beams. To this end, we adjust the LO optical path length thanks to a dedicated motorised translation stage (see Fig. 4.5).

The first step is crucial when replacing avalanche photodiodes with time-multiplexed detectors, because the binary photon counters have higher detection efficiencies and are therefore easier to align on the PDC signal. The spectral interference pattern

allows us to evaluate the performance of our active phase stabilisation system by monitoring the classical fringes over time (see paragraph on phase sensitivity).
On a daily basis, we only repeat steps 1 and 2 in the above procedure and then optimise the detection efficiencies of our TMDs (see step I).

The acquisition of all data produced by our detection system is based on a field-programmable gate array (FPGA); all coincidence counting software was developed by a former D.Phil. student in the group. A graphical user interface written in MATLAB displays counts and coincidences in real time, conveniently visualised as the elements of a matrix (see below). Particularly, this software allows us to set, test and finely tune fundamental parameters such as the electronic delays for the time bins within each mode multiplexer [82]. It is important to remark that coincidence counts have a different meaning depending on whether we observe the split single photon or the squeezed vacuum. In the latter case, coincident detection events are unheralded; the only temporal reference is a trigger signal from the RegA system which instructs the FPGA to record clicks whenever it registers a trigger event. When we probe the SSPS we keep the temporal gating from the external trigger; we then record coincidence counts from the two TMDs heralded by a detection event on the APD following the parametric source (see Fig. 4.1).

Mode overlap between quantum signal and coherent probe

As with most homodyning schemes, the successful operation of our WFH layout relies on two main aspects: how well the local oscillator overlaps with the signal, and how well we detect incoming photons. We note that in a weak-field homodyne

detection setup, indistinguishability between signal and coherent-state probe must be regarded differently from the strong-field scheme. Since the latter relies on the difference between the two detected output signals to estimate the variance of the field quadratures, noise in the local oscillator is automatically discarded; in fact, the LO defines the detection mode. The same is not true when the signal interferes with a reference of comparable mean photon number. The local oscillator does not act as a filter anymore: we detect the total output state as affected by mode mismatch as it is. At the optical level, poor quality of the detected modes, misalignment of the interference filters and/or unoptimised coupling into SMFs can all decrease the detection efficiencies. The latter are also limited by the design of our TMDs, which is structurally prone to loss (see paragraph on temporal multiplexing).

Our two-mode WFH layout relies on a collinear geometry for the parametric source and the detection system, as illustrated in Fig. 4.1 and Fig. 4.2. Each mode of the considered state is recombined with a local oscillator of orthogonal polarisation at a PBS. In the ideal case, this delivers a signal and weak coherent beam in a common spatial mode in both monitored output arms. Temporal indistinguishability is guaranteed by the adjustable LO path length, and it can be tested through Hong-Ou-Mandel interference (see below). In the spatially separated output modes, the HWP and PBS of each WFH detector erase the information about the polarisation of the signal and the coherent state, thus realising interference between these two fields. At this stage, there is one degree of freedom which still makes the quantum state and the LO distinguishable: as we already noted, the downconverted photons have distinct spectral widths, and these in turn differ from the width of the

local oscillators. To ensure spectral overlap, suitable interference filter are placed before the coupling stages. We can verify the outcome of the filtering operation by

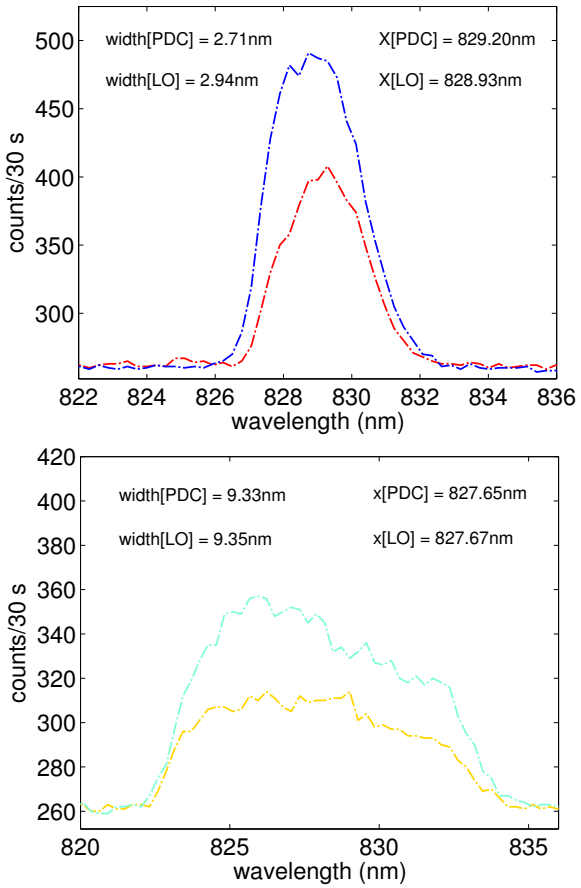

Figure 4.6 The dashed-dotted curves are experimental spectra corresponding to the filtered signal and LO in Alice's (red and blue, respectively) and Bob's output arms (gold and aquamarine). The values of the widths and central wavelengths for all curves indicate that the filters work as expected. These spectra were acquired with a single-photon spectrometer (Andor SR163 and DV420A).

measuring the filtered spectra for the PDC signal as well as for each LO: typical results are shown in Fig. 4.6. Finally, single-mode fibres on both output channels select the modes detected via time-multiplexed photon counting.

To optimise and test the quality of the achieved temporal overlap, we record HOMI patterns (see Chapter 2, Section 2.1) by changing the LO path length to find

the condition of zero delay. Fig. 4.7 and Fig. 4.8 show examples of HOMI scans for the SSPS and the TMSS, respectively.

For a split single photon, the lowest value of three-fold coincidence counts identifies the condition of temporal overlap between signal and coherent-state probes (see Fig. 4.7). On the other hand, the successful application of WFH detection to

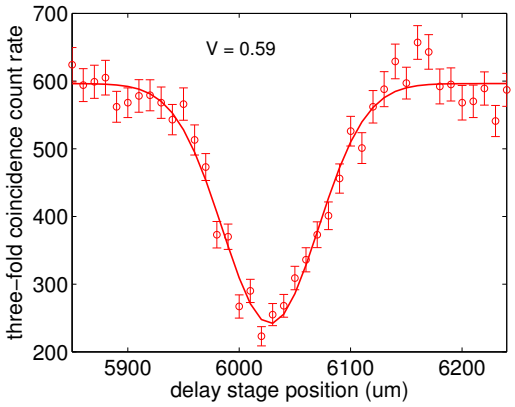

trigger from herald	(coinc. with herald - coinc.) on A.'s mode (1,0) term	(2,0) term
(coinc. with herald - coinc.) on B.'s mode (0,1) term	(1,1) coinc. term 3-fold coinc. counts for HOMI	(2,1) coinc. term
(0,2) term	(1,2) coinc. term	(2,2) coinc. term

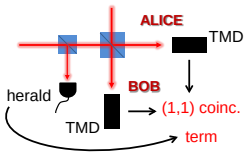

Figure 4.7 The red data points (with error bars from a Monte Carlo simulation assuming Poissonian statistics for the raw counts) show a dip in the coincidence counts as we interfere the SSPS with the coherent fields. The solid curve is a Gaussian fit that provides us with the estimated dip visibility. We note that this data includes spurious contributions such as background counts (see following section). To clarify how we observe HOMI as a daily check preceding the measurement of phase-sensitive joint counting statistics, we schematically show the origin of three-fold coincidence events in our detection setup. We can also conveniently visualise counts and coincidences as the elements of a matrix (on the right).

a two-mode squeezed state requires two temporal conditions to be met, as illustrated in Fig. 4.8 and Fig. 4.9. In this case we detect the full state produced by parametric downconversion; consequently, the first condition entails the overlap of each temporal mode from the squeezer with a local oscillator. However, to detect the full two-mode output state with optimised temporal overlap on both channels we also need to identify one common position for the translation stage in the LO

path, i.e. the temporal modes of both coherent fields must map those of the PDC signal. One question may then arise: why would not the two zero-delay settings of the translation stage coincide already? As mentioned in Chapter 2 (see Section 2.2),

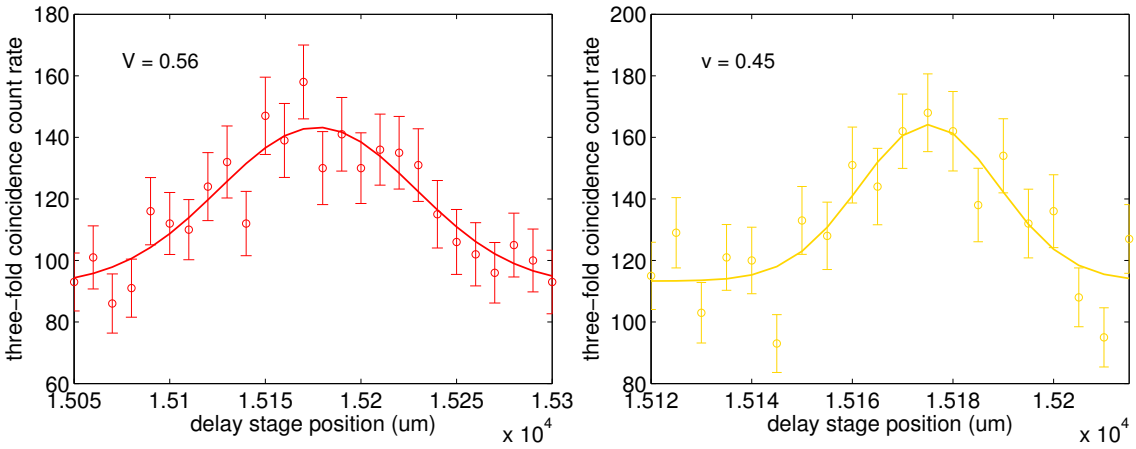

Figure 4.8 These graphs show the observed HOMI patterns for the TMSS: we now scan both the H-polarised (red plot) and V-polarised (gold plot) downconversion modes. The data points (with error bars from a Monte Carlo simulation assuming Poissonian statistics for the raw counts) show peaks in the coincidence counts rather than the more familiar dips – this is due to the way we perform the data acquisitions (see Fig. 4.9). The solid curves are Gaussian fits that provide us with the estimated peak visibilities. We note that this data includes background counts (see following section).

the production of degenerate photons in our source is determined by a specific condition of asymmetric group velocity matching – horizontally and vertically polarised light quanta do not travel at the same speed inside the non-linear medium. Most importantly, this implies that their emission times out of the KDP crystal differ by Δt (which corresponds to a spatial difference Δx): it is this temporal walk-off that we account for when we identify a common zero-delay condition. The compensation of the walk-off can take place in the signal or the LO path; in our setup we chose the latter option, and inserted a quartz element prior to the recombination PBS

(see Fig. 4.2). If we choose the length of the birefringent medium so that it matches Δx, as the local oscillators propagate through the quartz crystal one polarisation mode will be slowed down due to the higher refractive index that it experiences. We estimate the temporal walk-off inside the KDP by running two HOMI scans in the absence of any compensation: $\Delta x_{\mathrm{PDC}} \simeq 140\,\mu$m for our source. A 10 mm-long quartz cube provides the correct delay: in the condition of normal incidence, $\Delta x_{\mathrm{quartz}} \simeq 90\,\mu$m. Further tilting of the crystal allows us to increase the portion of medium encountered by the coherent fields: in this way we can compensate for the walk-off almost completely, as shown in Fig. 4.9.

If we compare the visibilities of the HOMI curves associated with the SSPS and the TMSS, we notice a difference in the visibilities of the observed interference patterns. In the case of the squeezed vacuum, it would generally prove difficult to obtain very high values of V for both output modes simultaneously; we would often record worse interference for the V-polarised beam than for the H-polarised signal[1]. The theoretical study of Hong-Ou-Mandel interference between a single photon and a coherent state confirms that we are indeed below the predicted values for the accessible visibilities [83]. Interestingly, this model accounts for non-ideal detection efficiencies yet assumes pure input states. The expected values[2] for V are likely to

[1]We might consider the following interplay between the HOMI visibility V, the (half) width σ of the filtered signal and the width σ_{pump} of the pump beam (assuming Gaussian profiles for all considered fields): $V = 1/\sqrt{(1 + (\sigma^2/(2\sigma^2_{\mathrm{pump}})))}$. In this sense the closer the two widths, the lower the visibility [83]. While this is an insightful formula, we must stress that it relates to a layout where filtering is applied in order to obtain better spectral factorability (see Chapter 2, Section 2.2). In our setup this feature is achieved through a specific design for the downconversion source, hence the above expression should be regarded as a general guideline.

[2]For the interference to be recognised as non-classical, the visibility of the HOMI dip – or peak – must be higher than 0.5. Given our coherent-state intensities and detection efficiencies, the simulations reported in [83] indicate that we should expect values of V well above 0.6.

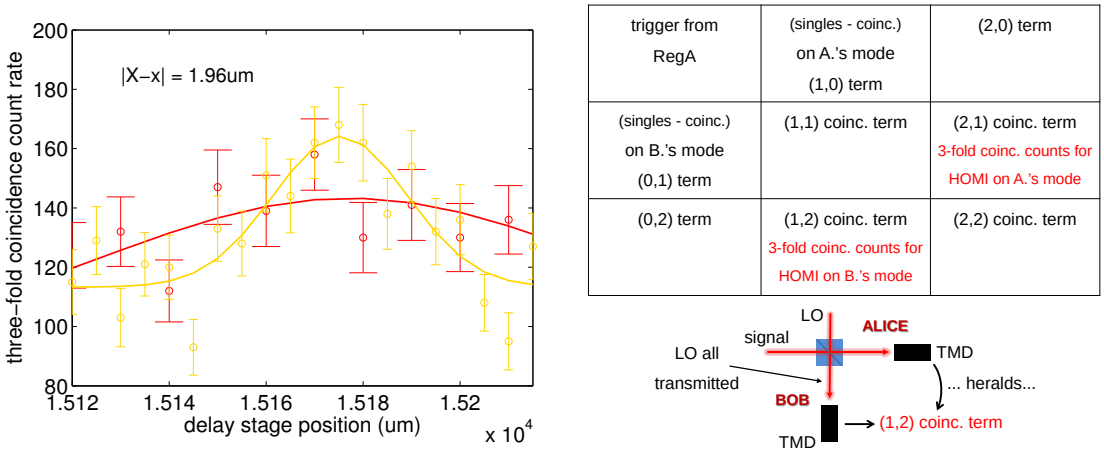

Figure 4.9 We superpose the two HOMI plots from Fig. 4.8 to highlight the second temporal requirement that must be met for the TMSS: once we find zero-delay conditions for both modes (identified by the abscissae of the maxima in the coincidence count rates, X and x), we need to find a common position for the translation stage in the LO path (see text) in order to probe the full two-mode output state – that is, we must minimise $|X-x|$. Similarly to Fig. 4.7, we also illustrate the origin and meaning of the coincidence count rates considered here.

decrease if the signal is not pure; we shall drop the hypothesis of perfect input signal in the theoretical descriptions discussed later in this chapter.

Finally, we note that our daily check of the HOMI curves for the TMSS is mainly motivated by the second requirement discussed above – accounting for the temporal walk-off of the PDC photons in the KDP. In this sense, we mostly monitor $|X-x|$ (see Fig. 4.9) and, when necessary, make adjustments to recover the lost overlap. This condition would be sometimes met at the expense of the HOMI visibilities, suggesting a potentially wider issue with the reproducibility of our experimental conditions.

Phase sensitivity and temporal multiplexing

In the introduction to the current section, we discussed the interest of our experimental demonstration of non-classical optical coherence across the Fock layers of two classes of two-mode quantum states. Because of the very nature of this phenomenon, a hybrid detection system such as our weak-field homodyne scheme is a most appropriate tool to reveal this type of coherence. So far we have provided details about a number of important building blocks in our experimental setup, but we have not yet discussed two overarching aspects: phase sensitivity and photon-number resolution. Indeed, both elements are necessary to access joint counting statistics that exhibit phase-dependent coherent oscillations.

In order to perform phase-sensitive measurements, we must be able to scan the phase of the weak coherent states as well as to ensure phase stability when this is required. Specifically, we want to vary the relative phase between the input signal and each LO; following the scheme adopted in [26], we insert two geometric phase rotators which change the coherent-state phases locally on both detection channels (see Fig. 4.1 and Fig. 4.2). Each geometric phase rotator (GPR – also known as Berry phase rotator) is composed of a quarter-wave plate (QWP), a half-wave plate and a second QWP. The calibration of this optical element is crucial, in that it makes a major contribution to the quality of the collected data. To this end, all wave plates must be individually calibrated; the interference PBSs following the GPRs also need to be carefully aligned to minimise the reflected outputs. Once every relevant optical component is calibrated and correctly aligned, each GPR is set to produce arbitrary

phase rotations. The axis of the first QWP is set to $\pi/4$: this transforms the input linear polarisations into circular ones. Rotating the HWP by $\phi/4$ results in a phase shift equal to ϕ between left- and right-circular polarisations. The initial linear polarisations are recovered by setting the second QWP to $\pi/4$. With a well-calibrated GPR it is possible to record power fluctuations below 5%; by contrast, imperfections in the calibration of one of its constituents can lead to fluctuations in power above 10%. It is thus important to characterise the performance of the GPRs in use, as such pseudo-periodical changes in the photon counts add an undesired phase-dependent contribution to the non-classical oscillations of the joint counting statistics. Fig. 4.10 shows the calibration curve of a GPR on counts from the LO.

Before we turn to phase stability and active locking, we must stress a few key differences between the study of the SSPS and that of the TMSS. As we set out to measure phase-dependent joint counting probabilities, we must know what phase dependence to expect for the considered classes of states. In their investigation of single-photon non-locality via WFH, Hessmo and coworkers showed that the probability of three-fold coincident counts (that is, of simultaneous *heralded* clicks in both detectors) depends on the phase difference $\phi^{(-)} = \phi_{\mathrm{A}} - \phi_{\mathrm{B}}$, where ϕ_{A} and ϕ_{B} are the individual LO phases [26]. For the two-mode squeezed state, we refer to the results obtained in the previous chapter: in the expression for the Wigner function of a TMSS mixed with coherent fields we have a clear dependence on the phase sum $\phi^{(+)} = \phi_{\mathrm{A}} + \phi_{\mathrm{B}}$. This is also what Kuzmich and collaborators found in their study on the violation of Bell's inequality with a squeezed vacuum probed in a WFH scheme [84]: they recorded three-fold coincidence counts and showed that the phase

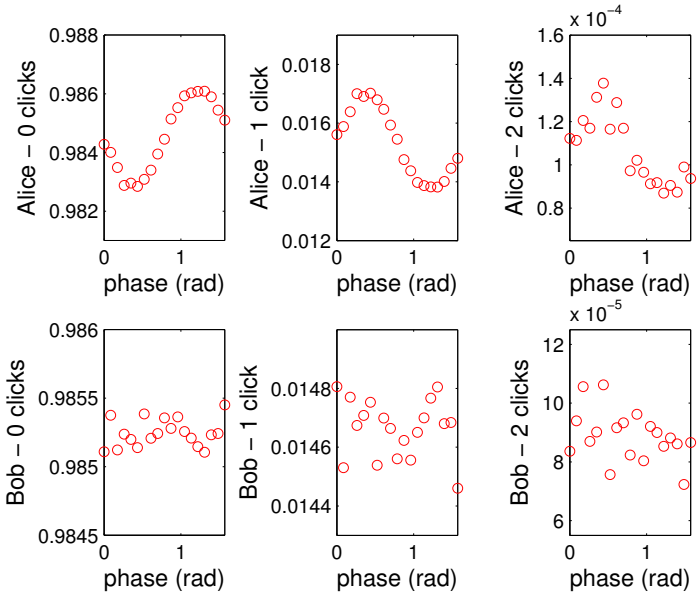

Figure 4.10 To calibrate the geometric phase rotators we interfere the vacuum with the local oscillator and record counts on one detector as we scan the position of the motorised HWP (in this case, in Alice's arm). A partial trace operation on the joint counts so obtained leads to the plots shown here. We observe oscillations in the clicks recorded with Alice's detector; the LO counts vary by less than 1% if we look at the trigger (0 'clicks'), while the '1-click' and '2-click' terms exhibit a modulation of the recorded counts as we change the LO phase. We have $V \simeq 0.1$ for 1 'click', and the visibility is even higher for the '2-click' term (although the absolute values are of the order of 10^{-4} counts/s). We shall refer back to these values when we examine the marginal distributions of counts for our experimental two-mode states.

dependence for this detection probability is $\tilde{\phi}^{(+)} = \phi^{(+)} - \theta$, where θ is the phase which the TMSS inherits from the doubled pump field (see Chapter 2, Section 2.2). This result highlights an additional difference between the SSPS and the TMSS.

These findings lead to the following practical observations. As noted in previous applications of WFH detection [26, 85], the collinear geometry that we adopted is advantageous because it ensures that the relative phase between the two modes in each output beam path is preserved. Therefore, when we consider the SSPS we do not need active phase locking: the individual phase rotators in each output arm

allow us to vary the relative phase between the two coherent-state references [26] – in fact, it is sufficient to change one LO phase. As we switch to the TMSS, however, we need to prevent the relative phase between the signal and the LOs (in the interferometer identified by the DM and the recombination PBS) from fluctuating freely during a data acquisition; this is not automatically guaranteed by our collinear WFHs. For this reason, we must implement an active phase locking system for the study of the two-mode squeezed vacuum state.

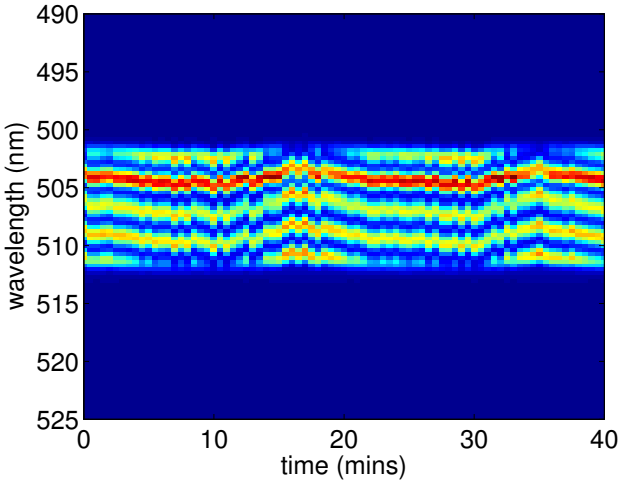

Figure 4.11 This is a graphical representation of our 'freely running' experimental setup: we monitor the classical interference pattern between signal and local oscillator over time in the absence of active phase locking (see text). Phase drifts are then visualised as wavelength shifts affecting the spectral fringes. An estimate of the phase fluctuations can be obtained by fast Fourier transform. We note that the spectrometer (Ocean Optics USB4000) used for the data acquisition was not calibrated prior to this measurement, which explains why the wavelength range is not the one expected for our setup. The same comment applies to Fig. 4.12.

Let us first quantify the phase fluctuations that take place in our setup over the time frame of a data acquisition. To this end, we record the classical interference pattern discussed earlier (see paragraph on the PDC source, test II following the

full alignment procedure): as illustrated in Fig. 4.11, if we monitor the interference fringes over a time scale comparable to that of an experiment, we record fluctuations of about 9° in the absence of any correction mechanism.

The active phase stabilisation uses an ancillary laser beam from a continuous-wave helium-neon (HeNe) laser ($\lambda_{\mathrm{HeNe}} = 633\,\mathrm{nm}$) that back-propagates through the interferometer (see Fig. 4.2). When this ancillary beam reproduces correctly the signal and LO optical paths, classical interference fringes are visible in the transmitted output arm of the dichroic mirror. A linear photodiode can thus detect this pattern and record shifts in the fringes as bright areas become dark and vice versa (provided that there is enough contrast). The electrical signal generated by the PD is then sent to a proportional-integral-derivative (PID) controller (SRS SIM960); this device connects to the motorised translation stage in the LO path. In this

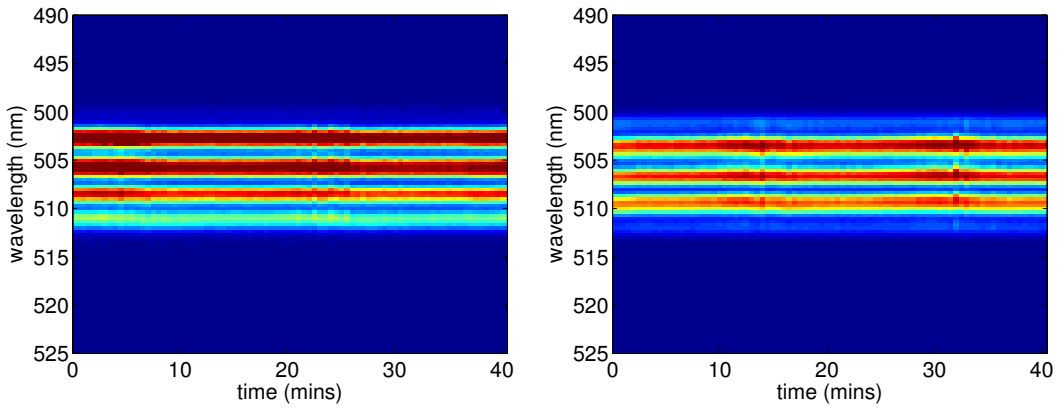

Figure 4.12 If we compare these graphs to the one in Fig. 4.11, the different behaviour is visible: no notable wavelength drift can be seen here. The two plots show data taken in two distinct experimental conditions: in one case the brightness of the fraction of HeNe beam coming from the signal path was comparable to that associated with the LO path (left plot). By contrast, in the second case we voluntarily unbalanced the two contributions to see whether this would affect the quality of the interference in a way that could jeopardise the locking: despite the imbalance, we do not record higher phase fluctuations.

way, the PID controller realises a feedback loop whereby phase shifts detected on the HeNe interference pattern are counteracted by finely adjusting the LO optical path length. The PID controller monitors the output signals in real time: this is important because, for example, it can warn us of sudden phase variations that are not successfully corrected for. We stress that classical interference fringes with high visibilities guarantee a more reliable response from the PID device. Fig. 4.12 shows two temporal scans of the spectral interference pattern in the presence of active phase locking; fluctuations in phase are reduced to less than 2° over 40 minutes.

In Chapter 3 we characterised photon counters based on mode multiplexing by considering the effect of binned counting on the recorded statistics as well as the role of loss. We introduced a conditional probability matrix **C** and a loss matrix **L** which relate the distribution of counts to that of incoming photons for a given input state detected with a mode multiplexer. Both matrices are device-dependent: **C** is determined by the specific design that realises the multiplexing, while **L** is a function of the detection efficiency η. In this chapter we shall apply the Klyshko calibration method [61] to estimate η_{A} and η_{B} (see Chapter 2, Section 2.3).

Our photon-number-resolving detectors are based on temporal multiplexing, as illustrated in Fig. 4.13. A two-stage time-multiplexed detector consists of two cascaded Mach-Zehnder fibre interferometers that split an incoming signal over two spatial modes and four distinct time bins; the resulting time-resolved clicks are recorded by four APDs, two for each TMD. Given that each mode multiplexer can discriminate up to eight incoming particles, we conveniently visualise the collected data as 9×9 matrices (as already shown in Fig. 4.7 and Fig. 4.9). The specific design of the

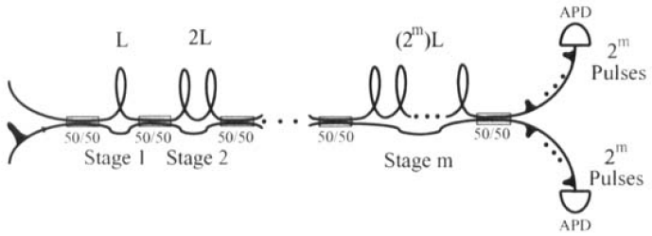

Figure 4.13 The TMDs in our setup are realised as follows: the first balanced fibre beam splitter splits an incoming signal over two distinct spatial modes; a loop of fibre subsequently delays the photons in one of the two modes. The time delay due to a fibre loop must be longer than the dead time of the APDs in use (see Chapter 2, Section 2.3); in our case, the length of a single loop corresponds to a delay of about 100 ns. Additional fibre BSs and loops of fibre increase the maximum resolution of the device: our detectors are characterised by $m = 2$, hence we can resolve up to eight incoming particles (as each APD detects four temporal modes). However, we remark that a larger number of stages limits the response time of the detector: for a two-stage device such as ours, the repetition rate of the incoming signal cannot exceed 2.5 MHz [65]. Image reproduced from [65].

TMDs has a significant impact on the accessible range of detection efficiencies: for example, the splicings needed to produce the fibre loops and realise the temporal multiplexing are bound to introduce additional losses.

4.2 Data analysis and modelling

In this section we present the results of our direct observation of coherent oscillations in the joint counting statistics $\{P(n_{\mathrm{A}}, n_{\mathrm{B}})\}$ for a split single-photon state and the squeezed vacuum. We restrict our study to $n_{\mathrm{A}}, n_{\mathrm{B}} = 0, 1, 2$ as the brightness of our parametric downconversion source is such that higher photon-number contributions are negligible.

In preparation for a data acquisition, the HWP in the LO path preceding the recombination PBS is set so as to split the reference beam equally between the two

output modes. For the polarising beam splitters of the WFH detectors we have that $t = r = 1/\sqrt{2}$: this balanced condition (along with an appropriate setting of the LO power control) guarantees a mean photon number in the LO comparable to that of the PDC signal. As we pointed out in the previous section, the data acquisitions for the SSPS and the TMSS differ by two main aspects: the definition of coincidence counts and the use of active phase locking. The latter is only necessary for the two-mode squeezed vacuum state. All counts and coincidences are time-gated by a trigger from the femtosecond laser, but when we observe the split single photon we also herald on one downcoversion mode (see paragraph on the PDC source). The HWP in each GPR is motorised and can be programmed to scan a user-defined angular range with a given step size, holding each setting for a specified time interval. Additionally, for every acquisition we record 'PDC only' and 'LO only' data by blocking either beam (and with the interference PBSs fully transmitting the detected field): this information is necessary to estimate the experimental detection efficiencies and the coherent-state intensities. As previously noted for the HOMI curves, none of the data presented in this chapter is corrected for background noise.

As the very first step in our investigation, we carry out a qualitative test on the non-classical nature of the phase-dependent behaviour that interests us [26]. We probe both considered classes of quantum states with our WFH detectors and measure $P(n_{\mathrm{A}}, n_{\mathrm{B}})$ for $n_{\mathrm{A}} = n_{\mathrm{B}} = 1$ as we scan the relative LO phase. Subsequently, we block the signal path and record again $P(1, 1)$ for the same range of values of the LO phase shift. We should then observe two effects: first, the coincidence rate oscillates as a function of the LO phase when the signal interferes with the weak

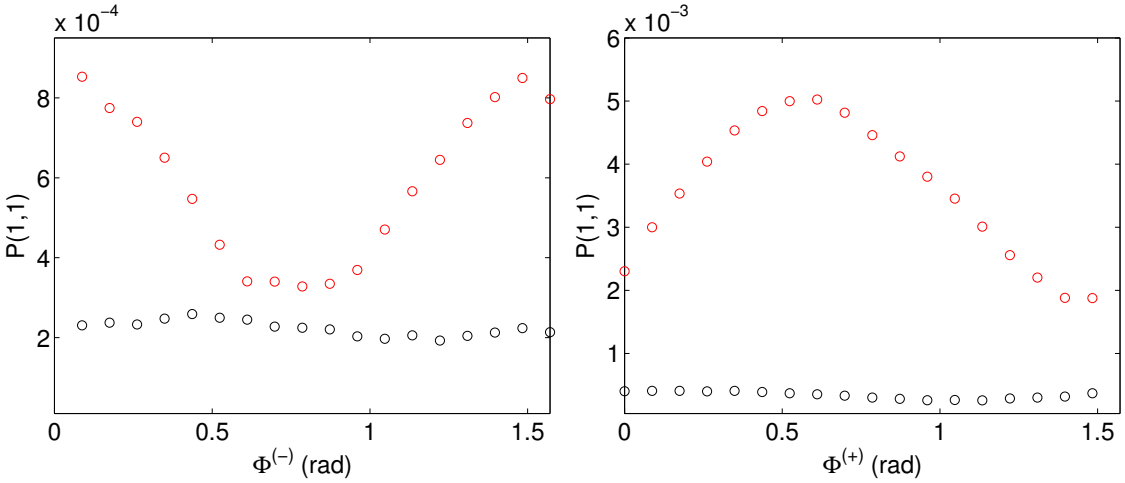

Figure 4.14 We plot the three-fold coincidence counts as a function of the LO phase shift for the SSPS (left) and the TMSS (right). We have that $\Phi^{(\pm)} = \phi^{(\pm)}/4 = (\phi_{\rm A} \pm \phi_{\rm B})/4$ where $\phi_{\rm A}$, $\phi_{\rm B}$ are the phases of the coherent fields, and the factor of four determines the conversion between physical shift $\phi^{(\pm)}$ and HWP setting $\Phi^{(\pm)}$. Red data points are obtained by interfering the two-mode signal with the LOs; black data points correspond to the case where the signal is blocked and only the classical probes reach the detectors. In the latter scenario, we observe no relevant oscillations. For both input states, the red curves are characterised by $V \simeq 0.43$. While this value lies within the classically accessible region of visibilities for such oscillations, care must be taken in interpreting this result in the same way as one would do for experiments with standard 'on-off' detectors (see text).

coherent field, while if either input beam (most significantly, the signal) is blocked the phase dependence of $P(1,1)$ essentially disappears. Second, the visibility of the oscillations is such that the same behaviour could not be obtained in the presence of two classical fields.

The outcome of our measurements for the SSPS and the TMSS is shown in Fig. 4.14. In the presence of signal and LO, $P(1,1)$ exhibits a clear phase dependence – a behaviour that disappears almost completely when we only detect the coherent field. However, the visibilities of the recorded oscillations are slightly below 50%: this may cast doubts on the assertion that we are in the presence of a non-classical effect.

The characterisation of our parametric source in terms of the degree of second-order coherence mentioned in the previous section indicates that we indeed produce single photons ($g^{(2)} = 0.39 \pm 0.04$) and the squeezed vacuum (for the reduced output states, $g_{\mathrm{A}}^{(2)} = 1.92 \pm 0.04$ and $g_{\mathrm{B}}^{(2)} = 1.98 \pm 0.04$). We also recall that the experimental distributions of joint counts presented here include undesired contributions – such as background counts[3] – that can be accounted for with further post-processing of the collected data (which is the case in [26], for instance). Further, it is important to stress that the TMDs grant access to photon-number resolution, yet this does not eliminate all detection inaccuracies; in fact, the use of mode multiplexers calls for a specific interpretation of the acquired data given the design of the detectors (as explained in Chapter 3). We thus maintain that the test which we have just presented highlights the presence of oscillations stemming from the non-classical interference between signal and reference beam. We will comment further on the observed visibilities later in this section.

While we do not include factors such as background noise in our data analysis, we want our theoretical models to account for imperfections that are specific to our experimental realisation. Fig. 4.10 illustrates a typical calibration curve for a GPR, recording counts from the local oscillator only. What is the effect of imperfect phase rotators on the joint counting statistics? To investigate this aspect we acquire click counting statistics coming from the signal and the coherent fields; we then trace over one output mode to obtain marginal distributions of counts (that is, counting

[3]We record up to 100 counts/s from background noise (depending on the value of P_{UV}), and less than one coincident detection event per second. Therefore, the most significant contribution of dark counts to the joint counting statistics is likely to come from false coincidences where one photon is genuine signal and the other belongs to background noise.

statistics for single-mode output states). These quantities are indeed expected to be independent of the relative LO phase [22, 84]. In Fig. 4.15 we compare the

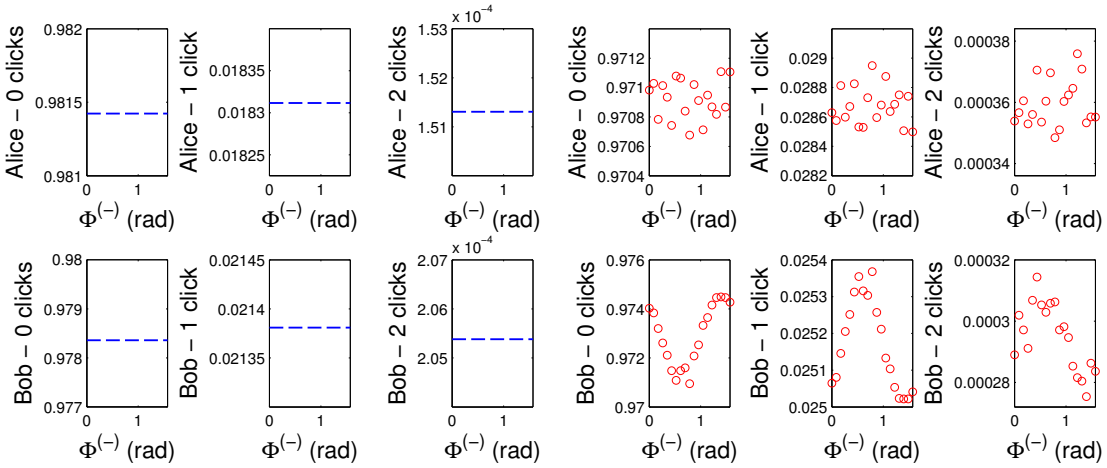

Figure 4.15 We show the theoretical marginal distributions for the SSPS (left) along with the analogous experimental distributions of counts (right) as one GPR controls the LO phase shift (here in Bob's output mode). Similar results are obtained for the squeezed vacuum. We see that the predicted behaviour is phase-independent. By contrast, the experimental data reveals oscillations in the counts recorded by Bob's TMD. The comparison between the experimental marginals and the calibration curve for a GPR shows that the respective visibilities for the '1-click' and '2-click' terms are compatible; this suggests that an imperfect phase rotator can be the cause of the observed spurious modulation of counts.

experimental marginal distributions to the theoretical predictions. We observe that the counting probabilities on the channel where the GPR is active do not remain constant as we change the phase shift. Interestingly, the visibilities of these undesired oscillations are compatible with those observed in the calibration of a GPR (see caption of Fig. 4.10). This suggests that imperfections in the individual wave plates, a slightly off-axis rotation of the motorised HWP in the GPR and/or calibration inaccuracies may be responsible for a modulation of the reflectivity of the PBSs in our WFH detectors. We shall account for this effect in the expression for the

reflection coefficient r of the interference PBS in the arm where the GPR is active. Specifically, we write $r(\Phi^{(\pm)}) = r_0\sqrt{1 + v\cos(4\Phi^{(\pm)} + \phi_0)}$: $r_0 = 1/\sqrt{2}$ is the ideal value, $\Phi^{(\pm)}$ is the setting of the half-wave plate in the phase rotator and ϕ_0 is an offset angle. We expect the modulation depth v to be of the order of 0.1, given the observed deviations from the perfect case.

From now on, we shall treat the two considered classes of quantum states separately as we develop two distinct models to describe the experimental data.

4.2.1 Non-classical coherence in a split single-photon state

We are interested in a theoretical description for the behaviour of our experimental split single-photon state probed via WFH detection. The model should rely on as few parameters as possible and include observed imperfections such as the modulation of the WFH reflectivities. If we focus on the counting statistics, there are two approaches that we can follow.

The first option refers back to the results presented in Chapter 3 (see Section 3.2): if we know the expression for the theoretical output state, we can compute the elements $\{F(m, m')\}$ of the photon statistics matrix (see Eq.(3.25)) and apply

$$\mathbf{P} = \mathbf{C}_{\mathrm{A}} \cdot \mathbf{L}(\eta_{\mathrm{A}}) \cdot \mathbf{F} \cdot \mathbf{L}(\eta_{\mathrm{B}})^{\mathrm{T}} \cdot \mathbf{C}_{\mathrm{B}}^{\mathrm{T}}$$

to determine the expected $\mathbf{P}$ matrix.

The second approach appears more convoluted, but it is valuable to us as it takes advantage of previous work on weak-field homodyne detection carried out in the

group. Given an input state $\hat{\rho}$, it is possible to write the detection probability for the outcome j of a measurement on the system described by $\hat{\rho}$ as

$$p_j = \mathrm{Tr}[\hat{O}_j \hat{\rho}]\,,$$

where $\hat{O}_j$ is the Hermitian operator associated with the considered measurement. Interestingly, this formula is at the core of two well-known methods in quantum optics: state and detector tomography. The former aims at reconstructing an unknown quantum state $\hat{\rho}$ through application of the above relation for a tomographically complete set of measurements, i.e. a set that spans the space of the unknown density matrix. The latter allows for the characterisation of a detector in terms of its positive operator-valued measure (POVM). This means that we now wish to determine the set of operators $\{\hat{O}_j\}$: this reconstruction relies on a set of reference states $\{\hat{\rho}_j\}$, $j = 1, ..., d$, where d is the number of possible outcomes for a given measurement and is thus detector-specific. In 2011 previous members of the group successfully performed the full tomographic reconstruction of our time-multiplexed detectors in terms of their POVM elements [86]. This characterisation of our mode multiplexers complements well the investigation carried out in this section, as we shall explain shortly.

We can express the generic element of the counting statistics matrix as

$$P(n_\mathrm{A}, n_\mathrm{B}) = \mathrm{Tr}[\hat{O}_{n_\mathrm{A}, n_\mathrm{B}} \hat{\varrho}]\,, \tag{4.1}$$

where $\hat{\varrho}$ is the density operator for the theoretical two-mode input state – for example, the SSPS – and $\hat{O}_{n_\mathrm{A},n_\mathrm{B}}$ is the tensor product of operators $\hat{O}_{n_\mathrm{A}}$ and $\hat{O}_{n_\mathrm{B}}$, each of which describes a measurement performed by one of our TMDs. Detector tomography grants us access to the set of measurement operations $\{\hat{O}_{n_\mathrm{A},n_\mathrm{B}}\}$; if $\hat{\varrho}$ is known, we can apply Eq.(4.1) to reconstruct the theoretical joint counting statistics matrix $\mathbf{P}$ for the considered signal. A pure split single-photon state reads

$$|\Psi\rangle_\mathrm{SSPS} = \frac{1}{\sqrt{2}}\big(|0\rangle_\mathrm{A}|1\rangle_\mathrm{B} + |1\rangle_\mathrm{A}|0\rangle_\mathrm{B}\big), \tag{4.2}$$

hence $\hat{\varrho}_\mathrm{SSPS} = |\Psi\rangle_\mathrm{SSPS}\langle\Psi|$. We shall thus refer to Eq.(4.1) to compute the counting statistics matrix for the SSPS.

Schematically, our data analysis proceeds as follows:

1. We determine the experimental detection efficiencies thanks to the 'PDC only' data. If $\mathbf{P}_\mathrm{PDC}$ is the matrix associated with the click counting statistics, we compute $\mathbf{F}_\mathrm{PDC}^{\{\eta_\mathrm{A},\eta_\mathrm{B}\}} = \mathbf{C}_\mathrm{A}^{-1} \cdot \mathbf{P}_\mathrm{PDC} \cdot (\mathbf{C}_\mathrm{B}^\mathrm{T})^{-1}$ to obtain $\eta_\mathrm{A} = 2\,F_\mathrm{PDC}^{\{\eta_\mathrm{A},\eta_\mathrm{B}\}}(1,0)$ and $\eta_\mathrm{B} = 2\,F_\mathrm{PDC}^{\{\eta_\mathrm{A},\eta_\mathrm{B}\}}(0,1)$.
2. The experimental coherent-state amplitudes are a function of the detection efficiencies. Given the matrix of 'LO only' counts, we find $\mathbf{F}_\mathrm{LO}^{\{\eta_\mathrm{A},\eta_\mathrm{B}\}}$, which is analogous to $\mathbf{F}_\mathrm{PDC}^{\{\eta_\mathrm{A},\eta_\mathrm{B}\}}$. This allows us to compute

$$\begin{aligned} |\alpha_\mathrm{A}| &= \sqrt{F_\mathrm{LO}^{\{\eta_\mathrm{A},\eta_\mathrm{B}\}}(1,0)/(F_\mathrm{LO}^{\{\eta_\mathrm{A},\eta_\mathrm{B}\}}(0,0)\cdot\eta_\mathrm{A})}\,, \\ |\alpha_\mathrm{B}| &= \sqrt{F_\mathrm{LO}^{\{\eta_\mathrm{A},\eta_\mathrm{B}\}}(0,1)/(F_\mathrm{LO}^{\{\eta_\mathrm{A},\eta_\mathrm{B}\}}(0,0)\cdot\eta_\mathrm{B})}\,. \end{aligned} \tag{4.3}$$

The efficiencies of detection and the coherent-state amplitudes are required for the estimation of the POVM elements of our TMDs.

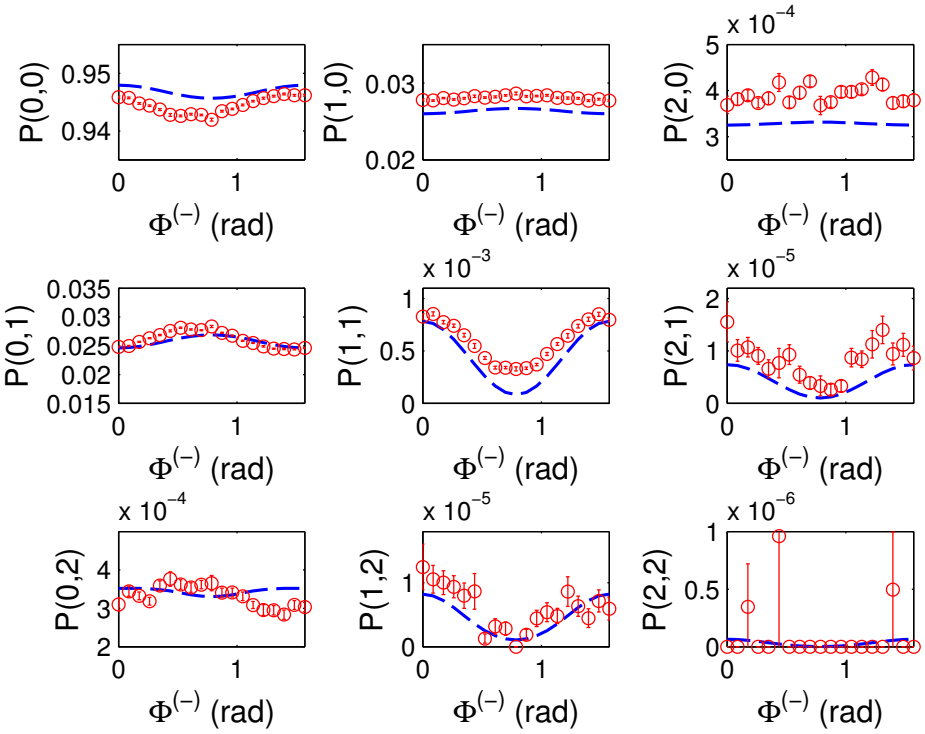

Figure 4.16 We show the correlations between the responses of two WFH detectors as a function of the relative LO phase $\Phi^{(-)} = \phi^{(-)}/4$ (see text). We recall that $P(n_{\rm A}, n_{\rm B})$ indicates the joint probability of counting $n_{\rm A}$ photons with Alice's TMD and $n_{\rm B}$ particles with Bob's detector. The red dots correspond to experimental data, with uncertainties determined by a Monte Carlo routine under the assumption of a Poissonian distribution for the raw counts. The dashed blue curves represent the predictions from the developed model, which assumes a perfect input state but takes into account non-ideal detection and imperfect GPRs (see text). For the dataset shown here we estimated $\eta_{\rm A} = 0.072$ and $\eta_{\rm B} = 0.064$; this implies $|\alpha_{\rm A}| = 0.510$ and $|\alpha_{\rm B}| = 0.585$ for the amplitudes of the two LOs. As for $r(\Phi^{(-)})$, we set $v = 0.15$ for the modulation depth and $\phi_0 = 0°$ for the offset angle.

In Fig. 4.16 we present the experimental joint counting probabilities for the SSPS, together with the theoretical matrix elements $\{P(n_{\rm A}, n_{\rm B})\}$ computed from the model that we have just discussed. The experimental curves show oscillations in the coincidence counts: these are evident in the $P(1,1)$, $P(2,1)$ and $P(1,2)$ terms,

as also predicted by the theory. The striking aspect about the observed behaviour is the fact that non-classical oscillations are displayed by terms $P(n_{\mathrm{A}}, n_{\mathrm{B}})$ for which $n_{\mathrm{A}} + n_{\mathrm{B}} > 1$ although they are determined by the coherence between the terms $|0\rangle_{\mathrm{A}}|1\rangle_{\mathrm{B}}$ and $|1\rangle_{\mathrm{A}}|0\rangle_{\mathrm{B}}$ (see Eq.(4.2)) – terms that do not contain more than one photon each. Consequently, any additional detected particles must come from the local oscillators – yet it is the SSPS that is responsible for the behaviour of the joint counting probabilities.

There is good qualitative agreement between our data and the theoretical predictions: most experimental features are captured by the model. Nevertheless, the terms showing more evident discrepancies urge us to refine the description that we have just presented. For instance, the experimentally determined value of $g^{(2)}$ suggests that the generated single photons are affected by some degree of mixedness. We take into account imperfect single-photon generation in the form of contributions from the vacuum as well as from a higher-order term coming from the downconversion process. We thus rewrite

$$\hat{\varrho}_{\mathrm{SSPS}} = w_0|0\rangle\langle 0| + w_1|1\rangle\langle 1| + (1 - w_0 - w_1)|2\rangle\langle 2|\,. \tag{4.4}$$

This state still generates an entangled resource when split at a symmetric beam splitter. However, the counting statistics are now affected by additional terms in a way determined by the weights w_0 and w_1. These coefficients, along with the detection efficiencies η_{A} and η_{B}, are the key parameters in our revised model. In order to estimate the weights in Eq.(4.4) from the data we refer again to Eq.(3.9). As

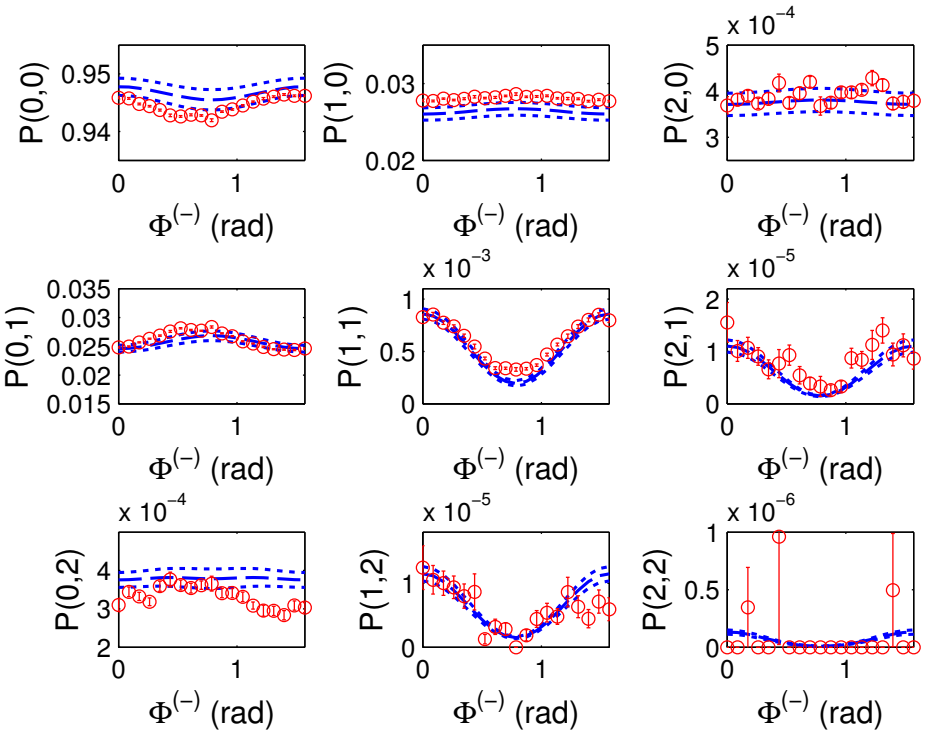

Figure 4.17 We compare the measured joint counting statistics (red dots) with theoretical curves given by a revised model that takes into account non-ideal single-photon production in addition to the previously considered imperfections. The dashed curves correspond to an input state with the experimentally determined weights w_0=0.161 and w_1=0.669. The uncertainties σ_0=0.011 on w_0 and σ_1=0.029 on w_1 are estimated by a Monte Carlo routine; the dotted curves show the results given by the theoretical model with $(w_0 - \sigma_0, w_1 - \sigma_1)$ and $(w_0 + \sigma_0, w_1 + \sigma_1)$, respectively. The remaining parameters are unchanged with respect to Fig. 4.16.

discussed in the previous chapter, if the conditional probability matrices are known and so are $\mathbf{L}(\eta_A)$ and $\mathbf{L}(\eta_B)$, then we can invert Eq.(3.9) to find $\mathbf{F}_{PDC}$ from $\mathbf{P}_{PDC}$ and hence determine w_0 and w_1. The analysis carried out in Chapter 3 revealed that such inversion can easily become unreliable; consequently, we constrain it by requiring that the photon statistics matrix $\mathbf{F}_{PDC}$ is positive semidefinite.

Fig. 4.17 displays the outcome of the revised model. The agreement between data and theoretical predictions has visibly improved for some terms; the residual dis-

crepancies may be attributed to variations of the laser power, given that a complete data acquisition for the SSPS could last a few hours.

4.2.2 Non-classical coherence in a two-mode squeezed vacuum state

The investigation of the squeezed vacuum proceeds in an analogous way. We recall the expression for an ideal TMSS:

$$|\Psi\rangle_{\mathrm{TMSS}} = \sqrt{1-|\lambda|^2}\sum_{n=0}^{+\infty}\lambda^n|n\rangle_{\mathrm{A}}|n\rangle_{\mathrm{B}}\,. \tag{4.5}$$

Once more, the starting point for our theoretical description of the experiment is Eq.(4.1). The relevant parameters for this model are the detection efficiencies and the real squeezing parameter $|\lambda|$. We estimate the latter from the photon statistics matrix $\mathbf{F}_{\mathrm{PDC}}$, which we reconstruct through inversion of Eq.(3.9) (with the constraint discussed for the SSPS). Eq.(4.3) is still valid for the coherent-state amplitudes. To calculate the detection efficiencies we apply the Klyshko calibration method (see Chapter 2, Section 2.3) to find

$$\eta_{\mathrm{A}} = \frac{F_{\mathrm{PDC}}^{\{\eta_{\mathrm{A}},\eta_{\mathrm{B}}\}}(1,1)}{F_{\mathrm{PDC}}^{\{\eta_{\mathrm{A}},\eta_{\mathrm{B}}\}}(0,1)}\,, \quad \eta_{\mathrm{B}} = \frac{F_{\mathrm{PDC}}^{\{\eta_{\mathrm{A}},\eta_{\mathrm{B}}\}}(1,1)}{F_{\mathrm{PDC}}^{\{\eta_{\mathrm{A}},\eta_{\mathrm{B}}\}}(1,0)}\,, \tag{4.6}$$

where $F_{\mathrm{PDC}}^{\{\eta_{\mathrm{A}},\eta_{\mathrm{B}}\}}(0,1)$ corresponds to one photon in Bob's detection mode.

The experimental joint counting probabilities for the TMSS are shown in Fig. 4.18, along with the predictions from the model. Loss is included in our analysis by con-

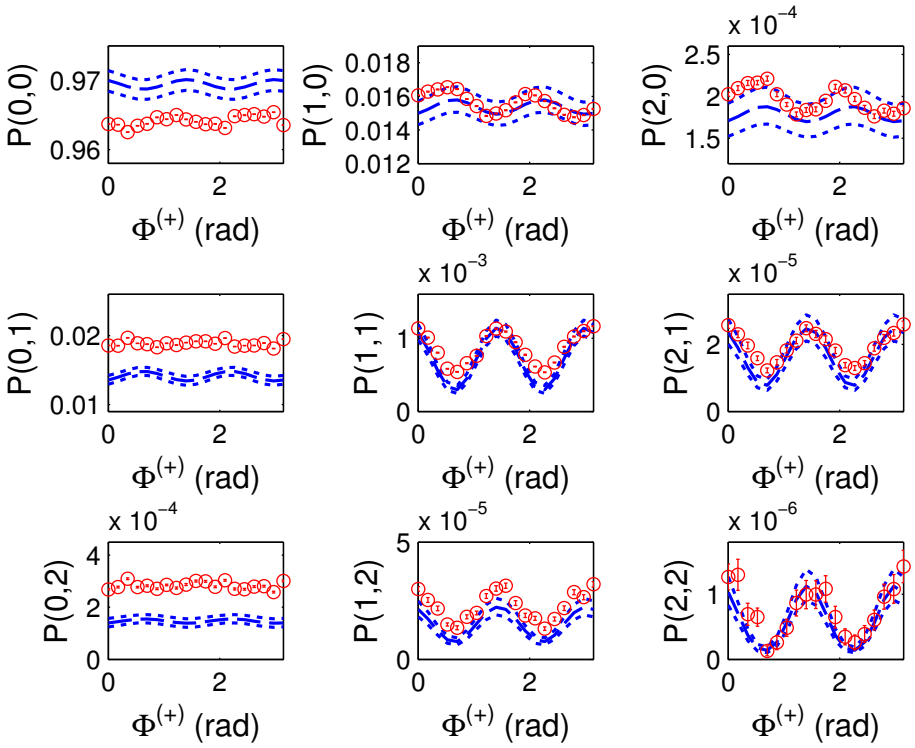

Figure 4.18 We show the correlations between the responses of two WFH detectors as a function of the phase sum $\Phi^{(+)}$ (we recall that $\Phi^{(+)}$ is determined by the setting of the HWP in the active GPR – see text). The red dots correspond to experimental data points, and we run a Monte Carlo routine to compute the error bars (under the assumption of a Poissonian distribution for the raw counts). The blue theoretical curves are obtained from a model that takes into account lossy detection and imperfect GPRs. The dashed curves correspond to an input state with the experimentally determined squeezing parameter $|\lambda| = 0.295$; the uncertainty $\sigma = 0.016$ on $|\lambda|$ is estimated by a Monte Carlo simulation. The additional dotted blue curves show the predicted behaviours for $|\lambda| \pm \sigma$. The experimental detection efficiencies associated with this dataset are $\eta_{\rm A} = 0.132$ and $\eta_{\rm B} = 0.155$, which implies $|\alpha_{\rm A}| = 0.365$ and $|\alpha_{\rm B}| = 0.347$ for the coherent-state amplitudes. In the function $r(\Phi^{(+)})$ (which describes the modulation of the reflectivity in the arm where the GPR is active) we set $v = 0.1$ for the modulation depth and $\phi_0 = 45°$.

sidering the experimentally determined efficiencies $\eta_{\rm A}$ and $\eta_{\rm B}$; we also take into account the modulation of the reflectivities that characterise the PBSs in our WFH detectors. It is interesting to observe that the relevant terms in Fig. 4.18, i.e. those displaying coherent oscillations, show a good agreement with the model despite our

minimal assumptions. On the other hand, the terms characterised by $n_{\mathrm{A}} = 0$ (the first column in the 'matrix' of plots) exhibit rather evident discrepancies in the levels of detected and predicted click counts.

As we did for the split single photon, we refine the model for the TMSS by dropping the hypothesis of a pure input state. We thus introduce a more realistic expression for the experimental squeezed vacuum:

$$\hat{\varrho}_{\mathrm{TMSS}} = (1 - p_{\mathrm{A}} - p_{\mathrm{B}})|\Psi\rangle_{\mathrm{TMSS}}\langle\Psi| + p_{\mathrm{A}}|1,0\rangle\langle 1,0| + p_{\mathrm{B}}|0,1\rangle\langle 0,1|\,. \tag{4.7}$$

The terms $p_{\mathrm{A}}|1,0\rangle\langle 1,0|$ and $p_{\mathrm{B}}|0,1\rangle\langle 0,1|$ represent a first-order approximation of added noise which superposes to the original signal coming from the pure state $|\Psi\rangle_{\mathrm{TMSS}}\langle\Psi|$. The validity of such modification to the previous description is supported by the experimental values of $g^{(2)}$ for the PDC source. Indeed, we recall the relation between the degree of second-order coherence and the Schmidt number K for a squeezer: we have that $K = 1/(g^{(2)} - 1)$ (see Eq.(2.17)). In the ideal case, $g^{(2)} = 2$ (as we trace over one output mode to consider the photon statistics for the other mode) hence $K = 1$: the only active frequency mode in the observed state is the one we detect. In this sense, we see that a deviation from the ideal value for $g^{(2)}$ indicates the presence of undesired frequency modes in the produced two-mode squeezed state.

In the case of the SSPS we estimated the weights w_0 and w_1 in $\hat{\varrho}_{\mathrm{SSPS}}$ from the data. Here we deduce physically reasonable values for the coefficients p_{A} and p_{B} in Eq.(4.7) by direct inspection of the experimental and theoretical plots, and particularly of

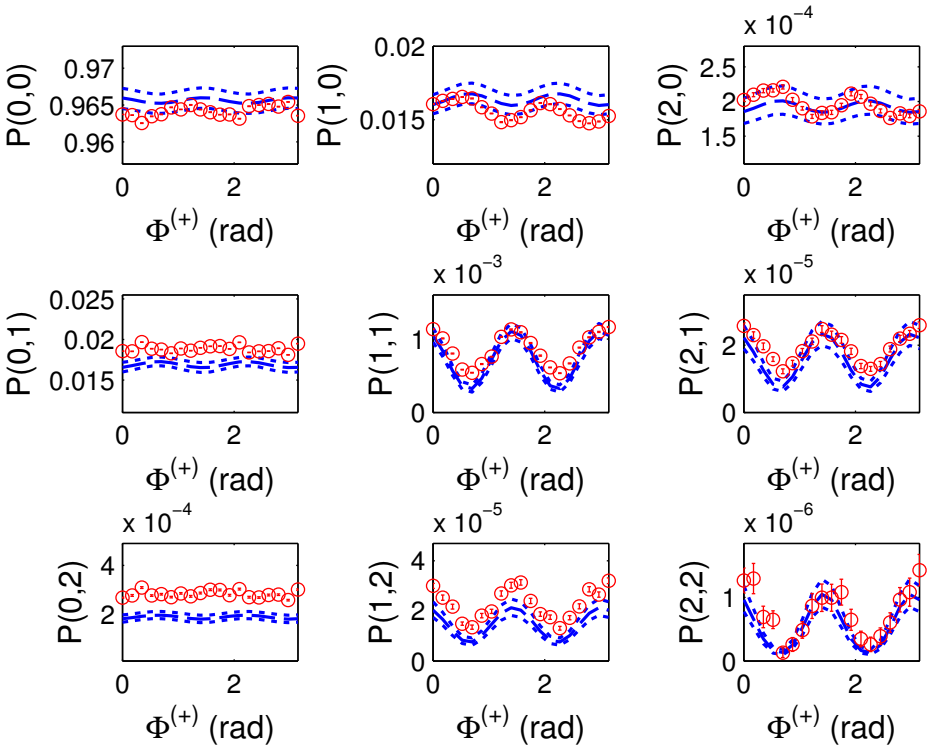

Figure 4.19 We compare the experimental joint counting statistics (red dots) with theoretical curves given by a revised model that takes into account thermal noise affecting the ideal squeezed vacuum in addition to the previously considered imperfections. The dashed curves correspond to an input state with the experimentally determined squeezing parameter $|\lambda| = 0.295$ and weights $p_{\mathrm{A}} = 0.02$ and $p_{\mathrm{B}} = 0.05$ for the noise terms. The uncertainty $\sigma = 0.016$ on $|\lambda|$ is estimated by a Monte Carlo simulation; the dotted blue curves show the predicted behaviours for $|\lambda| \pm \sigma$ (with $p_{\mathrm{A}} = 0.02$ and $p_{\mathrm{B}} = 0.05$). All other parameters are unchanged with respect to Fig. 4.18.

those terms where the disagreement is more pronounced. This empirical procedure led to the values $p_{\mathrm{A}} = 0.02$ and $p_{\mathrm{B}} = 0.05$. We compare the experimental data to the revised model in Fig. 4.19: with the addition of thermal noise to the pure input state, we observe an improved agreement between data and theoretical predictions for most considered terms in the joint counting statistics matrix.

It is interesting to highlight the role of the two major aspects included in the theoretical descriptions that we have just discussed, namely loss (through the exper-

imentally determined efficiencies) and imperfect state generation. As illustrated in Fig. 4.20, the effect of lossy detection is well-captured by considering three distinct scenarios corresponding to different values of η_A and η_B: poor efficiency of detection appears to mainly affect the visibility of the non-classical oscillations. Interestingly,

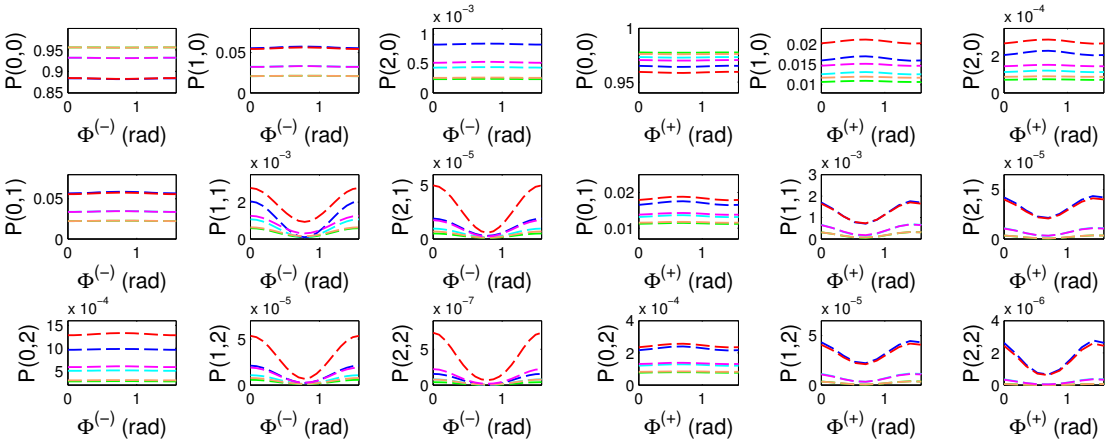

Figure 4.20 We show the array of considered click counting probabilities for the SSPS (left) and the TMSS (right) as a function of the relevant LO phase shift. Blue, cyan and green curves correspond to ideal, pure initial states (that is, $w_1 = 1$ for the SSPS and $p_A = p_B = 0$ for the TMSS) measured with increasingly lossy detectors (under the assumption $\eta_A = \eta_B$) – $\eta = 0.2$, $\eta = 0.1$ and $\eta = 0.05$, respectively. Red, magenta and copper curves correspond to the same choice of detection efficiencies; however, we drop the assumption of pure input states and use the values of w_0, w_1 (for the SSPS) and of p_A, p_B (for the TMSS) given in the text.

this conclusion holds for both considered expressions for the initial states of the SSPS and the TMSS: while three curves (blue, cyan and green) correspond to ideal input states, the remaining plots are given by the revised expressions for $|\Psi\rangle_{\mathrm{SSPS}}$ and $|\Psi\rangle_{\mathrm{TMSS}}$. For the split single photon, the form of the initial state has a greater impact on the counting statistics for $\eta > 0.1$ (blue and red curves) than for smaller efficiencies. Particularly, we notice an effect on the visibility of the oscillating terms: for instance, $P(1,1)$ exhibits almost unit visibility with a pure input state, while V

drop slightly below 50% if $|\Psi\rangle_{\mathrm{SSPS}}$ is mixed. On the other hand, the visibility of terms such as $P(2,1)$ seems to be fictitiously enhanced when $|\Psi\rangle_{\mathrm{SSPS}}$ is not pure. As for the squeezed vacuum, the most evident differences between the two assumptions on the form of $|\Psi\rangle_{\mathrm{TMSS}}$ appear for the terms where $n_{\mathrm{A}} = 0$ or $n_{\mathrm{B}} = 0$. Moreover, we notice that $P(2,2)$ has a considerably higher visibility than $P(1,1)$, for which $V < 0.5$. In the light of Fig. 4.20, the visibilities observed in Fig. 4.14 (where we only showed $P(1,1)$ for both states) appear then less anomalous than one might expect from the comparison of our results with similar tests on the non-classicality of the observed oscillations.

Let us close this section with a few general remarks on our data analysis. The models for the SSPS and the TMSS share some common limitations; there are effects that we have not included – such as imperfect mode matching between the probed two-mode state and the classical references. Nonetheless, our theoretical descriptions have the advantage of relying on few assumptions as well as on a limited set of parameters, most of which are directly estimated from the collected data. Each model captures the experimental features for most terms in the considered joint counting statistics matrix simultaneously. This means that we harness the behaviour of the multi-photon Fock layers in the observed output states with a single description and set of experimentally determined parameters.

4.3 Higher-order Bell tests

In the previous two sections of this chapter we have discussed the experimental demonstration of non-classical correlations across the Fock layers characterising two different classes of two-mode states. This observation of optical coherence was made possible by weak-field homodyne detectors combining photon-number resolution and phase sensitivity. Standard Bell tests performed with detection schemes similar to ours [26, 84] suggest that we ask whether we can view this instance of non-classical optical coherence as a quantum resource and, if so, establish what the required conditions are.

Let us consider the familiar layout illustrated in Fig. 4.21: we interfere a two-mode squeezed vacuum state with two local oscillators and detect the resulting output state with four PNRDs. Can we perform projective measurements with WFH A and WFH B and violate a Bell-type inequality with a Gaussian resource – the TMSS – probed with non-Gaussian detectors? The ability to discriminate the number of detected particles represents both a novelty and an immediate problem: the outcomes of our measurements are not dichotomic anymore, i.e. we record more complex information than just 'click' or 'no click'. A few published studies report on extensions of Bell's results to multi-chotomic outcomes; here we follow the approach given in [87]. Specifically, we shall apply the Collins-Gisin-Linden-Massar-Popescu (CGLMP) inequalities, valid for arbitrary dimensions of the set of measurement outcomes, to a pure two-mode squeezed vacuum state probed with two ideal WFH detectors. We stress the two assumptions made here: the purity of the signal, and a

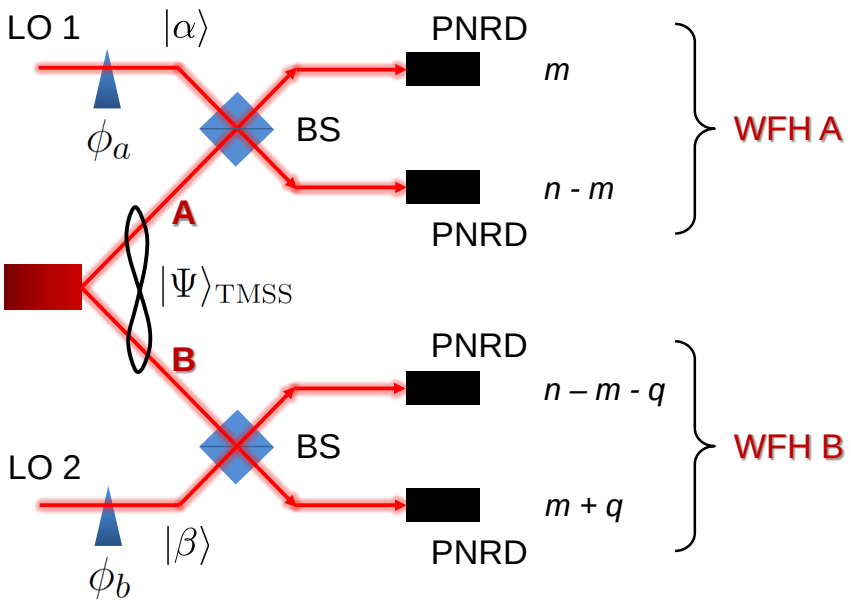

Figure 4.21 This is the ideal layout for our investigation of the non-local character of Gaussian entanglement via WFH detection. The two modes of the squeezed vacuum state, an archetypal Gaussian resource, are interfered with weak coherent fields to produce a four-mode output state. Photon-number-resolving detectors monitor all outputs (that is, we do not discard the reflected output modes here). If we fix the number n of photons detected by each WFH detector, we can label the recorded detection events according to how n particles distribute themselves between the transmitted and reflected output modes: namely, these are the quantities m, $n-m$ (WFH A) and $n-m-q$, $m+q$ (WFH B) shown in the diagram.

detection system excluding loss as well as any other source of imperfection affecting the measurement process.

We begin our theoretical investigation by fixing the number n of detected photons on each WFH, distributed among the transmitted and reflected output modes as indicated in Fig. 4.21. We restrict our study to $n^{\max} = 2$, hence each projective measurement can yield one value within the set $\{0,1,2\}$ – or, equivalently, within $\{0,1,-1\}$ (the two sets being congruent modulo 3). In other terms, our local subsystems (A and B, see Fig. 4.21) have dimension $d = n+1 = 3$. The generalisation

to higher photon numbers proceeds in a similar fashion, but the added complexity of the theoretical framework does not contribute significantly to this investigation. Next we consider the quantum state $|\Psi\rangle_{\text{TMSS}}$, distributed across modes $\hat{a}_{\text{s}}^{\dagger}$ and $\hat{a}_{\text{i}}^{\dagger}$, and the local oscillators $|\alpha\rangle$ and $|\beta\rangle$ associated with modes $\hat{b}_1^{\dagger}$ and $\hat{b}_2^{\dagger}$, respectively. Under the assumption of low numbers of detected photons ($n^{\max} = 2$), we write the initial state as (neglecting the multiplicative factor $\sqrt{1-|\lambda|^2}e^{-|\alpha|^2/2}e^{-|\beta|^2/2}$)

$$|\Psi\rangle_{\text{in}} = \left(\frac{\alpha^2}{2}\frac{\beta^2}{2}(\hat{b}_1^{\dagger})^2(\hat{b}_2^{\dagger})^2 + \frac{\lambda^2}{2}(\hat{a}_{\text{s}}^{\dagger})^2(\hat{a}_{\text{i}}^{\dagger})^2 + \lambda\alpha\beta\,\hat{a}_{\text{s}}^{\dagger}\hat{a}_{\text{i}}^{\dagger}\hat{b}_1^{\dagger}\hat{b}_2^{\dagger}\right)|0\rangle_{\text{s}}|0\rangle_{\text{i}}|0\rangle_1|0\rangle_2\,, \tag{4.8}$$

where $\alpha = |\alpha|e^{\imath\phi_a}$, $\beta = |\beta|e^{\imath\phi_b}$ and $\lambda = |\lambda|e^{\imath\theta}$.

The beam splitter of each weak-field homodyne detector operates the following output-input transformations:

$$\begin{cases} \hat{a}_{\text{s}}^{\dagger} = t_1\hat{d}_1^{\dagger} + r_1^*\hat{e}_1^{\dagger}\,, \\ \hat{b}_1^{\dagger} = r_1\hat{d}_1^{\dagger} - t_1\hat{e}_1^{\dagger} \end{cases} \tag{4.9}$$

for WFH A, and

$$\begin{cases} \hat{a}_{\text{i}}^{\dagger} = t_2\hat{d}_2^{\dagger} + r_2^*\hat{e}_2^{\dagger}\,, \\ \hat{b}_2^{\dagger} = r_2\hat{d}_2^{\dagger} - t_2\hat{e}_2^{\dagger} \end{cases} \tag{4.10}$$

for WFH B.

Here $(\hat{d}_1^{\dagger}, \hat{d}_2^{\dagger})$ and $(\hat{e}_1^{\dagger}, \hat{e}_2^{\dagger})$ are the transmitted and reflected output modes, respectively; the coefficients associated to the BSs are such that $t_{1,2} \in \mathbb{R}$ and $r_{1,2} = -\imath|r_{1,2}|$, with $|r_{1,2}| = \sqrt{1-t_{1,2}^2}$ (see Chapter 2, Section 2.1 for the validity of this choice).

As a consequence, we can express the total output state $|\Psi\rangle_{\text{out}}$ as

$$
\begin{aligned}
|\Psi\rangle_{\text{out}} = &\Big(\frac{\alpha^2\beta^2}{4}r_1^2r_2^2 + \frac{\lambda^2}{2}t_1^2t_2^2 + \lambda\alpha\beta t_1t_2r_1r_2\Big)|2200\rangle + \\
&+ \Big(\frac{\alpha^2\beta^2}{4}t_1^2t_2^2 + \frac{\lambda^2}{2}(r_1^*)^2(r_2^*)^2 + \lambda\alpha\beta t_1t_2r_1^*r_2^*\Big)|0022\rangle + \\
&+ \Big(\frac{\alpha^2\beta^2}{4}r_1^2t_2^2 + \frac{\lambda^2}{2}t_1^2(r_2^*)^2 - \lambda\alpha\beta t_1t_2r_1r_2^*\Big)|2002\rangle + \\
&+ \Big(\frac{\alpha^2\beta^2}{4}t_1^2r_2^2 + \frac{\lambda^2}{2}(r_1^*)^2t_2^2 - \lambda\alpha\beta t_1t_2r_1^*r_2\Big)|0220\rangle + \\
&+ \big[\alpha^2\beta^2t_1t_2r_1r_2 + 2\lambda^2t_1t_2r_1^*r_2^* - \\
&\quad - \lambda\alpha\beta(t_2^2|r_1|^2 - |r_1|^2|r_2|^2 + t_1^2|r_2|^2 - t_1^2t_2^2)\big]|1111\rangle + \\
&+ \Big[-\frac{\alpha^2\beta^2}{2}t_2r_1^2r_2 + \lambda^2t_1^2t_2r_2^* - \lambda\alpha\beta(t_1t_2^2r_1 - t_1r_1|r_2|^2)\Big]|2101\rangle + \\
&+ \Big[-\frac{\alpha^2\beta^2}{2}t_1r_1r_2^2 + \lambda^2t_1t_2^2r_1^* - \lambda\alpha\beta(t_1^2t_2r_2 - t_2|r_1|^2r_2)\Big]|1210\rangle + \\
&+ \Big[-\frac{\alpha^2\beta^2}{2}t_1t_2^2r_1 + \lambda^2t_1r_1^*(r_2^*)^2 + \lambda\alpha\beta(t_1^2t_2r_2^* - t_2|r_1|^2r_2^*)\Big]|1012\rangle + \\
&+ \Big[-\frac{\alpha^2\beta^2}{2}t_1^2t_2r_2 + \lambda^2t_2(r_1^*)^2r_2^* - \lambda\alpha\beta(t_1r_1^*|r_2|^2 - t_1t_2^2r_1^*)\Big]|0121\rangle\,.
\end{aligned}
\tag{4.11}
$$

Throughout this section we shall use the convention $|0000\rangle = |0\rangle_{1\text{t}}|0\rangle_{2\text{t}}|0\rangle_{1\text{r}}|0\rangle_{2\text{r}}$, and similarly for all other four-photon Fock states; 't' and 'r' denote transmitted and reflected output modes, respectively.

To construct Bell inequalities for high-dimensional systems, Collins and collaborators formulate a logical constraint that correlations must satisfy if they can be explained in terms of a local variable theory (see Chapter 1, Section 1.3). Given two parties A and B, we suppose that they can realise two measurements (A_1, A_2) and (B_1, B_2), respectively. Each such measurement has d possible outcomes indicated as $\mathscr{A}_1$, $\mathscr{A}_2$, $\mathscr{B}_1$ and $\mathscr{B}_2$, such that $\mathscr{A}_1, \mathscr{A}_2, \mathscr{B}_1, \mathscr{B}_2 = 0, \ldots, d-1$. In a LVT, we associate a probability p_{jklm} to measurements A_1 and A_2 giving outcomes j and l,

respectively, *and* to measurements B_1 and B_2 producing outputs k and m; p_{jklm} is such that $p_{jklm} \geq 0$ for all j, k, l, m and $\sum_{j,k,l,m} p_{jklm} = 1$. The joint probability $P(\mathscr{A}_1 = j, \mathscr{B}_1 = k)$ can be computed by summing p_{jklm} over l and m; analogous relations hold for other joint measurements. If we consider a specific set of outcomes such that $\mathscr{A}_1 = j$, $\mathscr{A}_2 = l$, $\mathscr{B}_1 = k$ and $\mathscr{B}_2 = m$, we can define [87]

$$\begin{aligned} \mathscr{R} &:= \mathscr{B}_1 - \mathscr{A}_1 = k - j \,, \\ \mathscr{S} &:= \mathscr{A}_2 - \mathscr{B}_1 = l - k \,, \\ \mathscr{T} &:= \mathscr{B}_2 - \mathscr{A}_2 = m - l \,, \\ \mathscr{U} &:= \mathscr{A}_1 - \mathscr{B}_2 = j - m \,. \end{aligned} \tag{4.12}$$

We see that we are free to assign values to $\mathscr{R}$, $\mathscr{S}$ and $\mathscr{T}$ by choosing j, k, l, m. However, this automatically fixes the value of $\mathscr{U}$ to $\mathscr{U} = -(\mathscr{R} + \mathscr{S} + \mathscr{T})$ given that $\mathscr{R} + \mathscr{S} + \mathscr{T} + \mathscr{U} = 0$.

We can rephrase this key result by introducing the quantity

$$I = P(\mathscr{A}_1 = \mathscr{B}_1) + P(\mathscr{B}_1 = \mathscr{A}_2 + 1) + P(\mathscr{A}_2 = \mathscr{B}_2) + P(\mathscr{B}_2 = \mathscr{A}_1) \,. \tag{4.13}$$

The term $P(\mathscr{B}_1 = \mathscr{A}_2 + 1)$ is a special case of a more general quantity that we shall use repeatedly in this section: the probability of measurements A_a and B_b producing outcomes that differ by some integer – 1, in this case – modulo d, that is,

$$P(\mathscr{A}_a = \mathscr{B}_b + k) = \sum_{j=0}^{d-1} P(\mathscr{A}_a = j, \mathscr{B}_b = (j + k) \bmod d) \tag{4.14}$$

with $a, b = 1, 2$ in our case. We recall that d identifies the dimension of the local subsystems, while k can assume both positive and negative integer values.

The constraint expressed by Eq.(4.12) can be reformulated by stating that a LVT precludes all four probabilities in Eq.(4.13) from being non-zero. Any choice of local variables will only satisfy three conditions – for example, $\mathscr{A}_1 = \mathscr{B}_1$, $\mathscr{A}_2 = \mathscr{B}_2$ and $\mathscr{B}_2 = \mathscr{A}_1$. This would imply $j = k$, $l = m$ and $m = j$ so that $j = k = l = m$. However, $P(\mathscr{B}_1 = \mathscr{A}_2 + 1)$ would impose $k = l + 1$, which clearly contradicts the earlier conclusion. Consequently, the following inequalities hold:

$$I^{\mathrm{LVT}} \leq 3\,, \quad I^{\mathrm{QM}} \leq 4\,. \tag{4.15}$$

Further, we generalise Eq.(4.13) to an arbitrary dimension d [87]:

$$\begin{aligned} I_d = \sum_{k=0}^{[d/2]-1} \left(1 - \frac{2k}{d-1}\right) \Big\{ &+ \big[P(\mathscr{A}_1 = \mathscr{B}_1 + k) + P(\mathscr{B}_1 = \mathscr{A}_2 + k + 1) + \\ &+ P(\mathscr{A}_2 = \mathscr{B}_2 + k) + P(\mathscr{B}_2 = \mathscr{A}_1 + k)\big] - \big[P(\mathscr{A}_1 = \mathscr{B}_1 - k - 1) + \\ &+ P(\mathscr{B}_1 = \mathscr{A}_2 - k) + P(\mathscr{A}_2 = \mathscr{B}_2 - k - 1) + P(\mathscr{B}_2 = \mathscr{A}_1 - k - 1)\big] \Big\}\,. \end{aligned} \tag{4.16}$$

In the sum over k, $[\cdot]$ indicates the floor function. If we compare this expression to Eq.(4.13), we see that the generalisation comes as new terms in the summation. It is possible to prove that the inequalities in Eq.(4.15) become

$$I_d^{\mathrm{LVT}} \leq 2\,, \quad I_d^{\mathrm{QM}} \leq 4\,. \tag{4.17}$$

Let us focus on $d = 3$ and justify the classical bound in this special case. We write I_3 as

$$I_3 = [P(\mathscr{A}_1 = \mathscr{B}_1) + P(\mathscr{B}_1 = \mathscr{A}_2 + 1) + P(\mathscr{A}_2 = \mathscr{B}_2) + P(\mathscr{B}_2 = \mathscr{A}_1)] - \\ - [P(\mathscr{A}_1 = \mathscr{B}_1 - 1) + P(\mathscr{B}_1 = \mathscr{A}_2) + P(\mathscr{A}_2 = \mathscr{B}_2 - 1) + P(\mathscr{B}_2 = \mathscr{A}_1 - 1)] , \tag{4.18}$$

given that $[3/2] \equiv 1$. In the presence of non-local correlations (I_3^{QM}), it is possible that all four probabilities with a plus sign are equal to one. By contrast, I_3^{LVT} cannot exceed 2 because of the terms preceded by a minus sign in Eq.(4.18). Indeed, we already know that only three out of the four conditions associated to the probabilities with a plus sign can be simultaneously met: for instance, $\mathscr{A}_1 = \mathscr{B}_1$, $\mathscr{A}_2 = \mathscr{B}_2$ and $\mathscr{B}_2 = \mathscr{A}_1$. Following the notation of Eq.(4.12), this implies once again $j = k = l = m$, which in turn means that $P(\mathscr{B}_1 = \mathscr{A}_2 + 1) = 0$. However, we also have that $P(\mathscr{B}_1 = \mathscr{A}_2) = 1$ because $k = l$, hence the classical bound of 2 for I_3.

How do we tailor Eq.(4.18) to the layout sketched in Fig. 4.21? Every probability in I_3 can be computed as the expectation value of a given Fock state projector on $|\Psi\rangle_{\mathrm{out}}$. Additionally, we recall that $P(\mathscr{A}_1 = \mathscr{B}_1)$ is the probability that outcomes $\mathscr{A}_1$ and $\mathscr{B}_1$ coincide, and that these measurement results correspond to settings A_1 and B_1: in order to make the connection with the physical state $|\Psi\rangle_{\mathrm{out}}$ clearer, we shall indicate these settings by the coherent-state amplitudes α_1 and β_1 (and similarly for

A_2 and B_2). Therefore, we express each term in Eq.(4.18) as follows:

$$\begin{aligned}
P(\mathscr{A}_1 = \mathscr{B}_1) &= \langle \hat{P}_{00} \rangle(\alpha_1, \beta_1) + \langle \hat{P}_{11} \rangle(\alpha_1, \beta_1) + \langle \hat{P}_{22} \rangle(\alpha_1, \beta_1), \\
P(\mathscr{B}_1 = \mathscr{A}_2 + 1) &= \langle \hat{P}_{10} \rangle(\alpha_2, \beta_1) + \langle \hat{P}_{21} \rangle(\alpha_2, \beta_1) + \langle \hat{P}_{02} \rangle(\alpha_2, \beta_1), \\
P(\mathscr{A}_2 = \mathscr{B}_2) &= \langle \hat{P}_{00} \rangle(\alpha_2, \beta_2) + \langle \hat{P}_{11} \rangle(\alpha_2, \beta_2) + \langle \hat{P}_{22} \rangle(\alpha_2, \beta_2), \\
P(\mathscr{B}_2 = \mathscr{A}_1) &= \langle \hat{P}_{00} \rangle(\alpha_1, \beta_2) + \langle \hat{P}_{11} \rangle(\alpha_1, \beta_2) + \langle \hat{P}_{22} \rangle(\alpha_1, \beta_2),
\end{aligned} \tag{4.19}$$

and

$$\begin{aligned}
P(\mathscr{A}_1 = \mathscr{B}_1 - 1) &= \langle \hat{P}_{10} \rangle(\alpha_1, \beta_1) + \langle \hat{P}_{21} \rangle(\alpha_1, \beta_1) + \langle \hat{P}_{02} \rangle(\alpha_1, \beta_1), \\
P(\mathscr{B}_1 = \mathscr{A}_2) &= \langle \hat{P}_{00} \rangle(\alpha_2, \beta_1) + \langle \hat{P}_{11} \rangle(\alpha_2, \beta_1) + \langle \hat{P}_{22} \rangle(\alpha_2, \beta_1), \\
P(\mathscr{A}_2 = \mathscr{B}_2 - 1) &= \langle \hat{P}_{10} \rangle(\alpha_2, \beta_2) + \langle \hat{P}_{21} \rangle(\alpha_2, \beta_2) + \langle \hat{P}_{02} \rangle(\alpha_2, \beta_2), \\
P(\mathscr{B}_2 = \mathscr{A}_1 - 1) &= \langle \hat{P}_{01} \rangle(\alpha_1, \beta_2) + \langle \hat{P}_{12} \rangle(\alpha_1, \beta_2) + \langle \hat{P}_{20} \rangle(\alpha_1, \beta_2)\,.
\end{aligned} \tag{4.20}$$

In Eqn.(4.19) and (4.20) we adopted a convenient short-hand notation for the projectors:

$$\begin{aligned}
&|2200\rangle \longleftrightarrow |00\rangle \to \hat{P}_{00}\,, \qquad |1111\rangle \longleftrightarrow |11\rangle \to \hat{P}_{11}\,, \\
&|0022\rangle \longleftrightarrow |22\rangle \to \hat{P}_{22}\,, \qquad |1210\rangle \longleftrightarrow |10\rangle \to \hat{P}_{10}\,, \\
&|0121\rangle \longleftrightarrow |21\rangle \to \hat{P}_{21}\,, \qquad |2002\rangle \longleftrightarrow |02\rangle \to \hat{P}_{02}\,, \\
&|2101\rangle \longleftrightarrow |01\rangle \to \hat{P}_{01}\,, \qquad |1012\rangle \longleftrightarrow |12\rangle \to \hat{P}_{12}\,, \\
&|0220\rangle \longleftrightarrow |20\rangle \to \hat{P}_{20}\,.
\end{aligned}$$

This convention amounts to retaining the number of detected photons on the two

reflected output modes as the two significant digits for the labels identifying the operators in Eqn.(4.19) and (4.20).

In fact, this choice is more than a convenient notation: it justifies the specific structure of each probability in Eqn.(4.19) and (4.20). As illustrated in Fig. 4.21, we perform four projective measurements on the total state $|\Psi\rangle_{\text{out}}$, one in every output mode. A natural doubt arises: when we consider measurement outcomes $\mathscr{A}_1$ and $\mathscr{A}_2$, for example, to what PNRD of WFH A do we refer? We must answer this question in order to give a meaning to the eight quantities in Eqn.(4.19) and (4.20), and this is precisely what the above convention does: it establishes that, for the purpose of computing I_3, measurement results refer to the outcomes recorded in the reflected output modes. We could have equally chosen to look at the transmitted modes: this would modify Eqn.(4.19) and (4.20), but it would not affect I_3. To clarify this point further, let us calculate explicitly $P(\mathscr{B}_1 = \mathscr{A}_2 + 1)$:

$$
\begin{aligned}
P(\mathscr{B}_1 = \mathscr{A}_2 + 1) \equiv P(\mathscr{A}_2 = \mathscr{B}_1 - 1) = \sum_{j=0}^{2} P(\mathscr{A}_2 = j, \mathscr{B}_1 = (j-1) \bmod 3) = \\
= P(\mathscr{A}_2 = 0, \mathscr{B}_1 = -1 \bmod 3) + P(\mathscr{A}_2 = 1, \mathscr{B}_1 = 0 \bmod 3) + \\
+ P(\mathscr{A}_2 = 2, \mathscr{B}_1 = 1 \bmod 3) = \\
= P(\mathscr{A}_2 = 0, \mathscr{B}_1 = 2) + P(\mathscr{A}_2 = 1, \mathscr{B}_1 = 0) + \\
+ P(\mathscr{A}_2 = 2, \mathscr{B}_1 = 1) = \\
= \langle \hat{P}_{02} \rangle(\alpha_2, \beta_1) + \langle \hat{P}_{10} \rangle(\alpha_2, \beta_1) + \langle \hat{P}_{21} \rangle(\alpha_2, \beta_1) \,,
\end{aligned}
$$

which is exactly the expression that appears in Eq.(4.19).

In Fig. 4.22 we show the behaviour of $\langle \hat{P}_{kk'} \rangle$ for $k = k' = 1$ and $k = k' = 2$ as the phase of one local oscillator is varied. We recall that these expectation values appear in Eq.(4.18) through the detection probabilities expressed in Eqn.(4.19) and (4.20). The most remarkable feature is the presence of two different oscillation periods for the considered four-photon detection probabilities: the phase dependence is determined by the specific Fock layer observed.

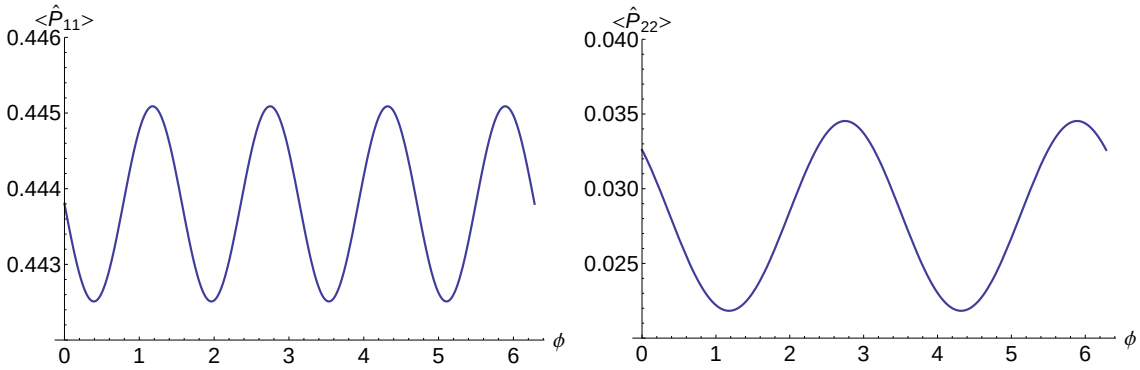

Figure 4.22 We show the expectation values of the projection operators on four-photon states $|1111\rangle$ (left) and $|0022\rangle$ (right). The phase on the horizontal axis can be that of either LO, i.e. ϕ_a or ϕ_b; we assume $\theta = 0$ for the two-mode squeezed state and $\phi_b = \phi_a + \pi/4$, relabelling $\phi_a = \phi$. Values close to those measured in the previous section are assigned to the remaining variables: $|\lambda| = 0.3$ and $|\alpha| = |\beta| = 0.131$ (for unit detection efficiency). We assume balanced beam splitters, hence $t_i = r_j = 1/\sqrt{2}$ for $i, j = 1, 2$. In these plots we also take into account the global factor $(1 - |\lambda|^2)e^{-|\alpha|^2}e^{-|\beta|^2}$ (see the remark preceding the expression for $|\Psi\rangle_{\text{in}}$). We only show two out of the nine considered expectation values as these are representative of the two observed oscillation periods: $\langle \hat{P}_{01} \rangle$, $\langle \hat{P}_{10} \rangle$, $\langle \hat{P}_{12} \rangle$ and $\langle \hat{P}_{21} \rangle$ behave in the same way as $\langle \hat{P}_{11} \rangle$, while $\langle \hat{P}_{00} \rangle$, $\langle \hat{P}_{02} \rangle$ and $\langle \hat{P}_{20} \rangle$ are characterised by the same period as $\langle \hat{P}_{22} \rangle$.

Can we violate the local realistic inequality in Eq.(4.17)? If so, can the violation be maximal and how does this depend on the dimension $d = n + 1$ of the local subsystems? To investigate this aspect, we extend the calculation that led to $|\Psi\rangle_{\text{out}}$ (see Eq. (4.11)) to account for an arbitrary number n of detected photons with each

WFH. Given the initial state (neglecting again a global normalisation factor)

$$|\Psi\rangle_{\rm in}^{n} = \sum_{j=0}^{n} \frac{\tilde{\alpha}^{n-j}\tilde{\beta}^{n-j}}{j![(n-j)!]^2} (\hat{a}_{\rm s}^{\dagger})^{j} (\hat{a}_{\rm i}^{\dagger})^{j} (\hat{b}_{1}^{\dagger})^{n-j} (\hat{b}_{2}^{\dagger})^{n-j} |0\rangle_{\rm s}|0\rangle_{\rm i}|0\rangle_{1}|0\rangle_{2}\,, \tag{4.21}$$

we apply the beam splitter transformations introduced earlier to obtain the following expression for the total output state:

$$\begin{aligned} |\Psi\rangle_{\rm out}^{n} = & \sum_{j=0}^{n} \frac{1}{2^n} \frac{\tilde{\alpha}^{n-j}\tilde{\beta}^{n-j}}{j![(n-j)!]^2} \sum_{k=0}^{j} \sum_{k'=0}^{j} \sum_{l=0}^{n-j} \sum_{l'=0}^{n-j} \binom{j}{k} \binom{j}{k'} \cdot \\ & \cdot \binom{n-j}{l} \binom{n-j}{l'} (-1)^{l+l'} (\hat{d}_{1}^{\dagger})^{n-k-l} (\hat{e}_{1}^{\dagger})^{k+l}\,. \\ & \cdot (\hat{d}_{2}^{\dagger})^{n-k'-l'} (\hat{e}_{2}^{\dagger})^{k'+l'} |0\rangle_{\rm s}|0\rangle_{\rm i}|0\rangle_{1}|0\rangle_{2}\,. \end{aligned} \tag{4.22}$$

We note that we have introduced rescaled coherent-state (complex) amplitudes, defined as $\tilde{\alpha} = \alpha/\sqrt{\lambda}$, $\tilde{\beta} = \beta/\sqrt{\lambda}$. This choice is advantageous in that it effectively lowers the number of parameters by two (namely, it rules out $|\lambda|$ and θ) without compromising the generality of the above formula. To find the probabilities $\{P(\mathscr{A}_a = \mathscr{B}_b + q)\}$ for $q = 0, \ldots, n$, we must calculate the amplitudes $\{\langle m|\langle m+q|\langle n-m|\langle n-m-q|\Psi\rangle_{\rm out}^{n}\}$ first. We then sum the quantities given by the square moduli of the probability amplitudes over all possible values of m (accounting for the appropriate normalisation) to find the desired probabilities (which are a function of q). This is the information we need to compute I_n (see Eq.(4.16) with $n = d-1$ and q in place of k).

We adopt a similar approach to that discussed in Chapter 3 and carry out a numerical optimisation to find the set of parameters (real coherent-state amplitudes and

phases) that determine the highest violation of generalised Bell inequalities based on I_n for values of n ranging from 2 to 8. Our numerical results are illustrated in

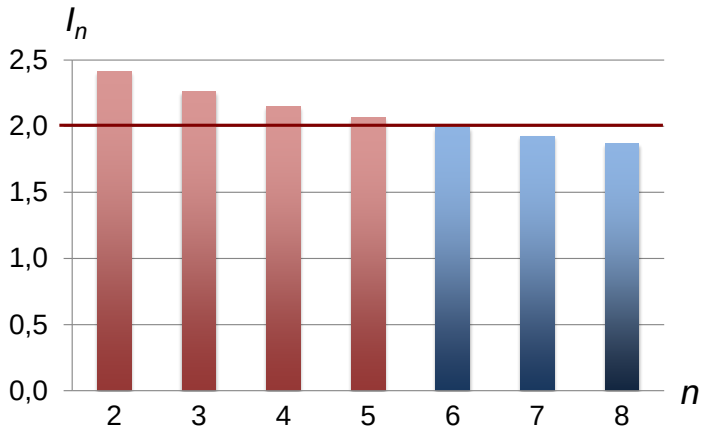

Figure 4.23 This histogram shows the values taken by the quantity I_n when the number of detected photons n on each WFH varies between 2 and 8. The bound for I_n predicted by local realism is 2 for all values of n, hence we see that no violation of a generalised Bell inequality is possible beyond $n = 5$ with a two-mode squeezed vacuum state probed by weak-field homodyne detectors.

Fig. 4.23, and show that no violation is achieved beyond $n = 5$. Furthermore, the quantum bound of 4 is never attained. We may explain this behaviour by noting that the maximal violation based on I_n relies on a particular structure for the input state, as discussed in [88]. However, a two-mode squeezed state is specified solely by the squeezing parameter λ: the limited degrees of freedom do not allow for the form of the input state to be tuned as required by these generalised inequalities. The restriction becomes more severe as the dimensionality of the system increases, to the point that no violation can be inferred despite the use of an entangled resource such as a TMSS. This behaviour may stem from the Gaussian character of the squeezed vacuum state: indeed, we see that the functional shape of $\langle \hat{P}_{kk'} \rangle$ (shown for

$k = k' = 1$ and $k = k' = 2$ in Fig. 4.22) is simultaneously fixed for every accessible Fock layer.

The study that we have just presented can be viewed in the more general framework of Gaussian versus non-Gaussian measurements. The outcomes of a Gaussian measurement on a Gaussian quantum state can be explained by a LVT. For this reason, strong-field homodyne detection of a TMSS cannot be used to violate a Bell inequality. On the other hand, weak homodyning performs non-Gaussian measurements, as attested by its POVM [86]. Consequently, we would expect that the outcomes of WFH detection on an entangled Gaussian state cannot be described by a local realistic model. Our investigation suggests that this fails for moderately high photon numbers, which we can also regard as the transition from non-Gaussian to Gaussian measurements – a transition corresponding to an increase in the LO intensity in the context of weak-field homodyne detection. From a broader perspective, our results indicate that non-Gaussianity is only one aspect in the violation of a Bell inequality; this opens the way to further studies aimed at identifying the origin of non-locality.

Conclusions

Summary

This doctoral work was motivated by the growing interest in hybrid techniques – combining the DV and CV descriptions of light fields – for QIP. Over the past decades, the idea of turning the wave-particle duality from intellectual matter of debate into powerful resource has taken on various forms, depending on the motivations and goals of the specific theoretical proposal or experimental implementation. In this thesis, we have presented the realisation and discussed the applications of a two-mode weak-field homodyne detection scheme which unites photon-number-resolved counting and phase sensitivity.

We first investigated the direct reconstruction of defining properties for a two-mode squeezed vacuum state, sampling its Wigner function point by point and obtaining its photon distribution from the click counting statistics. The preliminary study of the vacuum and thermal states highlighted the instability of a naive inversion of the loss matrices for the reconstruction of the photon distribution. To keep the data post-processing to a minimum, we only took into account the multiplexed nature of our detectors in the subsequent analysis of the data for the TMSS. In this case,

the reconstruction aimed at a direct estimation of squeezing with WFH detection. For some choices of the UV pump power and the coherent-state amplitudes, our data shows good qualitative agreement with a theoretical Wigner function which predicts one squeezed variance. However, such encouraging results would have to be confirmed for different values of source brightness and amplitudes of the local oscillators. Hence the study discussed here does not yet provide a definitive proof of the reliable reconstruction of the considered two-mode Gaussian resource by sampling of the four-dimensional phase space with WFH detectors.

Secondly, we have shown that our layout allows us to deconstruct phase-dependent measurements on two-mode entangled states into their constituent photon-number layers. We experimentally demonstrated the observation of non-classical optical coherence – intended here as a wave-like phenomenon – in the joint click counting probabilities corresponding to discrete detection events. In this case we considered two important classes of two-mode states, namely a split single photon and the squeezed vacuum. For each quantum resource, we were able to describe the behaviour of the click counting statistics with a model based on few assumptions and a limited number of experimental parameters. These theoretical descriptions allowed us to compare the effects of loss and non-ideal state generation on the phase-dependent joint counting probabilities. Notably, the visibilities of the oscillating terms highlight that it is the whole matrix $\mathbf{P}$, rather than each individual term, which we must consider to assess the role of the observed non-classical correlations as quantum resources. This observation further motivated our theoretical study of the violation of generalised Bell inequalities with a TMSS probed by weak-field homodyne detectors.

Outlook

Progress in all-DV [89, 90] and all-CV [91–94] schemes for quantum information processing has evidenced individual strengths and drawbacks of both approaches [95, 96]. Consequently, drawing on the advantages of each framework to overcome their respective limitations is a solution worth exploring. For instance, near-deterministic teleportation was shown to be achievable with hybrid quantum resources [97]; however, such protocols require very efficient detectors as well as high fidelities for the preparation of the hybrid entangled states. Recent experimental realisations successfully addressed the latter requirement [98, 99]. Similarly, the demonstration of entanglement swapping between continuous and discrete variables constitutes an encouraging achievement [100]. These experimental advances call for a corresponding theoretical effort towards measuring and classifying hybrid correlations to evaluate the performance of schemes relying on qudit-qumode entanglement [101–103].

The ability to operate our WFH layout at the interface of wave and particle regimes places this work well within the ongoing research into hybrid approaches to QIP, be it for computing [104, 105] or towards the realisation of heterogeneous networks for communication protocols [106, 107].

The experimental data that we collected and analysed provides valuable insight into the strengths and limitations of our current setup, suggesting modifications and improvements should this scheme be utilised and/or adapted for future experiments. A partial redesign could extend the life of the present layout: each arm of the interferometer has a length of two metres, hence a more compact arrangement would

provide greater passive stability and possibly reduce the negative effects of the observed beam pointing instability of the main IR laser beam[4]. Moreover, it would be extremely useful to benefit from the possibility of shining a coherent signal of tunable intensity in the pump beam path: particularly, this would allow for a more precise calibration of the detection system.

We can now comment on further perspectives for our experimental layout based on an observation about the role of loss in the violation of high-order Bell inequalities with WFH detectors as discussed in Chapter 4. In Fig. 4.22 we showed the dependence of the expectation values for the considered Fock-state projection operators (see Eqn.(4.19) and (4.20)) on the phases of the coherent-state probes. In Fig. 4.20 we highlighted that low detection efficiencies decrease the visibility of the oscillations in the click counting probabilities (and at the same time artificially enhance the vacuum contribution); here we wish to stress that this effect is more pronounced for higher Fock layers. Let us consider a simplified scenario where the most prominent contribution to noise in layer n comes from layer $n+1$: because of inefficient detection, we 'miss' one in $n+1$ photons, adding a spurious term to the probability associated with layer n. Assuming that all involved detectors have the same efficiency η, we write each detection probability as $P \propto \eta^n P_n + \binom{n+1}{1}\eta^n(1-\eta)\nu_{n+1}$, where P_n is the ideal value (for $\eta = 1$), and ν_{n+1} is the noise contribution coming from Fock layer $n+1$ upon loss of one photon. We thus see that the relative weight of the noise term becomes more important as n increases. In this sense, the achievable violation of a generalised Bell inequality with the considered layout not only

[4]The point locking system and an active stabilisation of the phase would still be necessary; however, a more compact design could allow us to operate these systems in less critical conditions.

decreases with n – it also becomes less resilient to loss.

In the light of this remark, future experimental investigations on the violation of Bell-type inequalities in high-dimensional systems would benefit from highly efficient single-photon detectors. Indeed, if our setup was rebuilt to operate at telecom wavelengths this could improve both the performance and the reliability of the weak-field homodyne layout. The parametric source could be realised in a waveguide to achieve better control of the produced spatial modes, and a promising technology such as transition-edge sensors (TESs) could provide high detection efficiencies. Importantly, these detectors are also inherently energy-sensitive; however, the current major drawback of TESs is the requirement of very low temperatures for optimal performance [52].

Finally, we remark that hybrid QIP does not seem to have yet merged with integrated optics (except for on-chip parametric sources embedded in an otherwise bulk setup). This is perhaps because, once again, most efforts have been so far devoted to applications in the discrete-variable framework – although the recent generation and characterisation of EPR states in a photonic chip represent a pioneering step which may open the way to new research directions [108]. Integrated technologies are a most promising development of the past two decades: they have been driving a miniaturisation trend which is not only relevant to the ever-present scalability concern, but also ensures a compact design for experimental layouts that are intrinsically more stable while offering better control. It will thus be interesting to witness what progress may be achieved through the combination of integrated optics and hybrid approaches to quantum information processing.

Appendix: Experimental conditional probability matrices

We tailor the contents included in this appendix to our experimental detection setup. Precisely, we determine the conditional probability matrices for two time-multiplexed detectors each characterised by 8 temporal bins. As discussed in Chapter 3, the weight assigned to every detection mode should be $w_i = 1/8$ for all i; however, this is not the case for a non-ideal TMD where the individual components and the way they are assembled contribute to deviations from perfect operation.

To estimate the mode weightings experimentally, we block the signal from the PDC source and use the LO to probe the binned structure of our detectors on all four avalanche photodiodes. To this end, we take advantage of a specific function of our acquisition board which allows us to identify the four temporal bins for each APD by producing replicas of the external reference (or trigger) used for time gating, subsequently registering coincidence counts between the trigger and the signal from the considered APD within a given acquisition time. This procedure generates plots such as the ones shown in the following figure for two of the four photon counters.

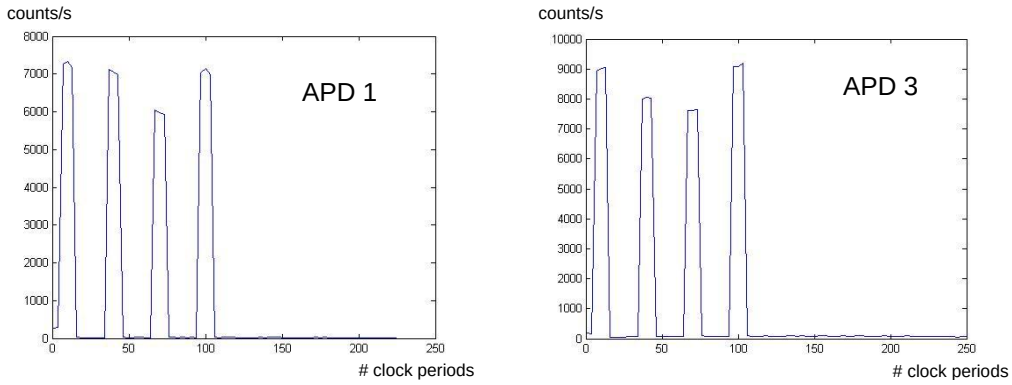

Determination of the relative delay between a signal detected in the temporal bins of APDs 1 and 3, associated with TMD A and TMD B respectively, and the external trigger from the laser system. For a reliable measurement, we must set the amplitude of the LO so that all bins saturate (that is, they are as populated as they can be). The total acquisition time reported on the horizontal axis corresponds to 255 FPGA clock periods; here 1 clock period has a duration of 3 ns.

From the data collected with these temporal scans, we can compute the weights $\{w_i\}_{i=1,\ldots,8}$ for both TMDs as the ratios between the counts in each temporal bin over the total number of 'clicks' recorded by the two APDs associated with either time-multiplexed detector: this leads to the values reported in the table below.

Once the mode weights for the considered detection system are known, we refer back to the assumptions discussed in Chapter 3 (see Section 3.2) to reconstruct the conditional probability matrices for our time-multiplexed detectors.

TMD A (APD 1 and 2)		TMD B (APD 3 and 4)	
w_1	0.1139	w_1	0.1357
w_2	0.1097	w_2	0.1199
w_3	0.0920	w_3	0.1141
w_4	0.1111	w_4	0.1360
w_5	0.1663	w_5	0.1269
w_6	0.1348	w_6	0.1264
w_7	0.1402	w_7	0.1039
w_8	0.1320	w_8	0.1371

Experimental values of the mode weights for the TMDs constituting our detection system. These figures are rounded off so that they sum to unity for each detector.

Specifically, conservation of probability imposes that

$$\left(\sum_{i=1}^{8} w_i\right)^n = 1 \quad \Longleftrightarrow \quad \sum_{\{l_1,\ldots,l_8\}} \frac{n!}{l_1!\cdots l_8!} w_1^{l_1}\cdots w_8^{l_8} = 1\,, \tag{A.1}$$

where n represents the number of incoming photons and $\sum_{\{l_1,\ldots,l_8\}}$ indicates the sum over all sequences of non-negative integers such that $\sum_{i=1}^{8} l_i = n$. In our case we let n run from 0 to 8, as this range of values[5] coincides with the resolution of the TMDs (that is, the number of available bins). The elements $\{C_{kn}\}$ of a conditional probability matrix must be such that $\sum_{n,k=0}^{8} C_{kn} = 1$ for $k \leq n$ (see Chapter 3). The above result indicates that we need to treat separately every configuration of incoming particles (identified by the value of n); the elements of the considered $\mathbf{C}$ matrix appear as we apply Eq.(A.1) to each specific case. For $n = 0$ and $n = 1$ we obtain $C_{00} = 1$ and $C_{11} = 1$ (as we focus on the binned structure of the detectors and assume that they are lossless devices – see Chapter 3, Section 3.2). The case $n = 2$ yields

$$\left(\sum_{i=1}^{8} w_i\right)^2 = 1 \quad \Longleftrightarrow \quad \sum_{\{l_1,\ldots,l_8\}} \frac{2!}{l_1!\cdots l_8!} w_1^{l_1}\cdots w_8^{l_8} = 1\,,$$

where the left-hand side of the second equality can be rewritten as

$$\sum_{\{l_1,\ldots,l_8\}} \frac{2!}{l_1!\cdots l_8!} w_1^{l_1}\cdots w_8^{l_8} = \frac{2!}{2!}\sum_{i=1}^{8} w_i^2 + \frac{2!}{1!1!}\left(\sum_{i,j=1}^{8} w_i w_j - \sum_{\substack{i,j=1\\ i=j}}^{8} w_i w_j\right)\frac{1}{2!}\,.$$

[5] In the experimental results presented in Chapter 3 and Chapter 4, we recall that we further restricted our attention to the subset $n = 0, 1, 2$ given the brightness of our source.

We thus identify

$$C_{12} = \frac{2!}{2!}\sum_{i=1}^{8} w_i^2 \,, \qquad C_{22} = \frac{2!}{1!1!}\left(\sum_{i,j=1}^{8} w_i w_j - \sum_{\substack{i,j=1 \\ i=j}}^{8} w_i w_j\right)\frac{1}{2!}$$

for the non-zero elements in the second column of $\mathbf{C}$. In the expression for C_{22} we must require that $i \neq j$ to avoid including terms which belong to C_{12}. Moreover, the factor (1/2!) is added to take into account 'redundant terms' coming from weights raised to the same power – for instance, both $w_1 w_2$ and $w_2 w_1$ appear in C_{22} although the two terms coincide. As we compute the other terms in the conditional probability matrix, these considerations remain valid.

Iteration of the above procedure for all considered values of n allows us to calculate the coefficients of a 9×9 matrix. Our experimental conditional probability matrices are reported in Eqn.(A.2) (for TMD A) and (A.3) (for TMD B).

$$\mathbf{C}_{\mathrm{A}} = \begin{pmatrix} 1 & 0 & 0 & 0 & 0 & 0 & 0 & 0 & 0 \\ 0 & 1 & 0.1287 & 0.0171 & 0.0023 & 0.0003 & 0 & 0 & 0 \\ 0 & 0 & 0.8713 & 0.3350 & 0.1017 & 0.0287 & 0.0079 & 0.0022 & 0.0006 \\ 0 & 0 & 0 & 0.6479 & 0.4962 & 0.2662 & 0.1243 & 0.0543 & 0.0229 \\ 0 & 0 & 0 & 0 & 0.3999 & 0.5082 & 0.4222 & 0.2922 & 0.1833 \\ 0 & 0 & 0 & 0 & 0 & 0.1966 & 0.3732 & 0.4426 & 0.4233 \\ 0 & 0 & 0 & 0 & 0 & 0 & 0.0756 & 0.1911 & 0.3059 \\ 0 & 0 & 0 & 0 & 0 & 0 & 0 & 0.0176 & 0.0619 \\ 0 & 0 & 0 & 0 & 0 & 0 & 0 & 0 & 0.0021 \end{pmatrix} \tag{A.2}$$

$$\mathbf{C}_{\mathrm{B}} = \begin{pmatrix} 1 & 0 & 0 & 0 & 0 & 0 & 0 & 0 & 0 \\ 0 & 1 & 0.1260 & 0.0160 & 0.0020 & 0.0003 & 0 & 0 & 0 \\ 0 & 0 & 0.8740 & 0.3300 & 0.0973 & 0.0264 & 0.0069 & 0.0018 & 0.0005 \\ 0 & 0 & 0 & 0.6540 & 0.4933 & 0.2590 & 0.1177 & 0.0498 & 0.0203 \\ 0 & 0 & 0 & 0 & 0.4074 & 0.5116 & 0.4182 & 0.2836 & 0.1738 \\ 0 & 0 & 0 & 0 & 0 & 0.2028 & 0.3815 & 0.4471 & 0.4215 \\ 0 & 0 & 0 & 0 & 0 & 0 & 0.0722 & 0.1989 & 0.3159 \\ 0 & 0 & 0 & 0 & 0 & 0 & 0 & 0.0188 & 0.0658 \\ 0 & 0 & 0 & 0 & 0 & 0 & 0 & 0 & 0.0023 \end{pmatrix} \tag{A.3}$$

Acknowledgements

While I stare at this blank page, I am increasingly aware of the fact that if it was challenging to condense four-and-actually-close-to-five years of doctoral studies in about 200 pages, it is even trickier to acknowledge the change of perspective, the experiences and encounters that have characterised my time in Oxford.

I remember that I decided to embark on this 'adventure' because I wished to seek the answer to a few questions – how much do I like research in quantum information? How is it to live and study abroad on my own? What are my medium-to-long-term career plans? Although the answers came in ways that I could hardly foresee, I believe that these questions are now less fuzzy than they used to look like as I moved to England.

I would like to thank my supervisor, Ian Walmsley, for making this 'D.Phil. experience' possible – he often manages to ask *the one question* that I cannot answer (as I did not even think of *that aspect*). I also thank Ian for trying to infuse some positive thinking; I still do not believe that "it'll be fine", but I appreciate the attempt at reminding me that, sometimes, things do work. To Marco Barbieri – thank you so much for being enthusiastic about research, physics and everything optical. I suspect that this thesis would not look as it presently does without Dr Barbieri (who also read the whole document – thank you for this, too). As a whole, the Ultrafast Group has grown to a size which makes it hardly human to mention the many ultrafasters I interacted with over the past years. I would like to thank everyone in the IEP laboratory for such a wide and diverse human presence – it was a most instructive experience. Particularly, many thanks to Justin Spring for all things FPGA-related and to Mihai Vidrighin for the point locking software; I am also grateful to Animesh Datta and Andreas Eckstein for theoretical and experimental support with my doctoral project. A special thank you goes to Sean McCormack at Coherent Ltd for rescuing our laser system a few times; I shall also thank the brave people who try to bring Oxford's bureaucracy to acceptable levels of complexity (and often succeed).

My life in Oxford would have been very much incomplete without Linacre College – thank you to all the truly beautiful Linacrites whom I had the chance to meet and befriend.

To conclude, I will switch to Italian – in particolare per ringraziare i miei genitori, Gabriella e Flavio, nella mia lingua (il cui suono spesso mi manca): grazie per l'inimmaginabile sostegno morale e per i preziosi insegnamenti – spero di rendere giustizia a questa eredità. E grazie mille alla persona eccezionale – anche nota come *orso* – con la quale ho avuto la fortuna di condividere una parte di questa avventura britannica.

And as it happens, the page is not blank anymore.

"Living in a mental world of absolute rights and wrongs
may be imagining that because all theories are wrong,
the earth may be thought spherical now,
but cubical next century,
and a hollow icosahedron the next,
and a doughnut shape the one after.
What actually happens is that
once scientists get hold of a good concept
they gradually refine and extend it
with greater and greater subtlety
as their instruments of measurement improve.
Theories are not so much wrong as incomplete."

The relativity of wrong, Isaac Asimov

Bibliography

[1] J. P. Gordon, H. J. Zeiger, and C. H. Townes. The Maser–New type of microwave amplifier, frequency standard, and spectrometer. *Phys. Rev.*, 99:1264, 1955.

[2] R. J. Glauber. The quantum theory of optical coherence. *Phys. Rev.*, 130:2529, 1963.

[3] R. Hanbury Brown and R. Q. Twiss. Correlation between photons in two coherence beams of light. *Nature*, 177:27, 1956.

[4] T. H. Maiman. Stimulated optical radiation in ruby. *Nature*, 187:493, 1960.

[5] A. L. Shawlow. Optical and infrared masers. *Contemp. Phys.*, 5:81, 2006.

[6] R. L. Byer and S. E. Harris. Power and bandwidth of spontaneous parametric emission. *Phys. Rev.*, 168:1064, 1968.

[7] P. G. Kwiat, K. Mattle, H. Weinfurter, A. Zeilinger, A. V. Sergienko, and Y. Shih. New high-intensity source of polarization-entangled photon pairs. *Phys. Rev. Lett.*, 75:4337, 1995.

[8] P. G. Kwiat, E. Waks, A. G. White, I. Appelbaum, and P. H. Eberhard. Ultrabright source of polarization-entangled photons. *Phys. Rev. A*, 60:R773, 1999.

[9] C. Kurtsiefer, M. Oberparleiter, and H. Weinfurter. High-efficiency entangled photon pair collection in type-ii parametric fluorescence. *Phys. Rev. A*, 64:023802, 2001.

[10] A. G. White, D. F. V. James, P. H. Eberhard, and P. G. Kwiat. Nonmaximally entangled states: Production, characterization, and utilization. *Phys. Rev. Lett.*, 83:3103, 1999.

[11] A. Ourjoumtsev, R. Tualle-Brouri, J. Laurat, and P. Grangier. Generating optical Schrödinger kittens for quantum information processing. *Science*, 312:83, 2006.

[12] R. Demkowicz-Dobrzański, M. Jarzyna, and J. Kołodyński. Quantum limits in optical interferometry. arXiv, 2014. 1405:7703v2.

[13] U. L. Andersen, G. Leuchs, and C. Silberhorn. Continuous-variable quantum information processing. *Laser and Photon. Rev.*, 4:337, 2010.

[14] A. Ourjoumtsev. *Theoretical and experimental study of quantum coherent superpositions and of non-gaussian entangled states of the light.* PhD thesis, Université Paris Sud - Paris XI, 2007.

[15] D. T. Smithey, M. Beck, M. G. Raymer, and A. Faridani. Measurement of the Wigner distribution and the density matrix of a light mode using optical

homodyne tomography: Application to squeezed states and the vacuum. *Phys. Rev. Lett.*, 70:1244, 1993.

[16] F. Grosshans and P. Grangier. Continuous variable quantum cryptography using coherent states. *Phys. Rev. Lett.*, 88:057902, 2002.

[17] T. Hirano, H. Yamanaka, M. Ashikaga, T. Konishi, and R. Namiki. Quantum cryptography using pulsed homodyne detection. *Phys. Rev. A*, 68:042331, 2003.

[18] H. Yonezawa, T. Aoki, and A. Furusawa. Demonstration of a quantum teleportation network for continuous variables. *Nature*, 431:430, 2004.

[19] L. Zhang, C. Silberhorn, and I. A. Walmsley. Secure quantum key distribution using continuous variables of single photons. *Phys. Rev. Lett.*, 100:110504, 2008.

[20] D. Gottesman, A. Kitaev, and J. Preskill. Encoding a qubit in an oscillator. *Phys. Rev. A*, 64:012310, 2001.

[21] S. D. Bartlett and B. C. Sanders. Universal continuous-variable quantum computation: Requirement of optical nonlinearity for photon counting. *Phys. Rev. A*, 65:042304, 2002.

[22] P. Grangier, M. J. Potasek, and B. Yurke. Probing the phase coherence of parametrically generated photon pairs: a new test of Bell's inequalities. *Phys. Rev. A*, 38:3132, 1988.

[23] S. Wallentowitz and W. Vogel. Unbalanced homodyning for quantum state measurements. *Phys. Rev. A*, 53:4528, 1996.

[24] G. Puentes, J. S. Lundeen, M. P. A. Branderhorst, H. B. Coldenstrodt-Ronge, B. J. Smith, and I. A. Walmsley. Bridging particle and wave sensitivity in a configurable detector of positive operator-valued measures. *Phys. Rev. Lett.*, 102:080404, 2009.

[25] A. Kuzmich, I. A. Walmsley, and L. Mandel. Violation of Bell's inequality by a generalised Einstein-Podolski-Rosen state using homodyne detection. *Phys. Rev. Lett.*, 85:1349, 2000.

[26] B. Hessmo, P. Usachev, H. Heydari, and G. Björk. Experimental demonstration of single photon nonlocality. *Phys. Rev. Lett.*, 92:180401, 2004.

[27] K. Banaszek and K. Wódkiewicz. Direct probing of quantum phase space by photon counting. *Phys. Rev. Lett.*, 76:4344, 1996.

[28] K. Laiho, K. Cassemiro, D. Gross, and C. Silberhorn. Probing the negative Wigner function of a pulsed single photon point by point. *Phys. Rev. Lett.*, 105:253603, 2010.

[29] M. Dakna, T. Anhut, T. Opatrný, L. Knöll, and D.-G. Welsch. Generating Schrödinger-cat-like states by means of conditional measurements on a beam splitter. *Phys. Rev. A*, 55:3184, 1997.

[30] A. Zavatta, S. Viciani, and M. Bellini. Quantum-to-classical transition with single-photon-added coherent states of light. *Science*, 306:660, 2004.

[31] J. S. Neergaard-Nielsen, M. Takeuchi, K. Wakui, H. Takahashi, K. Hayasaka, M. Takeoka, and M. Sasaki. Optical continuous-variable qubit. *Phys. Rev. Lett.*, 105:053602, 2010.

[32] T. Kiesel, W. Vogel, B. Hage, and R. Schnabel. Entangled qubits in a non-Gaussian quantum state. *Phys. Rev. A*, 83:062319, 2011.

[33] R. Loudon. *The Quantum Theory of Light*. Oxford University Press, 3rd edition, 2000.

[34] M. O. Scully and M. S. Zubairy. *Quantum Optics*. Cambridge University Press, 1997.

[35] U. Leonhardt. *Measuring the Quantum State of Light*. Cambridge University Press, 1997.

[36] C. W. Gardiner. *Quantum Noise*. Springer-Verlag, 1991.

[37] E. A. Goldschmidt, F. Piacentini, I. R. Berchera, S. V. Polyakov, S. Peters, S. Kück, G. Brida, I. P. Degiovanni, A. Migdall, and M. Genovese. Mode reconstruction of a light field by multiphoton statistics. *Phys. Rev. A*, 88:013822, 2013.

[38] A. Eckstein. *Mastering quantum light pulses with nonlinear waveguide interactions*. PhD thesis, Friedrich-Alexander-Universität Erlangen-Nürnberg, 2012.

[39] J. H. Eberly. Schmidt analysis of pure-state entanglement. *Las. Phys.*, 16:921, 2006.

[40] A. Ekert and P. L. Knight. Entangled quantum systems and the Schmidt decomposition. *Am. J. Phys.*, 63:415, 1995.

[41] C. K. Law, I. A. Walmsley, and J. H. Eberly. Continuous frequency entanglement: Effective finite Hilbert space and entropy control. *Phys. Rev. Lett.*, 84:5304, 2000.

[42] A. Einstein, B. Podolsky, and N. Rosen. Can quantum-mechanical description of physical reality be considered complete? *Phys. Rev.*, 47:777, 1935.

[43] J. S. Bell. *Speakable and unspeakable in quantum mechanics.* Cambridge University Press, 1987.

[44] A. Aspect, P. Grangier, and G. Roger. Experimental realization of Einstein-Podolsky-Rosen-Bohm *Gedankenexperiment*: A new violation of Bell's inequalities. *Phys. Rev. Lett.*, 49:91, 1982.

[45] A. Aspect, J. Dalibard, and G. Roger. Experimental test of Bell's inequalities using time- varying analyzers. *Phys. Rev. Lett.*, 49:1804, 1982.

[46] Y. H. Shih and C. O. Alley. New type of Einstein-Podolsky-Rosen-Bohm experiment using pairs of light quanta produced by optical parametric down conversion. *Phys. Rev. Lett.*, 61:2921, 1988.

[47] G. Weihs, T. Jennewein, C. Simon, H. Weinfurter, and A. Zeilinger. Violation

of Bell's inequality under strict Einstein locality conditions. *Phys. Rev. Lett.*, 81:5039, 1998.

[48] M. A. Rowe, D. Kielpinski, V. Meyer, C. A. Sackett, W. M. Itano, C. Monroe, and D. J. Wineland. Experimental violation of a Bell's inequality with efficient detection. *Nature*, 409:791, 2001.

[49] D. L. Moehring, M. J. Madsen, B. B. Blinov, and C. Monroe. Experimental Bell inequality violation with an atom and a photon. *Phys. Rev. Lett.*, 93:090410, 2004.

[50] C. K. Hong, Z. Y. Ou, and L. Mandel. Measurement of subpicosecond time intervals between two photons by interference. *Phys. Rev. Lett.*, 59:2044, 1987.

[51] D. C. Burnham and D. L. Weinberg. Observation of simultaneity in parametric production of optical photon pairs. *Phys. Rev. Lett.*, 25:84, 1970.

[52] A. Migdall, S. Y. Polyakov, J. Fan, and J. C. Bienfang, editors. *Single-Photon Generation and Detection – Experimental Methods in the Physical Sciences.* Elsevier Academic Press, 2013.

[53] R. W. Boyd. *Nonlinear Optics.* Elsevier Academic Press, 2nd edition, 2003.

[54] D. R. Truax. Baker-Campbell-Hausdorff relations and unitarity of SU(2) and SU(1,1) squeeze operators. *Phys. Rev. D*, 31:1988, 1985.

[55] S. M. Barnett and S. J. D. Phoenix. Entropy as a measure of quantum optical correlation. *Phys. Rev. A*, 40:2404, 1989.

[56] W. P. Grice and I. A. Walmsley. Spectral information and distinguishability in type-ii down-conversion with a broadband pump. *Phys. Rev. A*, 56:1627, 1997.

[57] W. P. Grice, A. B. U'Ren, and I. A. Walmsley. Eliminating frequency and space-time correlations in multiphoton states. *Phys. Rev. A*, 64:063815, 2001.

[58] N. J. Cerf, G. Leuchs, and E. S. Polzik, editors. *Quantum information with continuous variables of atoms and light*. Imperial College Press, 2007.

[59] A. Christ, K. Laiho, A. Eckstein, K. N. Cassemiro, and C. Silberhorn. Probing multimode squeezing with correlation functions. *New J. of Phys.*, 13:033027, 2011.

[60] R. H. Hadfield. Single-photon detectors for optical quantum information processing. *Nat. Photon.*, 3:696, 2009.

[61] D. N. Klyshko. Observable signs of nonclassical light. *Phys. Lett. A*, 213:7, 1996.

[62] C. M. Natarajan, L. Zhang, H. Coldenstrodt-Ronge, G. Donati, S. N. Dorenbos, V. Zwiller, I. A. Walmsley, and R. H. Hadfield. Quantum detector tomography of a time-multiplexed superconducting nanowire single-photon detector at telecom wavelengths. *Opt. Expr.*, 21:893, 2013.

[63] Z. Y. Ou, C. K. Hong, and L. Mandel. Detection of squeezed states by cross correlation. *Phys. Rev. A*, 36:192, 1987.

[64] J. Sperling, W. Vogel, and G. S. Agarwal. True photocounting statistics of multiple on-off detectors. *Phys. Rev. A*, 85:023820, 2012.

[65] D. Achilles, C. Silberhorn, C. Sliwa, K. Banaszek, I. A. Walmsley, M. J. Fitch, B. C. Jacobs, T. B. Pittman, and J. D. Franson. Photon-number-resolving detection using time-multiplexing. *J. of Mod. Opt.*, 51:1499, 2004.

[66] A. P. Worsley. Measurement of the joint statistics of a single photon source generating pure quantum states. M.Phys. project report, University of Oxford, 2008.

[67] K. Cahill and R. Glauber. Ordered expansions in boson amplitude operators. *Phys. Rev.*, 177:1857, 1969.

[68] K. Cahill and R. Glauber. Density operators and quasiprobability distributions. *Phys. Rev.*, 177:1882, 1969.

[69] Royer A. Wigner function as the expectation value of a parity operator. *Phys. Rev. A*, 15:449, 1976.

[70] M. G. A. Paris. Displacement operator by beam splitter. *Phys. Lett. A*, 217:78, 1996.

[71] A. P. Worsley, H. B. Coldenstrodt-Ronge, J. S. Lundeen, P. J. Mosley, B. J. Smith, G. Puentes, N. Thomas-Peter, and I. A. Walmsley. Absolute efficiency estimation of photon-number-resolving detectors using twin beams. *Opt. Express*, 17:4397, 2009.

[72] K. Banaszek, C. Radzewicz, K. Wódkiewicz, and J. S. Krasiński. Direct measurement of the Wigner function by photon counting. *Phys. Rev. A*, 60:674, 1999.

[73] K. Banaszek, A. Dragan, K. Wódkiewicz, and C. Radzewicz. Direct measurement of optical quasidistribution functions: multimode theory and homodyne tests of Bell's inequalities. *Phys. Rev. A*, 66:043803, 2002.

[74] K. Laiho, M. Avenhaus, K. Cassemiro, and C. Silberhorn. Direct probing of the Wigner function by time-multiplexed detection of photon statistics. *New J. of Phys.*, 11:043012, 2009.

[75] J. Sperling, W. Vogel, and G. S. Agarwal. Sub-binomial light. *Phys. Rev. Lett.*, 109:093601, 2012.

[76] T. J. Bartley, G. Donati, X.-M. Jin, A. Datta, M. Barbieri, and I. A. Walmsley. Direct observation of sub-binomial light. *Phys. Rev. Lett.*, 110:173602, 2013.

[77] G. Donati, T. J. Bartley, X.-M. Jin, M.-D. Vidrighin, A. Datta, M. Barbieri, and I. A. Walmsley. Observing optical coherence across fock layers with weak-field homodyne detectors. *Nat. Commun.*, 5:5584, 2014.

[78] P. J. Mosley. *Generation of heralded single photons in pure quantum states.* PhD thesis, University of Oxford, 2007.

[79] P. J. Mosley, J. S. Lundeen, B. J. Smith, Piotr W., A. B. U'Ren, C. Silberhorn, and I. A. Walmsley. Heralded generation of ultrafast single photons in pure quantum states. *Phys. Rev. Lett.*, 100:133601, 2008.

[80] P. J. Mosley, J. S. Lundeen, B. J. Smith, and I. A. Walmsley. Conditional preparation of single photons using parametric downconversion: a recipe for purity. *New J. of Phys.*, 10:093011, 2008.

[81] T. J. Bartley, G. Donati, J. B. Spring, X.-M. Jin, M. Barbieri, A. Datta, B. J. Smith, and I. A. Walmsley. Multiphoton state engineering by heralded interference between single photons and coherent states. *Phys. Rev. A*, 86:043820, 2012.

[82] J. B. Spring. *Single photon generation and quantum computing with integrated photonics*. PhD thesis, University of Oxford, 2014.

[83] J. G. Rarity, P. R. Tapster, and R. Loudon. Non-classical interference between independent sources. *J. Opt. B.: Quantum Semiclass. Opt.*, 7:S171, 2005.

[84] A. Kuzmich, I. A. Walmsley, and L. Mandel. Violation of a Bell-type inequality in the homodyne measurement of light in an Einstein-Podolski-Rosen state. *Phys. Rev. A*, 64:063804, 2001.

[85] G. Björk, P. Jonsson, and L. L. Sánchez-Soto. Single-particle nonlocality and entanglement with the vacuum. *Phys. Rev. A*, 64:042106, 2001.

[86] L. Zhang, H. B. Coldenstrodt-Ronge, A. Datta, G. Puentes, J. S. Lundeen, X.-M. Jin, B. J. Smith, M. B. Plenio, and I. A. Walmsley. Mapping coherence in measurement via full quantum tomography of a hybrid optical detector. *Nat. Photon.*, 6:364, 2012.

[87] D. Collins, N. Gisin, N. Linden, S. Massar, and S. Popescu. Bell inequalities for arbitrarily high-dimensional systems. *Phys. Rev. Lett.*, 88:040404, 2002.

[88] A. Acín, T. Durt, N. Gisin, and J. I. Latorre. Quantum nonlocality in two three-level systems. *Phys. Rev. A*, 65:052325, 2002.

[89] W.-B. Gao, C.-Y. Lu, X.-C. Yao, P. Xu, O. Gühne, A. Goebel, Y.-A. Chen, C.-Z. Peng, Z.-B. Chen, and J.-W. Pan. Experimental demonstration of a hyper-entangled ten-qubit Schrödinger cat state. *Nat. Phys.*, 6:331, 2010.

[90] B. J. Metcalf *et al.*. Quantum teleportation on a photonic chip. *Nat. Photon.*, 8:770, 2014.

[91] J. S. Neergaard-Nielsen, B. M. Nielsen, C. Hettich, K. Mølmer, and E. S. Polzik. Generation of a superposition of odd photon number states for quantum information networks. *Phys. Rev. Lett.*, 97:083604, 2006.

[92] H. Takahashi, K. Wakui, S. Suzuki, M. Takeoka, K. Hayasaka, A. Furusawa, and M. Sasaki. Generation of large-amplitude coherent-state superposition via ancilla-assisted photon subtraction. *Phys. Rev. Lett.*, 101:233605, 2008.

[93] A. Ourjoumtsev, F. Ferreyrol, R. Tualle-Brouri, and P. Grangier. Preparation of non-local superpositions of quasi-classical light states. *Nat. Phys.*, 5:189, 2009.

[94] T. Gerrits, S. Glancy, T. S. Clement, B. Calkins, A. E. Lita, A. J. Miller, A. L. Migdall, S. W. Nam, R. P. Mirin, and E. Knill. Generation of optical

coherent-state superpositions by number-resolved photon subtraction from the squeezed vacuum. *Phys. Rev. A*, 82:031802, 2010.

[95] K. Park and H. Jeong. Entangled coherent states versus entangled photon pairs for practical quantum-information processing. *Phys. Rev. A*, 82:062325, 2010.

[96] P. van Loock. Optical hybrid approaches to quantum information. *Laser and Photon. Rev.*, 5:167, 2011.

[97] S.-W. Lee and H. Jeong. Near-deterministic quantum teleportation and resource-efficient quantum computation using linear optics and hybrid qubits. *Phys. Rev. A*, 87:022326, 2013.

[98] O. Morin, K. Huang, J. Liu, H. Le Jeannic, C. Fabre, and J. Laurat. Remote creation of hybrid entanglement between particle-like and wave-like optical qubits. *Nat. Photon.*, 8:570, 2014.

[99] H. Jeong, A. Zavatta, M. Kang, S.-W. Lee, L. S. Costanzo, S. Grandi, T. C. Ralph, and M. Bellini. Generation of hybrid entanglement of light. *Nat. Photon.*, 8:564, 2014.

[100] S. Takeda, M. Fuwa, P. van Loock, and A. Furusawa. Entanglement swapping between discrete and continuous variables. *Phys. Rev. Lett.*, 114:100501, 2015.

[101] J. Rigas, O. Gühne, and N. Lütkenhaus. Entanglement verification for quantum-key-distribution systems with an underlying bipartite qubit-mode structure. *Phys. Rev. A*, 73:012341, 2006.

[102] N. Spagnolo, C. Vitelli, M. Paternostro, F. De Martini, and F. Sciarrino. Hybrid methods for witnessing entanglement in a microscopic-macroscopic system. *Phys. Rev. A*, 84:032102, 2011.

[103] K. Kreis and P. van Loock. Classifying, quantifying, and witnessing qudit-qumode hybrid entanglement. *Phys. Rev. A*, 85:032307, 2012.

[104] T. P. Spiller, K. Nemoto, S. L. Braunstein, W. J. Munro, P. van Loock, and G. J. Milburn. Quantum computation by communication. *New J. of Phys.*, 8:30, 2006.

[105] P. van Loock, W. J. Munro, K. Nemoto, T. P. Spiller, T. D. Ladd, S. L. Braunstein, and G. J. Milburn. Hybrid quantum computation in quantum optics. *Phys. Rev. A*, 78:022303, 2008.

[106] P. van Loock, T. D. Ladd, K. Sanaka, F. Yamaguchi, K. Nemoto, W. J. Munro, and Y. Yamamoto. Hybrid quantum repeater using bright coherent light. *Phys. Rev. Lett.*, 96:240501, 2006.

[107] J. B. Brask, I. Rigas, E. S. Polzik, U. L. Andersen, and A. S. Sørensen. Hybrid long-distance entanglement distribution protocol. *Phys. Rev. Lett.*, 105:160501, 2010.

[108] G. Masada, K. Miyata, A. Politi, T. Hashimoto, J. L. O'Brien, and A. Furusawa. Continuous-variable entanglement on a chip. Advance online publication, 2015. doi:10.1038/nphoton.2015.42.